



# UNIVERSITÀ DEGLI STUDI DELL'AQUILA

*DIPARTIMENTO DI SCIENZE FISICHE E CHIMICHE*

*Ph.D Course in Physical and Chemical Sciences,  
XXXVI cycle*

## **The huge versatility of metal oxide nanoparticles: from catalytic to biomedical applications**

***Tutor***

Prof. Marcello Crucianelli

***Co-Tutor***

Prof. Andrea Di Giuseppe

***Coordinator of the Ph.D.  
course***

Prof. Massimiliano Aschi

***Ph.D. Candidate***

Roberta Colaiezzi  
274820

*Academic Year 2022-2023*

# Table of Content

Abstract .....	5
1. General introduction .....	7
1.1 <i>Magnetic properties</i> .....	9
1.2 <i>Synthesis of MNPs</i> .....	16
1.3 <i>Physicochemical characterization of MNPs</i> .....	20
1.4 <i>Application of MNPs</i> .....	22
1.5 <i>Coating of magnetic nanoparticles</i> .....	26
1.6 <i>Aim of the thesis</i> .....	33
References .....	38
2. Investigation of physico-chemical and catalytic properties of the coating layer of silica-coated iron oxide magnetic nanoparticles .....	43
2.1 <i>Introduction</i> .....	43
2.2 <i>Synthesis of silica coated magnetic nanoparticles (SC-IONs)</i> .....	44
2.3 <i>Qualitative evaluation of IONs and SC-IONs</i> .....	45
2.4 <i>Quantitative evaluation of IONs and SC-IONs</i> .....	54
2.5 <i>Catalytic tests as an effectiveness proof of silica coating</i> .....	58
2.6 <i>Experimental</i> .....	61
2.7 <i>Conclusions</i> .....	66
References .....	68
3. Catalytic oxygen atom transfer (OAT) promoted by tethered Mo(VI) dioxido complexes onto silica-coated magnetic nanoparticles .....	71
3.1 <i>Introduction</i> .....	71
3.2 <i>Synthesis of heterogeneous Vanadium (IV) catalyst</i> .....	72
3.3 <i>Synthesis of the heterogeneous catalysts 1–3</i> .....	75
3.4 <i>Characterization of heterogeneous molybdenum-based catalysts 1–3 and their precursors</i> .....	77
3.5 <i>Catalytic olefins oxidation study: reaction in organic solvents</i> .....	81
3.6 <i>Catalytic olefins oxidation study: reaction in aqueous medium</i> .....	84
3.7 <i>Experimental</i> .....	90

3.8 Conclusion .....	95
References.....	98
4. Synthesis and characterization of heterogeneous catalysts for the Suzuki reaction by magnetic induction .....	100
4.1 Introduction.....	100
4.2 Synthesis and characterization of magnetic cores.....	102
4.3 Silica coating .....	112
4.4 Deposition of catalytically active metals.....	116
4.5 Catalytic tests .....	119
4.6 Experimental .....	122
4.7 Conclusions.....	128
References.....	129
5. Synthesis of magnetic nanoparticles in deep eutectic solvents (DES).....	130
5.1 Introduction.....	130
5.2 Synthesis and characterization of deep eutectic solvents (DES) .....	132
5.3 Synthesis and characterization of magnetic nanoparticles .....	139
5.4 Experimental .....	142
5.5 Conclusions.....	143
6. Hybrid polyphenolic Network/SPIONs aggregates with potential synergistic effects in MRI applications.....	146
6.1 Introduction.....	146
6.2 Results and discussion .....	151
6.3 Experimental .....	163
6.4 Conclusions.....	169
References .....	169
7. Selective N-methylation and reduction of variously substituted nitroarenes using catalytic precursors of Ruthenium(II) half-sandwich complexes with dioxime ligands .....	174
7.1 Introduction.....	174
7.2 Synthesis of Ru compounds.....	179

7.3 Reactivity of dioxime complexes in methanol .....	180
7.4 Catalytic activity in the hydrogenation/ <i>N</i> -methylation of nitroarenes .....	181
7.5 Mechanistic insights: organic intermediates .....	190
7.6 Experimental .....	193
7.7 Conclusions .....	208
References .....	208
8. Synthesis of new Iron complexes for water oxidation catalysis.....	212
8.1 Introduction .....	212
8.2 Synthesis of the ligand .....	214
8.3 One-pot Miyaura-Suzuki coupling .....	216
8.4 Synthesis of tetracarboxylic acid .....	217
8.5 Synthesis of tetra acyl chloride .....	218
8.8 Characterization of the complex.....	221
8.9 Preliminary catalytic tests .....	222
8.10 Experimental .....	225
8.11 Conclusions and future work .....	229
References .....	229
9. General conclusions.....	232

## **Abstract**

This thesis work focused on the synthesis, characterization and application of magnetic nanoparticles based on iron oxides. At the beginning, the synthesis of maghemite nanoparticles was optimized and an inert coating was studied. This coating could allow the magnetic core to be covered without obscuring the magnetic properties too much, in order to use the system as a recyclable support for organometallic complexes. The chosen coating was silica and we proceeded by anchoring organometallic complexes of Molybdenum and Vanadium in order to study their reactivity and recyclability, both in organic and aqueous solvents. Subsequently, it was decided to synthesize mixed oxides by adding Nickel and Cobalt to the iron oxides, in order to obtain systems with different magnetic properties. This study led to the obtaining of heterogeneous catalysts in which the different magnetic cores were used as supports for catalytically active Palladium and Ruthenium nanoparticles. In this case it was decided to test the systems for unconventional catalysis, which involved the use of an alternating magnetic field to provide energy to the reaction, instead of using heating through the thermal pathway. For this work, the magnetic properties of the cores were not only used for the recovery of the catalyst, but also for the heating of the reaction itself. Finally, the biomedical application of magnetic nanoparticles was also explored, using it as a basis for the synthesis of metal phenolic networks also containing Gadolinium, used in imaging. Particular attention in all the works was placed on the in-depth characterization of the systems, using

techniques such as: ATR-IR, XRD, XPS, SEM, TEM, AGFM. The data collected by all these techniques allowed us to have a more than complete picture of the synthesized systems.

## 1. General introduction

This thesis work is focused on the synthesis, characterization, and application of magnetic nanoparticles. In the realm of material science, many recent significant advancements are intricately linked to the remarkable progress achieved in the field of nanoscience [1-4]. Nanoscience can be defined as a branch of science that deals with particles that fall in the size range of 1–100 nm. Their small size and better properties such as surface to volume ratio, surface interaction and surface energy when compared to their bulk material are one of the reasons why nanotechnology has been one of the rapidly growing fields of science.

Within this context, nanoparticles (NPs) of various sizes, shapes, and compositions have pushed the boundaries of technology in ways that scientists could not have envisioned even decades ago.

A diverse array of NPs has emerged, finding applications in crucial daily life fields such as biomedical (e.g., drug delivery, MRI contrast agents [5], protein purification [6]), electronics, paints and beauty care, and environmental protection. In most of the above outlined applications, the particles perform best when the size of the nanoparticles is below a critical value, which is dependent on the material but is typically around 10–20 nm.

However, an unavoidable problem associated with particles in this size range is their intrinsic instability over longer periods of time. Such small particles tend to form agglomerates to reduce the energy associated with the high surface area to volume ratio of the nanosized particles. Moreover, naked metallic nanoparticles are chemically highly active, and

are easily oxidized in air, resulting generally in loss of magnetism and dispersibility.

For many applications it is thus crucial to develop protection strategies to chemically stabilize the naked magnetic nanoparticles against degradation, during or after the synthesis. These strategies comprise grafting of or coating with organic species, including surfactants or polymers, or coating with an inorganic layer, such as silica or carbon. It is noteworthy that in many cases the protecting shells not only stabilize the nanoparticles, but can also be used for further functionalization, for instance with other nanoparticles or various ligands, depending on the desired applications.

In the domain of catalysis, a current objective for chemists engaged in material synthesis is the development of novel and viable approaches to enhance the long-term catalytic performances (excellent activity and high stability) in highly challenging areas such as pharmaceutical synthesis, energy, fine chemistry, and more. These advancements, following the principles of "green chemistry," should also address a second challenge, namely, achieving novel catalysts capable of providing total selectivity to the desired products [7].

The key to tackling these challenges lies in the realm of "nano," specifically in the context of nanocatalysis. Consequently, in recent years, this field has undergone explosive development.

Nanocatalysis serves as a bridge between homogeneous and heterogeneous catalysis, preserving the desirable attributes of both systems like high activity and selectivity, typical of homogeneous catalysis, as well as easy separation and recovery of the catalysts, typical of heterogeneous catalysis. Nanocatalysts (NCs), used either as catalysts



or as carriers for the immobilization of homogeneous catalysts [8–10], are thus emerging as potential candidates for fulfilling these conditions. Anyway, in some particular cases, the separation and recovery of such tiny NCs from the reaction mixture, by means of simple filtration, may pose a significant challenge having to employ more costly and time-consuming ultracentrifugation procedures.

This drawback can be overcome by using magnetic nanoparticles (MNPs) as a support for the catalytic active phases. Their paramagnetic character allows easy extraction from the reaction mixture by a simple application of a magnetic field.

### *1.1 Magnetic properties*

Since all materials have an inherent magnetic character stemming from the movements of their electrons, atomic magnetic fields can be induced by applying dynamic electric fields. Magnetic properties, excluding diamagnetism characteristic of materials such as copper, silver, gold, and most known elements, arise from the interactions of unpaired electrons. These properties are found in transition metals, lanthanides, actinides and their compounds, and are attributed to the unpaired d and f electrons of the metal.

Based on the magnetic response to external magnetic fields, these compounds can be generally classified as paramagnetic and ferromagnetic materials. Additionally, there are ferrimagnetic and antiferromagnetic materials, considered as subclasses of ferromagnets [11]. Paramagnetism occurs in materials (e.g., gadolinium, magnesium, lithium, and tantalum) in which the electron spins are randomly oriented

(Figure 1a), while ferromagnetism occurs in materials (e.g., iron, nickel, and cobalt) in which the unpaired electrons are all aligned (Figure 1b). A special kind of magnetic material is represented by those with enforced ferromagnetic properties (called spin glass-like) as the antiferromagnetic materials that have pockets of aligned electron spins (Figure 1c). In antiferromagnets (e.g., MnO, CoO, NiO, or CuCl<sub>2</sub>), the unpaired electrons line up opposite to one another (Figure 1d), while in ferrimagnets (such as magnetite Fe<sub>3</sub>O<sub>4</sub> and maghemite  $\gamma$ -Fe<sub>2</sub>O<sub>3</sub>), the electron spins of adjacent atoms or ions are in an antiparallel alignment, but they do not cancel each other (Figure 1e).

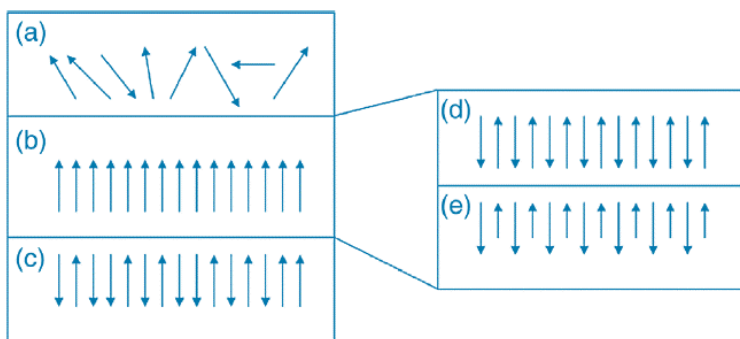


**Figure 1.** Type of magnetism: (a) paramagnetism; (b) ferromagnetism; (c) enforced ferromagnetism; (d) antiferromagnetism; (e) ferrimagnetism.

Therefore, ferromagnetic materials have an overall magnetic moment, while antiferromagnetic materials have a magnetic moment of zero. Ferrimagnetic materials also have an overall magnetic moment due to an inequality in the number of spins in each orientation. When placed in a magnetic field, antiferromagnetic and ferrimagnetic materials show a behavior similar to that of ferromagnetic ones.

When paramagnetic materials are placed in a magnetic field, the magnetic moments of the atoms align along the direction of the applied magnetic field, producing a weak net magnetic moment. These materials do not retain the magnetic moment when the magnetic field is removed. Therefore, in the absence of a magnetic field, the magnetic dipoles will randomize again to demagnetize the material without any extra energy. A nanoparticle that exhibits the above-described behavior is called superparamagnetic (SPM).

Superparamagnetic materials have a single-domain structure, which can fluctuate randomly by thermal fluctuations at high enough temperatures, similar to an atomic spin in paramagnetic materials [12]. At low temperatures, the thermal energy becomes smaller, and the magnetic moments become blocked. This temperature is named the blocking temperature (TB). Below the blocking temperature, the superparamagnetic materials lose their preferred direction of magnetization in zero magnetic fields [13]. When a ferromagnetic material is placed in a magnetic field, the magnetic moments of the domains align along the direction of the applied magnetic field, producing a large net magnetic moment. A residual magnetic moment exists even after the magnetic field is removed. This behavior is called hysteresis, and the plot of the variation of the magnetization versus the magnetic field is called a hysteresis loop (Figure 2).

Three parameters can be identified in the hysteresis loop generated in the field-dependent magnetization measurements: (i) the coercive field ( $H_c$ , which describes the external magnetic field directed oppositely to magnetic dipoles in the material and is reducing the magnetization to zero; this parameter is related to the minimal energy required for the

reversal of the magnetization); (ii) the magnetization at saturation ( $M_s$ , the maximum value of the magnetization that can be reached by the material under a sufficient magnetic field), and (iii) the remanence ( $M_R$ , the residual magnetization at zero applied field.) (Figure 2). In fact, these parameters describe the strength and the magnetization of the material. When placed in a magnetic field, antiferromagnetic and ferrimagnetic materials show a behavior similar to that of ferromagnetic ones.

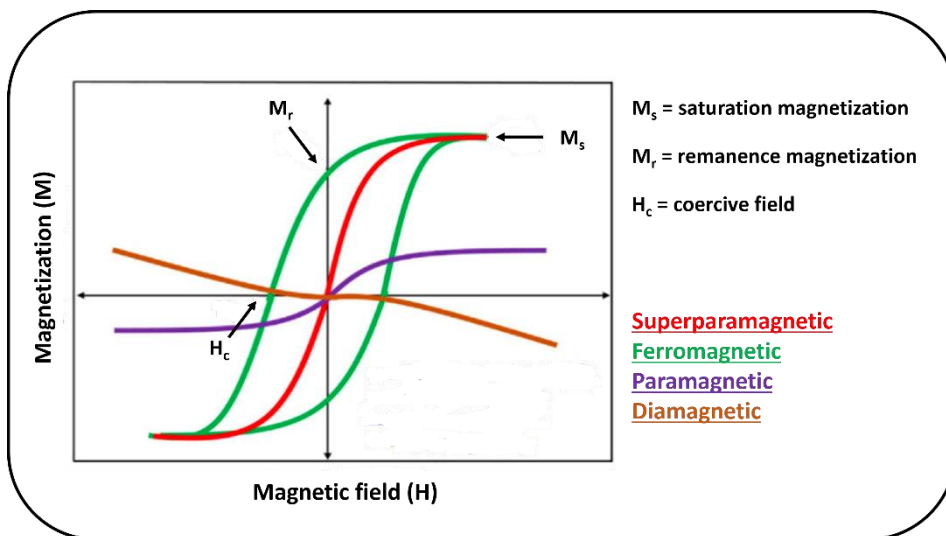


Figure 2. Theoretical magnetic field curve for superparamagnetic (red curve), ferromagnetic (green curve), paramagnetic (purple curve) and diamagnetic (dark yellow curve)

Magnetic nanoparticles show unique magnetic attributes such as superparamagnetic behavior, high coercivity, low Curie temperatures ( $T_c$ ), and high magnetic susceptibility ( $\chi$ , the ratio of magnetization ( $M$ ) to the magnetic field ( $H$ )). Superparamagnetism represents, in fact, the size effect of ferromagnetism [14]. The size reduction below a certain value of the radius, that is, the so-called superparamagnetic radius, may generate changes in both ferri- and ferromagnetic nanoparticles in such

a way that they would become superparamagnetic. However, high magnetic moments were still observed in the absence of any remanent magnetization after the external magnetic field has been removed. In other words, they lack a hysteresis loop. The phenomenon of superparamagnetism is strictly connected to magnetic nanosized materials composed of magnetic single domains and appears when the thermal energy is high enough to overcome the energy barrier for changing the magnetic moments' orientation (Figure 3).

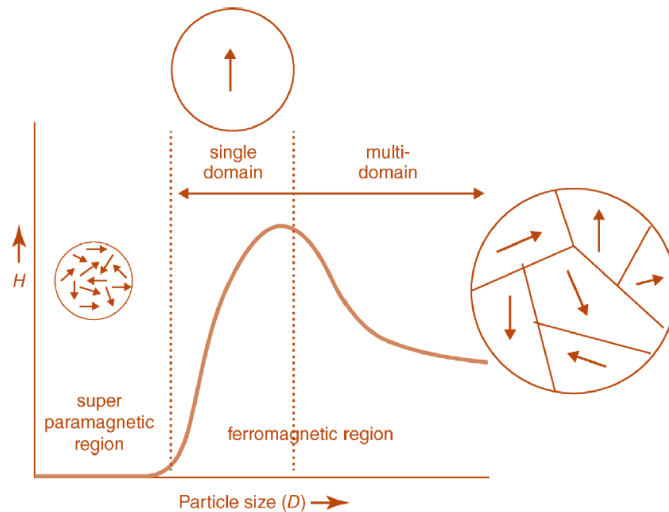


Figure 3. Magnetic coercivity versus the particle size

The surface-to-volume ratio represents a key factor in controlling the physical (e.g., the optical, electric, and magnetic properties), chemical (e.g., the chemical reactivation rate), and mechanical (e.g., strength and hardness) properties of the nanoparticles. Obviously, large ratios differentiate the nanoparticles from the corresponding bulk material. However, the high surface charge and chemical activity of these

nanoparticles may also constitute disadvantages since they enhance their aggregation tendency determined by the minimization of the free energy. Moreover, high chemical reactivity causes their oxidation, resulting in the magnetism and dispersibility losses.

Among iron oxides, magnetite ( $\text{Fe}_3\text{O}_4$ ), maghemite ( $\gamma\text{-Fe}_2\text{O}_3$ ), and hematite ( $\alpha\text{-Fe}_2\text{O}_3$ ) are the most commonly used in different industrial applications [12]. Magnetite (with a formula as  $\text{Fe(III)[Fe(II)Fe(III)]O}_4$ ) is black, ferromagnetic, with an inverse spinel oxide structure. It has an oxygen cubic close-packed (ccp) structure that contains both Fe(II) and Fe(III) ions ( $\text{Fe(II)/Fe(III)} = 0.5$ ), with trivalent ions occupying both tetrahedral (Td) and octahedral (Oh) sites. This oxide is frequently nonstoichiometric with a deficient Fe(III) sub-lattice, having a range of oxidation states dependent on the amount of structural Fe(II). The oxidation of magnetite takes place by migration of Fe(II) cations from the inside to the outside of the particle, creating vacancies ( $\odot$ ). In this case, the Fe(II)/Fe(III) ratio becomes lower than 0.5. Then, Fe(II) cations are oxidized to Fe (III) at the surface, generating maghemite [49]. The structures of the two oxides are given in Figure 4. In magnetite, Fe(III) ions are antiferromagnetically coupled and do not contribute to the magnetic moment.

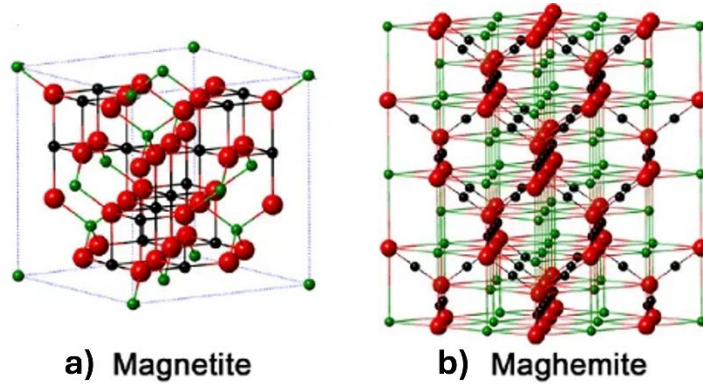


Figure 4. Crystalline structure of magnetite (a) and maghemite (b).

Hence, the magnetic moment of magnetite is due to the contribution of Fe(II) ions with a magnetic moment of  $4\mu_B$ . The sublattice of Fe(III) has a magnetic moment of  $40\mu_B$ , and the sublattice made of Fe(II) and Fe(III) has  $72\mu_B$ . The total magnetic moment of the two combined sublattices is, therefore,  $32\mu_B$ . The saturation magnetization of bulk magnetite is  $84 \text{ emu/g}$  (where emu is electromagnetic unit of magnetic moment) at room temperature, and the Curie temperature is  $850\text{K}$ . The Curie temperature represents the transition temperature between the ferromagnetic and paramagnetic states. In particular, it is the value above which a magnetic material loses this property to become paramagnetic. The magnetic saturation values of magnetite nanoparticles are experimentally determined to be in the range of  $30\text{--}50 \text{ emu/g}$ , which is lower than the bulk value [15]. In maghemite, the magnetic structure consists of two sublattices corresponding to Fe(III) located on Td and Oh sites.

The spins in each sublattice align ferromagnetically, but the spins between the sublattices align antiparallel. The sublattice of Fe(III) in Td

sites is  $40\mu\text{B}$ , and for Oh sublattice is  $66.7\mu\text{B}$ . Ferrimagnetism arises from the decompensation between a number of Fe(III) cations in each sublattice. The total magnetic moment is  $26.7\mu\text{B}$ . The saturation magnetization of bulk maghemite is  $74\text{ emu/g}$  at room temperature, and the Curie temperature is in the range of  $820\text{--}986\text{K}$ . Maghemite has a phase transition to hematite at  $800\text{K}$  [15].

## 1.2 *Synthesis of MNPs*

In the last decade, much effort and research have been devoted to the synthesis of magnetic nanoparticles with different compositions and phases, including iron oxides [16-18], pure metals (such as Fe and Co) [19,20], spinel-type ferromagnets (such as  $\text{MgFe}_2\text{O}_4$ ,  $\text{MnFe}_2\text{O}_4$ , and  $\text{CoFe}_2\text{O}_4$ ) [21,22], and alloys (such as  $\text{CoPt}_3$  and  $\text{FePt}$ ) [23,24].

In terms of recycling expensive catalysts or ligands, the separation of the MNPs catalysts in a quasi-homogeneous system may ensure additional advantages. Besides these, other specific advantages of magnetic nanomaterials in catalysis are: (i) the catalytically active sites can be distributed on the shell (outer surface) of the magnetic core, thus avoiding the pore diffusion constraints, and (ii) the small size of the particles (typically  $<50\text{nm}$ ) allows better dispersion in solvents, thus the external active sites become highly accessible to the reactants.

Various synthetic strategies for the preparation of MNPs have been investigated, including high-temperature decomposition [18], hydrothermal treatment [25], forced hydrolysis [26], solvothermal synthesis [27], chemical coprecipitation [28], electroprecipitation [29],



microwave heating [30], micro- and nanoemulsion [31], sol-gel synthesis [32], sonochemical reactions [33], and laser pyrolysis [34].

Among the mentioned routes, the co-precipitation is probably the most common method used to produce magnetic nanoparticles due to its ease of use, large volume capability, and economy. The first controlled preparation of superparamagnetic iron oxide particles ( $\text{Fe}_3\text{O}_4$ ), with a roughly spherical shape and a size of 8 nm (measured by XRD), was performed by Massart [35], through the precipitation of  $\text{FeCl}_2/\text{FeCl}_3$  in an aqueous alkaline solution. Magnetite ( $\text{Fe}_3\text{O}_4$ ) is, however, not very stable and sensitive to oxidation. In the presence of oxygen, it is easily transformed into maghemite ( $\gamma\text{-Fe}_2\text{O}_3$ ).

Subsequent studies demonstrated the influence of other synthetic parameters such as the nature of the base [36,37], the pH value, the influence of added cations, the nature of the anion of their iron salt, the Fe(II)/Fe(III) ratio, the solution ionic strength, or temperature.

All these parameters were found to influence the yield of the coprecipitation and the size, shape, and polydispersity of the nanoparticles. By adjusting the above parameters, it was possible to tune in a reproducible way the synthesis of  $\text{Fe}_3\text{O}_4$  particles in a range of sizes from 2 to 17 nm [38]. The complete precipitation of the mixture of Fe(II) and Fe(III) (working with a Fe(II)/Fe(III) ratio of 1:2) occurs in a non-oxidizing oxygen environment where the pH is in the range 8–14 [39]. As mentioned above, once the synthetic conditions are fixed, the coprecipitation route is fully reproducible.

However, the reactivity of the magnetite nanoparticles favors their sintering even under ambient conditions, leading to rather polydisperse materials. Therefore, the kinetic factors only control the growth process

and, implicitly, the particle size distribution [28]. Thus, the control of the nucleation and of the subsequent growth (i.e., the slow step) is the key to the production of monodisperse iron oxide magnetic nanoparticles.

Also, the particle mean size of magnetite is strongly dependent on the acidity and the ionic strength of the precipitation medium since they determine the chemical composition of the crystal surface and, consequently, the electrostatic surface charge of the particles [40]. A high pH and ionic strength are leading to small particle sizes and narrow-sized distribution width.

The kinetic control may tailor the particles' size in a range from 4 to 17 nm, while the modulation of acidity and ionic strength enables the tailoring in the range from 2 to 15 nm. The shape of the MNPs is mainly related to the electrostatic surface density [41].

As an alternative, in literature is reported [42] a generalized hydrothermal method for the synthesis of a large variety of nanoparticles, in a more comprehensive sense than the specific case of the MNPs. The method consists of a phase transfer and separation mechanism taking place at the interfaces of the solid, liquid, and solution phases present during the synthesis.

For the synthesis of  $\text{Fe}_3\text{O}_4$  and  $\text{CoFe}_2\text{O}_4$  nanoparticles, the application of this route resulted in very uniform sizes of about 9 and 12 nm, respectively. Although the reaction mechanism has not been entirely clarified, this strategy can be easily extended to the production of other nanomaterials as well.

The thermal decomposition of organometallic compounds is one of the simplest methods for preparing nanoparticles. This technique can be driven by classical heat activation (thermolysis), light activation

(photolysis), or sound activation (sonolysis or sonication). Since the decomposition temperature controls the growth of nanoparticles, monodisperse small-sized magnetic nanocrystals are primarily produced through the decomposition of these organometallic compounds at relatively low temperatures [43].

From the synthetic simplicity point of view, the coprecipitation appears to be the ideal method, but in terms of the control of the nanoparticles' size and morphology, the thermal decomposition is more reliable for the MNPs synthesis. Microemulsions require large amounts of solvent but can also be used to synthesize monodispersed nanoparticles with various morphologies.

The hydrothermal method allows the synthesis of high-quality nanoparticles but is still relatively little explored. To date, MNPs are prepared on a large scale by using the coprecipitation and thermal decomposition methods. The colloidal stability of the MNPs results either from the steric or electrostatic repulsion, depending on the stabilizers (e.g., fatty acids or amines) and the polarity of the solvent. For instance, magnetite nanoparticles synthesized through coprecipitation are positively charged and are stabilized by repulsive electrostatic forces [44]. The nanoparticles synthesized by thermal decomposition are, in general, sterically stabilized in an organic solvent by fatty acids or surfactants [43].

The methods chosen for this study were hydrothermal and solvothermal. These are two similar approaches that allowed us to modulate the properties of the nanoparticles during synthesis, depending on the specific applications under investigation.

### 1.3 *Physicochemical characterization of MNPs*

Various physicochemical characterization techniques can be employed to probe the magnetic behavior, shape, size, and morphologies of the MNPs, the crystalline nature, and the phase purity of magnetic nanoparticles [45-47].

The conventional method for assessing the magnetic properties of a sample involves measuring its attraction or repulsion in a non-uniform magnetic field. Using a Gouy balance, the variation in the apparent weight of the sample is measured when it is immersed in a magnetic field. With a Faraday balance, a magnetic field gradient is generated between two curved magnets, providing precise measurements of susceptibility and magnetization data as a function of the intensity and direction of the applied field. In modern vibrating-sample magnetometers, the sample undergoes vibrations, and an electric field is induced. The signal will have the same frequency as the vibration, and its amplitude will be proportional to the induced magnetization.

The alternating gradient field magnetometer (AGFM) is a device designed for magnetic measurements on nanoscale samples. Its principle is based on detecting the oscillation amplitude of a sample fixed on a quartz probe vibrating in a small alternating gradient field. This device exhibits high sensitivity and can measure samples with a total magnetization as low as  $10^{-6}$  emu. Due to its high resonance frequency, typically in the range of a few hundred Hz, the acquisition time is short. Measurements can be conducted with a magnetic field either parallel or perpendicular to the sample plane. The AGFM technique is crucial not only for assessing the intensity of magnetization but also for

characterizing the magnetic properties of nanoparticles. Through this technique, it is possible to determine whether a sample is superparamagnetic or not, based on the presence or absence of the hysteresis loop. As most conventional magnetization probes, these techniques are not element-specific but rather measure the whole magnetization.

Alongside magnetic characterization, to determine the shape, size, and morphologies of the MNPs, electron microscopy (transmission electron microscopy (TEM), scanning electron microscopy (SEM)), and X-ray diffraction (XRD) are versatile techniques. Specifically, SEM and TEM provide information not only on the shape and morphology of the nanoparticles but also on the degree of their aggregation. From the XRD pattern, it is possible to deduce the obtained phase of iron oxide. XRD also offers insights into the nanoparticle sizes, supporting the results obtained from electron microscopy. However, a typical problem associated with the XRD characterization is that magnetite and maghemite iron oxide nanoparticles possess an inverse spinel structure and are thus difficult to be distinguished by this technique.

Mössbauer spectroscopy (nuclear resonance absorption of  $\gamma$ -rays) can be used to identify iron(oxide) phases of iron-containing MNPs [48].

Another technique providing information about the size of the particles is the dynamic light scattering (DLS). The determination of the diffusion coefficient of the nanoparticles in solution gives access to the hydrodynamic radius of a corresponding sphere and to the polydispersity of the colloidal solution. This technique has recently been used to study the long-term stability of an iron oxide MNPs, with particle distributions ranging from 10 to 200 nm. It is especially suited to follow

aggregation processes [49]. The limitation of the technique is the lack of reliability if the nanoparticles are fluorescent.

For the characterization of the functional groups grafted onto the magnetic materials, Fourier-transform infrared spectroscopy (FT-IR) offers valuable information. A simple attenuated total reflection (ATR) infrared spectroscopy method to characterize the organic–inorganic magnetically separable nanoparticles (e.g., aminopropyl moieties attached on silica shell) was developed by Panella et al. [50]. With the aid of this novel approach, the authors determined that less than 40% of the grafted amino groups onto the silica shell coating magnetite core is available, indicating a remarkable difference between the estimated total amount of functional groups and the actual number of functional groups that were chemically available/accessible for the reaction. The possibility to follow the formation of new bonds after/during the reaction and the great potential for further development using a range of more complex functional groups commonly employed in catalysis, represent additional advantages of the ATR methodology [51].

#### *1.4 Application of MNPs*

In confirmation of the above described large interest in the use of MNPs for several different fields, this section will present examples of catalytic applications of the magnetic core–shell nanoparticles considering the effect of the shell nature (i.e., inorganic, organic, metallic, and oxide).

Magnetically recoverable materials have been used in a wide range of catalytic reactions, including oxidations, epoxidations, hydrogenations, hydroformylations, olefin metathesis, polymerizations, photocatalysis,

and C–C bond formation (e.g., Suzuki, Heck, Sonogashira, and Stille reactions), as well as in novel applications in asymmetric synthesis, organocatalysis, hydration, Knoevenagel condensations, or CO<sub>2</sub> cycloaddition reactions. A really interesting example of hydrogenation catalyst is Palladium on carbon (Pd/C) being a widely utilized catalyst for organic chemistry hydrogenation reactions. Various materials, such as pure Fe<sub>2</sub>O<sub>3</sub> nanospheres, silica-coated Fe<sub>2</sub>O<sub>3</sub> nanoparticles, and carbon-encapsulated Fe<sub>2</sub>O<sub>3</sub>, have been employed as supports for Pd magnetic nanoparticles (MNPs), resulting in magnetically recoverable Pd catalysts. Notably, Pd/C can be adapted into a magnetically separable catalyst through a straightforward nanocasting strategy. The nanocasting synthesis involves several steps: (1) synthesizing a carbon/SBA-15 composite using a mesostructured SBA-15 template, (2) selectively loading cobalt nanoparticles on the composite particle's outer surface, (3) coating a nanometer-thick carbon layer on the cobalt particles for protection, (4) removing the silica scaffold to create a porous system, and (5) depositing a catalytically active noble metal on the now-accessible pore system through conventional impregnation. The resulting catalyst displayed activity in the hydrogenation of octene, demonstrating stability and reusability across multiple runs. The catalyst could be easily removed after the reaction, with no leaching activity observed in the reaction filtrate, as confirmed by the hot-filtration test. The truly heterogeneous nature of the protocol was evident, as no hydrogen consumption was detected during the reaction cycles, emphasizing the efficacy of the magnetic field in immobilizing the catalyst and facilitating its reuse [52].

Oxidation reactions play a pivotal role in the chemical industry but, traditionally, oxidation has been accomplished non-catalytically, employing stoichiometric amounts of oxidants such as chromium and manganese oxides, often in the presence of corrosive mineral acids. In response to increasing environmental concerns, ongoing efforts focus on developing oxidation protocols grounded in green chemistry principles, emphasizing the creation of easily recoverable and reusable heterogeneous catalysts. Addressing these concerns, the utilization of magnetic nanomaterials as solid supports for heterogeneously catalyzed oxidation reactions has proven to be remarkably effective. One of the most important examples in literature are the heterogeneous ruthenium hydroxide ( $\text{Ru}(\text{OH})_x$ ) catalyst supported on magnetic ferrites. This catalyst system demonstrated proficiency in catalyzing the aerobic oxidation of alcohols and amines, as well as the reduction of carbonyl compounds to alcohols using 2-propanol as a hydrogen donor. These systems exhibited catalytic activity across various substrates, encompassing aromatic, aliphatic, and heterocyclic molecules, yielding favorable outcomes without necessitating additional additives or mediators. Notably, product isolation was easily achieved by employing an external magnet, and the recovered catalyst exhibited multiple reuses without significant loss in catalytic performance [53]. Epoxides, such as ethylene oxide and propylene oxide, play a crucial role as intermediates in the industrial synthesis of various chemicals. Given the economic significance of these oxides, there is a demand for new sustainable methodologies. In this context, in literature was demonstrated the efficacy of organic-inorganic hybrid nanocatalysts, synthesized by covalently anchoring  $[(\text{L-L})\text{-MoO}(\text{O}_2)_2]$  ( $\text{L-L} = (3\text{-triethoxysilylpropyl})[3\text{-}$



(2-pyridyl)-1-pyrazolyl]acetamide) onto silica-coated MNPs, as efficient catalysts for selective olefin epoxidation. The reaction exhibited successful outcomes with various substrates, including cyclooctene, cycloheptene, cyclohexene, styrene, and 1-octene, using chloroform as a solvent and tert-butylhydroperoxide (t-BuOOH) as an oxidant under reflux conditions. Recycling studies demonstrated that the catalyst could be readily recovered and reused six times in the epoxidation of cyclooctene without a significant loss of activity. The remarkable activity and stability of this catalyst system are attributed to the uniform dispersion of catalytically active sites on the surface and the strong interaction between the chelating ligand and the molybdenum center [54].

The Suzuki coupling reaction stands out as one of the most significant synthetic transformations developed in the 20th century [55]. The widespread adoption of this reaction at both academic and industrial levels can be attributed to several factors. Firstly, the protocol's versatility allows for the incorporation of numerous functional groups, thanks to its mild reaction conditions, making it an attractive choice for the total synthesis of complex drug molecules. Secondly, boron compounds, a key component in this reaction, are readily available, stable, and generally considered to be of low toxicity. Thirdly, the Suzuki coupling reaction demonstrates efficacy with a broad range of substrates.

An interesting contribution is the developing of Pd *N*-heterocyclic carbene immobilized onto the surface of oleate-stabilized soluble maghemite nanoparticles ( $\gamma$ -Fe<sub>2</sub>O<sub>3</sub>) to create a stable and active magnetic nanocatalyst. The partial solubility of these nanoparticles in

various organic solvents stems from their small dimensions (11 nm  $\pm$  10%) and organic coating. Employing 7.3 mol% of the catalyst and Na<sub>2</sub>CO<sub>3</sub> as the base in the presence of DMF, this catalyst provided nearly quantitative yields for both electron-rich and electron-poor aryl iodides and bromides [56]. The recycling of materials involved magnetic concentration, washing, and air-drying without further purification, demonstrating no significant loss of catalytic activity after multiple reaction cycles. Notably, this catalytic system exhibited higher efficiency compared to an analogous polystyrene solid-phase system, with the increased rate attributed to easier access to the surface active sites. It is clear that, due to their versatility and recyclability, which makes them particularly environmentally friendly, magnetic nanoparticles are finding increasingly interesting applications, especially in catalysis and beyond.

### *1.5 Coating of magnetic nanoparticles*

Despite significant advancements in the synthesis of magnetic nanoparticles, a critical challenge remains in maintaining their stability over an extended period, free from agglomeration or precipitation. Stability is a fundamental requirement for virtually all applications involving magnetic nanoparticles, particularly for pure metals such as Fe, Co, and Ni, as well as their metal alloys, which are highly sensitive to air. The primary obstacle in using pure metals or alloys lies in their susceptibility to oxidation in air, with smaller particles exhibiting increased vulnerability. Consequently, it is imperative to devise effective strategies to enhance the chemical stability of magnetic nanoparticles.

The most direct approach involves protecting the nanoparticles with an impermeable layer, preventing oxygen from reaching the particle surface. Often, stabilization and protection are interlinked, resulting in magnetic nanoparticles adopting a core-shell structure. This configuration entails a naked magnetic nanoparticle core enveloped by a protective shell, isolating the core from the surrounding environment. Protection strategies can be broadly categorized into two main groups: coating with organic shells, including surfactants and polymers [57], or coating with inorganic components, such as silica [58], carbon [59], precious metals (e.g., Ag, Au) [60-61], or oxides formed through gentle oxidation of the outer shell or additional deposition (e.g.,  $Y_2O_3$ ) [62]. Alternatively, magnetic nanoparticles can be dispersed or embedded into a dense matrix, typically composed of polymers, silica, or carbon, forming composites that also mitigate agglomeration and oxidation. However, this immobilizes the nanoparticles in relation to each other, which is often undesirable. In contrast, individually protected nanocrystals, with a free-dispersing and stable nature in various media, are achieved by incorporating a protective shell around them. A short survey on the most frequently employed strategies for MNPs coating, are shown below.

### *1.5.1 Surfactant and Polymer Coating*

Surfactants or polymers are commonly utilized to passivate the surface of nanoparticles during or after synthesis to prevent agglomeration.

Generally, electrostatic or steric repulsion can be employed to disperse nanoparticles and maintain them in a stable colloidal state. Notably, ferrofluids, invented by Papell in 1965 [63], exemplify such systems where the surface properties of magnetic particles are pivotal in determining colloidal stability. Measures to enhance ferrofluid stability include controlling surface charge [64] and employing specific surfactants [65]. For instance, magnetite nanoparticles, typically negatively charged, can be stabilized by peptization using aqueous tetramethylammonium hydroxide or perchloric acid. Surfactants or polymers can be chemically anchored or physically adsorbed on magnetic nanoparticles, forming single or double layers that create repulsive (mainly steric) forces to counterbalance magnetic and van der Waals attractive forces. Polymers with functional groups like carboxylic acids, phosphates, and sulfates can bind to magnetite surfaces. Suitable coating polymers include poly(pyrrole), poly(aniline), poly(alkylcyanoacrylates), poly(methylidene malonate), and polyesters such as poly(lactic acid), poly(glycolic acid), poly( $\epsilon$ -caprolactone), and their copolymers [66]. Surface-modified magnetic nanoparticles with biocompatible polymers find application in magnetic-field-directed drug targeting and serve as contrast agents for magnetic resonance imaging. Chu et al. reported synthesizing polymer-coated magnetite nanoparticles through a single inverse microemulsion, achieving superparamagnetic properties and a narrow size distribution. However, polymer-coated magnetic nanoparticles face challenges including susceptibility to leaching in acidic solutions and limited intrinsic stability at higher temperatures, exacerbated by the catalytic action of metallic cores. This

highlights the need for alternative methods to protect magnetic nanoparticles against deterioration.

### *1.5.2 Silica Coating*

Silica-based materials are commonly employed as heterogeneous catalysts due to the functionalization of amorphous, mesoporous, and zeolitic silica, leading to a wide range of catalytically active materials. Most studies focus on incorporating a single functional group on the surface, often with the aim of immobilizing an existing homogeneous catalyst.

One of the most common supports for heterogeneous catalysts is mesoporous silica. Amorphous silica is sometimes used due to its high surface area and low cost, although surface and pore irregularities may be detrimental in some applications. Microporous materials, like zeolites, can be challenging to organically functionalize, and small pore sizes limit the scope of catalytic reactions to small reactant molecules, increasing the risk of deactivation due to active site saturation.

Ordered mesoporous silica, such as SBA-15 and MCM-41, is easily functionalized in a direct synthesis or post-synthetic grafting procedure. Larger pore sizes (2–10 nm) reduce mass transfer limitations and allow even large reactant molecules to enter the pores. Numerous silica functionalization possibilities exist in the literature. In direct synthesis, a silica precursor is polymerized in the presence of functional organosilanes in a single step. This approach can yield higher loads of functional groups, well-distributed within the silica matrix. Mesoporous silicas typically become less ordered as organic load increases, and

microporous materials often fail to crystallize in the presence of large amounts of organosilanes. Post-synthetic modification, or grafting, involves the covalent attachment of organosilanes to the surface silanols of a pre-fabricated silica material. Generally, a more reactive silane will result in higher organic loads but with less homogeneous distribution. Trichlorosilanes or trialkoxysilanes are often used. As silica is synthesized before grafting, highly ordered silica geometries can be maintained even with moderately high organic loads [67].

### *1.5.3 Alumina Coating*

Among the available support materials, alumina has been widely used due to its low cost, stability in reaction environments, and its ability to provide a wide range of surfaces and porosities suitable for many catalytic applications. While it possesses intrinsic catalytic activity, this is usually negligible in the context of reactions catalyzed by active phases deposited on alumina.

The texture of alumina depends on various factors, with the predominant phase having a significant impact on surface and porosity. As a general rule, porosity increases with surface area, but this alone is insufficient for catalyst design. What is required is a specific distribution of pore sizes. Typically, control is needed over both large (mesopores) and small (micropores) pores, and the means to achieve this vary significantly. Mesopores results from intraparticle voids, and their sizes can be controlled by mixing alumina powder with a removable medium such as graphite, pelletizing, and then removing the graphite through

combustion [68]. Micropores arise from intra-particle voids caused, for example, by the removal of water between crystalline planes.

Surface nature and mechanical strength are equally important and are, to some extent, linked to porosity. For the synthesis of alumina supports, one can start from hydroxide intermediates or purchase directly the alumina of the desired allotropic form in powder or pellet form. It is known that there are two main classes of alumina: low surface area alumina ( $\alpha$ -Al<sub>2</sub>O<sub>3</sub>) and highly porous aluminas of catalytic interest. The latter exists in various forms, of which the so-called " $\eta$ " and " $\gamma$ " are perhaps the most common. Both  $\eta$ -Al<sub>2</sub>O<sub>3</sub>, obtained from the thermal decomposition of bayerite, and  $\gamma$ -Al<sub>2</sub>O<sub>3</sub>, produced through the decomposition of boehmite, have a tetragonal crystal structure, but they are structurally dissimilar as the tetragonal character of  $\eta$ -alumina is considered much weaker than that of  $\gamma$ -alumina. It has been demonstrated that not only the structure but also the texture (i.e., surface area, pore size, etc.) of these two aluminas differ significantly, naturally raising the question of whether catalytic properties and related surface phenomena may also depend on the type of alumina used as a support.  $\gamma$ -Alumina is a hard and translucent solid, while  $\eta$ -alumina is a softer, white, chalky material.  $\gamma$ -Alumina is characterized by a rather uniform pore size, whereas  $\eta$ -alumina exhibits a bimodal pore size distribution [69].

#### *1.5.4 Carbon Coating*

While the majority of studies have traditionally focused on the development of protective coatings using polymers or silica, there is a

growing interest in carbon-protected magnetic nanoparticles due to the numerous advantages offered by carbon-based materials. Carbon exhibits significantly higher chemical and thermal stability, along with biocompatibility, compared to polymers or silica.

The arc-discharge process revealed that carbon-encapsulated metal or metal carbide nanocrystallites could be generated shortly after the discovery of fullerenes. Subsequent research demonstrated that, in the presence of metal nanoparticles (Co, Fe, Ni, Cr, Au, etc.), graphitized carbon structures like carbon nanotubes and carbon onions formed under arc-discharge, laser ablation, and electron irradiation [70]. The well-developed graphitic carbon layers serve as an effective barrier against oxidation and acid erosion. This suggests the feasibility of synthesizing carbon-coated magnetic nanoparticles with thermal stability and resistance to oxidation and acid leaching, crucial for certain applications [71]. Additionally, carbon-coated nanoparticles typically exist in a metallic state, resulting in a higher magnetic moment compared to the corresponding oxides.

A simple method for preparing carbon-coated magnetic Fe and Fe<sub>3</sub>C nanoparticles is through the direct pyrolysis of iron stearate [72]. The resulting nanoparticles were stable up to 400°C under air. Despite a broad size distribution and the presence of multiple graphene layers, this salt-conversion process is advantageous as a single-step approach that can potentially be scaled up. Was also synthesized highly stable carbon-coated cobalt nanoparticles using furfuryl alcohol as a coating material. The resulting carbon layer provided stable protection against air oxidation and erosion by strong acids and bases.



Despite the advantageous properties of carbon-coated magnetic nanoparticles, challenges remain in obtaining these particles in a dispersed form due to the lack of effective synthetic methods and a limited understanding of the formation mechanism. The synthesis of dispersible, carbon-coated nanoparticles in isolated form represents a current challenge in this field.

## 1.6 *Aim of the thesis*

The main purpose of this thesis was to synthesize, characterize, and investigate the applications of various magnetic nanoparticles based on Iron oxides. In this section, the specific goals of each project carried out during the doctoral research, will be discussed in detail.

### 1.6.1 *Optimization of synthesis and coating of magnetic nanoparticles*

The optimization of the synthesis and coating of magnetic nanoparticles was the primary focus of this study. At first, the synthesis of  $\text{Fe}_x\text{O}_y$  nanoparticles was studied and optimized to identify which method, either hydrothermal or solvothermal, was more suitable for the intended applications (Chapter 2). The synthesized cores were subsequently coated with a layer of silica. Silica was chosen as the coating agent due to its inert nature in the reaction environment and ease of functionalization. Tetraethyl orthosilicate (TEOS) was chosen as the silica precursor, and the coating thickness was studied as a function of the amount of TEOS

used during synthesis. Additionally, the synthesis of these magnetic cores in deep eutectic solvents (DES) was explored to evaluate how the composition of DES could influence the magnetic properties, shape, and morphology of the magnetic nanoparticles (Chapter 5). An extensive characterization accompanied this synthesis and optimization phase to thoroughly understand the structure and properties of the obtained products. The primarily used techniques included ATR-IR, AGFM, XRD, XPS, and electron microscopy.

### 1.6.2 *Catalytic application of magnetic nanoparticles*

Once the synthesis of the cores and their coating was optimized, the next step involved functionalizing them for catalytic applications. The first catalytic application involved the heterogenization of vanadium and molybdenum organometallic complexes (Chapter 3). Propylsilane linkers were used to heterogenize the complexes on the supports. In total, four complexes were synthesized, one vanadium complex, and three molybdenum complexes. For the vanadium complex, a Salpr (*N,N'*-bis(3-salicylidenamino)propyl)amine)-like ligand was synthesized, while for the molybdenum complexes, all three ligands were acylpyrazolone-based. The ultimate goal of heterogenizing these complexes was to test them in selective oxidation reactions of double bonds and subsequently to recycle them using the magnetic core. The catalysts were tested and recycled in both organic solvent and aqueous media.

Another catalytic application involved using the magnetic cores not only for recycling but also for catalysis itself, utilizing magnetic induction instead of the traditional oil bath (Chapter 4). For this work, mixed

magnetic cores were synthesized by adding nickel and cobalt to the conventional iron oxides, to evaluate their different magnetic properties and behavior under magnetic induction. These cores were coated with silica, and catalytically active ruthenium and palladium nanoparticles were subsequently deposited. In this case, the chosen reaction to test the activity of the catalysts was the Suzuki coupling, aiming to demonstrate the greater efficiency of the systems tested for magnetic induction compared to catalysis in a bath oil.

### *1.6.3 Biomedical application of magnetic nanoparticles*

Beyond catalytic applications, another crucial aspect explored in this work was in the biomedical field. The aim was to synthesize new contrast agents for imaging using magnetic nanoparticles (Chapter 6). Two different procedures were tested in which magnetic nanoparticles served as the core of metal-phenolic networks (MPN). The MPNs were prepared from magnetic nanoparticles forming the base for a network consisting of tannic acid. Tannic acid was cross-linked either, with formaldehyde (TA reticulation) or by means of Mitsunobu polymerization reaction (TA PEGylation). Finally, gadolinium, a metal widely used in contrast agents, was added.

The goal was to synthesize contrast agents stable in water and easily tunable to achieve a switch between negative and positive contrasts, based on specific needs.

#### 1.6.4 *Homogenous catalysis*

With the ongoing goal of heterogenizing various complexes for different catalytic applications, a study on homogeneous catalysis was also conducted on several complexes. The first type of complexes studied were ruthenium half-sandwich complexes containing oxime ligands (Chapter 7). This project was carried out in collaboration with the University of Pisa (Professor F. Marchetti's group), which synthesized the complexes. The purpose of this work was to test the catalysts in the one-pot reduction/N-methylation reaction of nitroarenes, demonstrating that the oxime ligand played a role in the selectivity of the reaction.

The main advantage of this reaction was the use of methanol not only as a solvent but also as a methylating agent, thus avoiding the use of common highly toxic methylating agents currently in use.

The second homogeneous application was carried out during the overseas period at ICIQ in Tarragona (Spain) under the supervision of Professor A. Llobet (Chapter 8).

The aim of this work was to synthesize new complexes for use in water oxidation catalysis (WOC). Iron was chosen for this purpose as it is more abundant and less expensive than ruthenium, commonly used in this type of catalysis. In particular, a new binuclear iron complex with a pyridine-based ligand containing four carboxylate groups was synthesized, capable of forming complexes with very high oxidation states involved in secondary coordination effects. The obtained complex was then tested in electrochemical catalysis to assess its redox properties and activity in oxygen formation. Obviously, both of these

secondary projects were developed with the perspective of heterogenizing these new complexes, extensively studied during the work under homogeneous catalysis, to leverage magnetic cores for their recycling.

## References

1. Majewski P. and Thierry B., **2007**, *Rev. Solid State Mater. Sci.*, 32, 203–215.
2. Goessmann H and Feldmann C., **2010**, *Angew. Chem., Int. Ed.*, 49, 1362–1395.
3. Thanh N. T. K. and Green L. A. W., **2010**, *Nano Today*, 5, 213–230.
4. Schladt T. D., Schneider K., Schild H., and Tremel W., **2011**, *Dalton Trans.*, 40, 6315–6343.
5. Patel D., Moon J. Y., Chang Y., Kim T. J., and Lee G.H., **2008**, *Colloids Surf. A*, 313, 91–94.
6. Zha, M., Josephson L., Tang, Y., and Weissleder R., **2003**, *Angew. Chem., Int. Ed.*, 42, 1375–1378.
7. Anastas P. and Eghbali N., **2010**, *Chem. Soc. Rev.*, 39, 301–312.
8. Narayanan R. and El-Sayed M. A., **2005**, *J. Phys. Chem. B*, 109, 12663–12676.
9. White R. J., Luque R., Budarin V., Clark J. H., and Macquarrie D. J., **2009**, *Chem. Soc. Rev.*, 38, 481–494.
10. Budroni G. and Corm, A., **2006**, *Angew. Chem.*, 118, 3406–3409.
11. Morrish A.H., **2001**, *The Physical Principles of Magnetism*, John Wiley & Sons, Inc..
12. Cullity B. D. and Graham C.D., **2009**, *Introduction to Magnetic Materials*, 2nd edn, John Wiley & Sons, Inc., New Jersey.
13. Goya G. F. and Morales M. P., **2004**, *J. Metastable Nanocrys. Mater.*, 20, 673–678.
14. Pankhurst Q. A., Connolly J., Jones S. K., and Dobson J., **2003**, *J. Phys. D Appl. Phys.*, 36, 167–181.
15. Gallagher K. J., Feitkhn W., and Mannweiler U., **1968**, *Nature*, 217,

118–1121.

16. Neveu S., Bee A., Robineau M., and Talbot D., **2002**, *J. Colloid Interface Sci.*, 255, 293–298.

17. Grasset F., Labhsetwar, N., Li, Park D. C., Saito N., Haneda, H., Cador O., Roisnel T., Mornet S., Duguet E., Portier J., and Etourneau J., **2002**, *Langmuir*, 18, 8209–8216.

18. Sun S. and Zeng H., **2002**, *J. Am. Chem. Soc.*, 124, 8204–8205.

19. Park S. J., Kim S., Lee S., Khim Z., Char K., and Hyeon T., **2000**, *J. Am. Chem. Soc.*, 122, 8581–8582.

20. Puentes V.F., Krishan K. M., and Alivisatos A. P., **2001**, *Supramol. Sci.*, 291, 2115–2117.

21. Chen Q., Rondinone A. J., Chakoumakos B. C., and Zhang Z. J., **1999**, *J. Magn. Magn. Mater.*, 194, 1–7

22. Park J., Hwang Y., Park J. G., Noh H. J., Kim J. Y., Park J. H., Hwang N. M., and Hyeon T., **2004**, *Nat. Mater.*, 3, 891–895.

23. Sun S., Murray C. B., Weller D., Folks L., and Moser A., **2000**, *Supramol. Sci.*, **287**, 1989–1992.

24. Shevchenko E. V., Talapin D. V., Rogach A. L., Kornowski A., Haase M., and Weller H., **2002**, *J. Am. Chem. Soc.*, 124, 11480–11485.

25. Ji G. B., Tang S. L., Ren S. K., Zhang F. M., Gu B. X., and Du Y.W., 2004, *J. Crystal Growth*, 270, 156–161.

26. Compeán-Jasso M.E., Rui, F., Martínez J. R., and Herrera-Gómez A., **2008**, *Mater. Lett.*, 62, 4248–4250.

27. Guo S., Li D., Zhang L., Li J., and Wang E., **2009**, *Biomaterials*, 30, 1881–1889.

28. Kim Y. I., Kim D., and Lee C. S., **2003**, *Phys. B Condens. Matter.*, 337, 42–51.

29. Marques R. F. C., Garcia C., Lecante P., Ribeiro S. J. L., Noé L., Silva N. J. O., Amaral V. S., Millán A., and Verelst M., **2008**, *J. Magn. Magn. Mater.*, 320, 2311–2315.
30. Bensebaa F., Zavaliche F., L'Ecuyer P., Cochrane R. W., and Veres T., **2004**, *J. Colloid Interface Sci.*, 277, 104–110.
31. Vestal C. R. and Zhang Z. J., **2004**, *Int. J. Nanotech.*, 1, 240–263.
32. Lee J. G., Park J. Y., and Kim C. S., **1998**, *J. Mater. Sci.*, 33, 3965–3968.
33. Suslick K. S., Fang M. M., and Hyeon T., **1996**, *J. Am. Chem. Soc.*, 118, 11960–11961.
34. Gonzalezcarreno T., Morales M. P., Gracia M., and Serna C. J., **1993**, *Mater. Lett.*, 18, 151–155.
35. Massart R., **1981**, *IEEE Trans. Magn.*, 17, 1247–1248.
36. Massart R. and Cabuil V., 1987, *J. Chim. Phys.*, 84, 967–973.
37. Gribanow N. M., Bibik E. E., Buzunov O. V., and Naumov V. N., **1990**, *J. Magn. Magn. Mater.*, 85, 7–10.
38. Tang B., Yuan L., Shi T., Yu L., and Zhu Y., **2009**, *J. Hazard. Mater.*, 163, 1173–1178.
39. Laurent S., Forge D., Port M., Roch A., Robic C., Elst L. Vander., and Muller R. N., **2008**, *Chem. Rev.*, 108, 2064–2110.
40. Jiang W., Yang H. C., Yang S. Y., Horng H. E., Hung J. C., Chen Y. C., and Hong C. Y., **2004**, *J. Magn. Magn. Mater.*, 283, 210–214.
41. Jolivet J. P., Froidefond C., Pottier A., Chaeneac C., Cassaignon S., Tronc E., and Euzen P., **2004**, *J. Mater. Chem.*, 14, 3281–3288.
42. Wang X, Zhuang J., Peng. Q., and Li Y. **2005**, *Nature*, 437, 121-124.
43. Sun S., Zeng H., Robinson D. B., Raoux S., Rice P. M., Wang S. X., Li G., **2004**, *J. Am. Chem. Soc.*, 126, 273-279.
44. Bee A., Massart R., Neveu S., **1995**, *J. Magn Magn. Mater.*, 149, 6-9.



45. Ney A., Pouloupoulos P., Farle M., and Baberschke K., **2000**, *Phys. Rev. B*, 62, 11336–11339.
46. Foner S., **1959**, *Rev. Sci. Instrum.*, 30, 548–557.
47. Lindner P. and Zemb T., 2002, *Methods Applied to Soft Condensed Matter*, Elsevier, Dordrecht.
48. Corr S. A., Gun'ko Y. K., Douvalis A. P., Venkatesan M., Gunning R. D., and Nellist P. D., **2008**, *J. Phys. Chem. C*, 112, 1008–1018.
49. Lim J. K., Majetich S. A., and Tilton R. D., **2009**, *Langmuir*, 25, 13384–13393.
50. Panella B., Vargas A., Ferri D., and Baiker A., **2009**, *Chem. Mater.*, 21, 4316–4322.
51. Al-Hashimi M., Qazi A., Sullivan A. C., and Wilson J. R. H., **2007**, *J. Mol. Catal. A Chem.*, 278, 160–168.
52. Lu A., Schmidt W., Matoussevitch N., Bonnemann H., Spliethoff B., Tesche B., Bill E., Kiefer W., Schwith F., **2004**, *Angew. Chem., Int. Ed.*, 43, 4303.
53. Kotani M., Koike T., Yamaguchi K., Mizuno N., 2006, *Green Chem.*, 8, 735.
54. Shylesh S., Schweizer J., Demeshko S., Schunemann V., Ernst S., Thiela W. R., **2009**, *Adv. Synth. Catal.*, 351, 1789.
55. Miyaura N, Yanagi T., Suzuki A., **1981**, *Synth. Commun.*, 11, 513.
56. Zheng Y., Stevens P. D., Gao Y., **2006**, *J. Org. Chem.*, 71, 537.
57. Euliss L. G., Grancharov S. G., Brien S. O., Deming T. J., Stucky G. D., Murray C. B., Held G. A., **2003**, *Nano Lett.*, 3, 1489.
58. Kobayashi Y., Horie M., Konno M., Rodriguez-Gonzalez B., Liz-Marzan L. M., **2003**, *J. Phys. Chem. B*, 107, 7420.
59. Lu A.-H., Li W., Matoussevitch N., Spliethoff B., Pnnemann H. B., SchVth F., **2005**, *Chem. Commun.*, 98.

60. Sobal N. S., Hilgendorff M., Moehwald H., Giersig M., Spasova M., Radetic T., Farle M., **2002**, *Nano Lett.*, 2, 62.
61. Liu Q., Xu Z., Finch J. A., Egerton R., **1998**, *Chem. Mater.*, 10, 3936.
62. Lin J., Zhou W., Kumbhar A., Wiemann J., Fang J., Carpenter E. E., Connor C. J., **2001**, *J. Solid State Chem.*, 159, 26.
63. Papell S. S., **1965**, *US Patent 3215572*.
64. Massart R., **1981**, *IEEE Trans. Magn.*, MAG-17, 1247.
65. Raj K., Moskowitz R., **1990**, *J. Magn. Magn. Mater.*, 85, 107.
66. Wan M., Li J., **1998**, *J. Polymer. Sci.*, 36, 2799.
67. Margelefsky E. L., Zeidanb R. K., Davis M. E., **2008**, *Chemical Society Reviews*, 37, 1118-1126
68. Trimm D.L., Stanislaus A., **1986**, *Applied Catalysis*, 21, 215-238.
69. Maciver D. S., Tobin H. H., Barth R. T., **1963**, *Juornal of Catalysis*, 2, 485-497.
70. Ang K. H., Alexandrou I., Mathur N. D., Amaratunga G. A. J., Haq S., **2004**, *Nanotechnology*, 15, 520.
71. Chan H. B. S., Ellis B. L., Sharma H. L., Frost W., Caps V., Shields R. A., Tsang S. C., **2004**, *Adv. Mater.*, 16, 144.
72. Geng J., Jefferson D. A., Johnson B. F. G., **2004**, *Chem. Commun*, 2442.

## **2. Investigation of physico-chemical and catalytic properties of the coating layer of silica-coated iron oxide magnetic nanoparticles**

### *2.1 Introduction*

This work originates as an in-depth study, not only on the magnetic properties of nanoparticles but primarily on the optimization of a coating to achieve a subsequently functionalizable core-shell structure [1-3]. Indeed, due to the scarce availability, in the specific literature, of studies concerning the actual role, if any, of the magnetic metal core in influencing the catalytic outcome of the main process to be catalysed, before and after silica coating, we decided to study this aspect in the case of our MNPs, which will then be used for catalytic oxidation promoted by other metals anchored on the silica layer as metal complexes (see Chapter 3). A thorough investigation was conducted on the type of coating and its properties.

Silica was chosen as the coating material since, as explained earlier, it is inert in the reaction environment and easily functionalizable. The objective was to obtain a homogeneous coating that does not overly obscure the magnetic properties of the core, with the perspective of subsequent functionalizations [4].

In assessing the uniformity of the coating, a probe reaction involving the Fenton-like oxidation of cis-cyclooctene was conducted. These tests were carried out not only to demonstrate that the core was fully shielded and therefore non-reactive in catalysis but also to affirm the effective stabilization provided to the core.

In order to precisely understand the nature and properties of both the core and the coated core, a comprehensive characterization of the nanoparticles was conducted using techniques such as: ATR-IR for a preliminary assessment of oxide formation; AGFM to evaluate the magnetic properties of the core before and after coating; ICP-MS to assess Fe/O and Si/O ratios; SEM and TEM to determine the morphology and dimensions of the nanoparticles; XRD to identify the ferrite phase and confirm dimensions; BET to determine the surface area; and XPS to evaluate the oxidation states of Fe and Si.

## *2.2 Synthesis of silica coated magnetic nanoparticles (SC-IONs)*

The co-precipitation method was employed for the synthesis of Iron Oxide Nanoparticles (IONs), resulting in a finely powdered dark maroon substance. Preliminary assessment of its magnetic properties was conducted using a permanent magnet immediately after the drying process. Subsequently, the coating process was initiated, initially following the littérature conditions [5] with modifications, leading to Silica-Coated samples (referred to as SC hereafter). In this procedure, we opted to vary the thickness of the silica coating by adjusting the amount of Tetraethyl orthosilicate (TEOS) during synthesis. Consequently, three distinct SC samples were generated, and their specific surface area values are presented in Table 1.

**Table 1.** Summary of the four samples synthesized

<b>Sample name</b>	<b>TEOS (ml)</b>	<b>Specific surface area (m<sup>2</sup>·g<sup>-1</sup>)</b>
<b>IONs</b>	0	188
<b>SC1</b>	0.1	170
<b>SC2</b>	0.5	122
<b>SC3</b>	1	118

Notably, an observable trend in the silica shell is evident, with a color shift towards a brighter brown correlating with an increase in the silicating agent in the synthetic process. Upon obtaining both the coated and uncoated IONs, a comprehensive physico-chemical characterization was undertaken. The objective was to thoroughly examine their intrinsic nature, both qualitatively and quantitatively.

### *2.3 Qualitative evaluation of IONs and SC-IONs*

In the following step, we will provide a qualitative image of the synthesized samples, with techniques able to discriminate the physical and chemical nature of core and shell of the catalyst. XRD technique (shown in Figure 5) reveals the typical pattern of maghemite ( $\gamma\text{-Fe}_2\text{O}_3$ ) for all the samples under investigation [6–8].

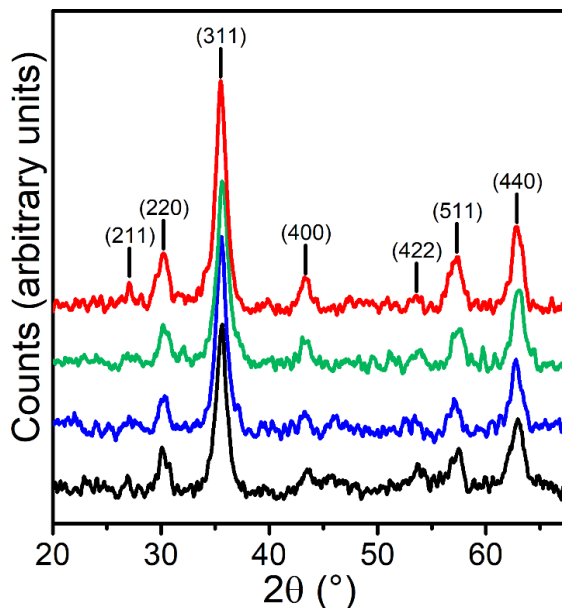


Figure 5. XRD patterns of IONs (black line), SC1 (blue line), SC2 (green line) and SC3 (red line), with the corresponding peak assignment.

Maghemite and magnetite share the same spinel crystal structure; however, the dimension of the unit cell is slightly larger for magnetite, meaning a small shift of all diffraction peaks towards lower angles. Due to peak broadening intrinsic for nanoparticles samples, the phase identification become quite difficult based on peaks position. Luckily, maghemite shows an additional peak around  $2\theta=26^\circ$ , corresponding to (211) reflection, which is absent in magnetite pattern [8,9]. Observing the broadening of the diffraction peaks it is also possible state that we are in the presence of samples in the nanoparticles range. As expected, different coating thicknesses seem not to affect the crystal structure of IONs, due to the mild conditions used for the coating of silica layer on top of the magnetic phase. Contrariwise, particles crystalline dimensions seem to be slightly affected: the average diameter, calculated with Scherrer equation applied to the (311) reflection, varied from 10.2 nm

for IONs to 7.3 nm for SC3. This variation does not mean necessarily that the size of the particle changed (see microscopy part), but possibly that the increasing amount of silicating agent (creating a layer of amorphous silica, as evidenced by the absence of  $\text{SiO}_2$  diffraction peaks) progressively affects the surface of the particles. For amorphous coated crystalline phases, it is possible the formation of a third phase at the interface between the core and the coating [10]: for macroscopic crystals the effect on crystal size is negligible; however, dealing with nanoparticles, the lower number of atoms available to generate the interfacial phase produces a more evident effect on crystal size. Therefore, we hypothesize the formation of an amorphous Fe-Si mixed oxide, provoking the slight variation observed. The magnetic character of the particles was evaluated measuring the magnetic moment of the specimens as a function of the applied magnetic field. In Figure 6 the specific magnetization (per sample unit mass, i.e. silica-coated  $\text{Fe}_2\text{O}_3$ ) is reported for the different samples.

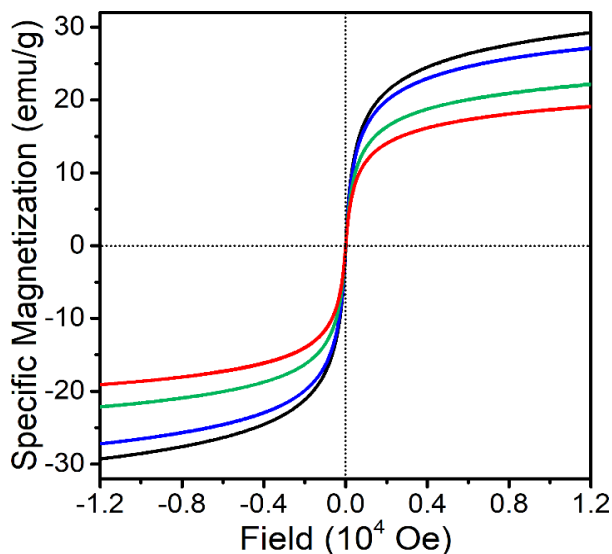


Figure 6. Magnetization curves of IONs (black line), SC1 (blue line), SC2 (green line) and SC3 (red line).

The qualitative shape of the magnetization curves indicates a dominant superparamagnetic (SP) behavior, suggested by the absence of hysteresis and residual magnetization once we remove the applied magnetic field, and by the trend to saturation at high field. As expected, the value of the specific magnetization decreases progressively with the increase of the silica layer thickness, i.e. as the Si fraction becomes higher [11-13], since its effect on the magnetic properties is that of simple mass addition, without any appreciable contribution to the magnetization. However, the maximum magnetization for ION sample, although sufficient to guarantee good recovery properties of our catalysts, is lower than the one of the bulk maghemite ( $\approx 75$  emu/g), but it's in the correct range for  $\sim 10$  nm nanoparticles [14,15]. The value found for our magnetic system is perfectly in line with ones having similar morphology [16,17], yet still lower in comparison with other systems in which particles arrange in more ordered shape (i.e. nanochains) [17,18]. However, as carriers of further catalytically active species, this system behaves in line with similar ones at the same synthetic stage [13,14,19]. This feature, together with the incomplete saturation at the maximum field, suggests the presence of a paramagnetic fraction of iron oxide, possibly consisting of uncompensated moments confined on the disordered surface layer of the particles. With the help of Transmission Electron Microscopy we are able to directly visualize the status of the synthesized catalysts, in order to correlate it with the amount of silica coating the maghemite core, therefore causing the decrease of magnetic properties [14,20]. Comparing samples IONs and SC1 (Fig.7a and b respectively) it is



possible to notice how the amount of silicating agent added to the synthesis forms a coating layer that is barely visible with the microscope, yet sufficient to favor and provoke a partial aggregation of the nanoparticles.

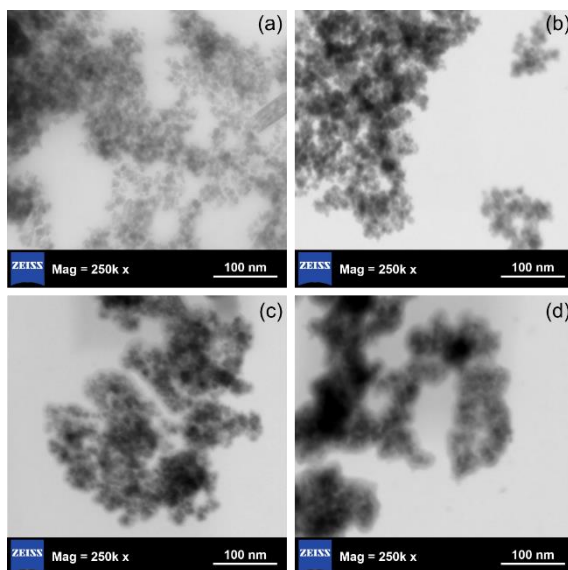


Figure 7. S-TEM images collected at 250k x magnification of IONs (part a), SC1 (part b), SC2 (part c) and SC3 (part d).

This is testified also by the minimum change in the surface area of the samples (Table 1), varying from  $188.2 \text{ m}^2 \text{ g}^{-1}$  to  $170.6 \text{ m}^2 \text{ g}^{-1}$ . Passing from SC1 to SC2 (Fig. 7b and c respectively) we observe the formation of a non-negligible amount of coating; correspondingly the surface area further decreases to  $122.5 \text{ m}^2 \text{ g}^{-1}$ . Finally, sample SC3 (Fig. 7d) does show an increasing enveloping in IONs with the silica coating: even though it is possible to appreciate the increasing thickness of the silica layer, surface area only slightly decreases to  $118.6 \text{ m}^2 \text{ g}^{-1}$ . An explanation for such trend in the variation of surface area values is difficult to be found in the literature, where it is possible to observe a decrease in the

surface area values of the samples, passing from SC-IONs to the following functionalization steps with active moieties or by increasing the amount of silicating agent [21,22]. One hypothesis to explain this trend might lie in the shape of the particles: liquid phase coating process gave a rounded shape to the nanoparticles, thus minimizing the surface area value. Also, enveloping phenomena between covered particles appears when we increase the amount of silicating agent in the coating synthesis and might strongly contribute to the decrease of surface area. Furthermore, the enveloping process with a progressively higher amount of TEOS (SC1 to SC3) tends to reduce the coarseness of the surface, thus reducing the surface area, as clearly visible by comparing the SEM images of samples SC1 and SC3, having surface area values of 170.6 and 118.6 m<sup>2</sup> g<sup>-1</sup> respectively. Using transmission SEM images, we also estimated the average thickness of the silica shell, which passes from 4.5 nm for SC1 to 7.7 nm for SC3, growing consistently with the increase of TEOS employed in the synthetic procedure. The techniques listed so far are not the only sensitive to the change in the ratio between core and shell of our samples. Spectroscopic techniques in general are qualitatively sensitive to ratios between different atomic/molecular species. Vibrational spectroscopies, especially FT-IR, are able to investigate the chemical moieties present in the whole thickness of the sample (150 nm at maximum), being the penetration depth of mid-infrared radiation c.a. 1000 nm [23].

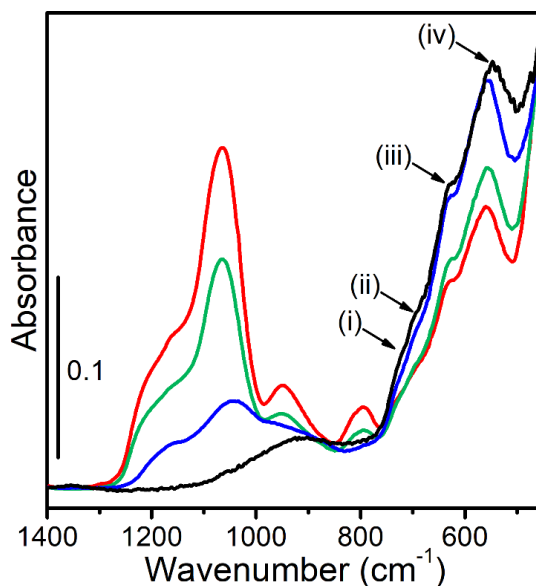


Figure 8. ATR-IR spectra, in the 1400-450  $\text{cm}^{-1}$  spectral region, of IONs (black line), SC1 (blue line), SC2 (green line) and SC3 (red line).

FT-IR spectroscopy provides information based on the vibration frequencies of chemical bonds and is able to clearly distinguish oxides of different nature simply by their difference in atomic weight. The ATR-IR configuration that we employed allows to investigate uniformly the sample, avoiding detector saturation; ATR-IR data are shown in Figure 8. The spectral range displayed can be divided in two zones showing bands belonging to different chemical species: a) the region between 1300 and 750  $\text{cm}^{-1}$  contains the band relative to symmetric ( $800 \text{ cm}^{-1}$ ) and antisymmetric ( $1060 \text{ cm}^{-1}$ ) stretching of Si-O bond from silica [5,24,25]; b) in the spectral region between 750 and 500  $\text{cm}^{-1}$ , it is possible to observe four different bands belonging to various Fe-O bond vibrations, more precisely at 725 (i), 701 (ii), 634 (iii) and 557  $\text{cm}^{-1}$  (iv) [6,26]. Among the ones listed above, the band (iii) is peculiar for maghemite and indicates that we are in the presence of this ferrous phase [26,27]. Across

the series of catalysts under investigation, we can observe a clear trend in which the region of maghemite vibrations (highest for IONs sample, black line in Fig.8) is progressively eroded at advantage of the silica region, upon gradual increase of SiO<sub>2</sub> shell thickness (highest for SC3 sample, red line in Fig. 8). The techniques employed so far were able to give a qualitative ratio between maghemite and silica. However, in order to shed light on the spatial distribution of the two phases we need to employ a method especially responsive to the outer layer of the catalysts that will be in contact with the reaction environment. The perfect choice for our purpose is X-ray Photoelectron Spectroscopy, which is by definition the most surface-sensitive technique, able to analyze only the first few nanometers at the external part of the samples. It is also an element selective technique, allowing to investigate the atomic composition of the materials. Since the probe of the technique is the kinetic energy of charged particles, this might be influenced by the charge of the emitting atoms and their neighbors; therefore, we expect a shift in the binding energy of O 1s peak in case the emitting atom is bound to either Si or Fe.

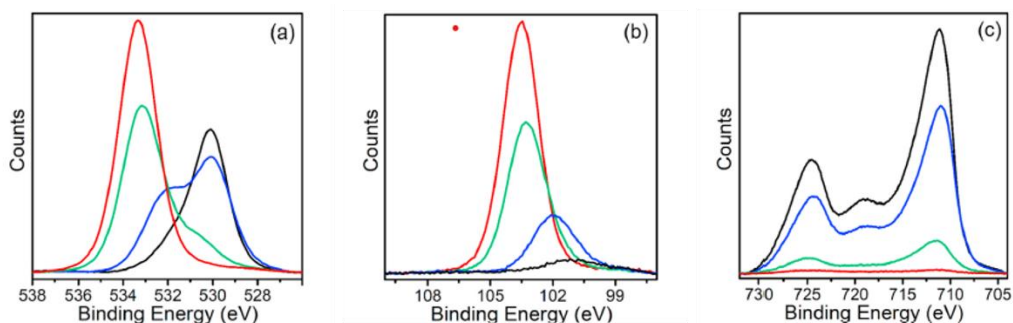


Figure 9. O 1s XPS spectra (part a), Si 2p XPS spectra (part b) and Fe 2p XPS spectra (part c) of IONs (black line), SC1 (blue line), SC2 (green line) and SC3 (red line).

Figure 9a shows the O 1s XPS spectra of all samples under investigation. It is possible to notice that, depending on the sample, two peaks are present in the spectrum, one at 533.1 eV relative to Si–O bond [25,28], and the other centered at 530.0 eV relative to Fe–O bond [29,30]. The two bands described above correlate perfectly with the catalysts under analysis: IONs sample (black line in Fig. 9a) displays only the band at 530 eV, as expected for pure maghemite sample. When we increase the amount of TEOS during the synthesis (therefore increasing the thickness of the silica shell), we assist to a progressive reduction of the Fe–O band and the consequent growth of the one relative to Si–O bond. Once we reached a sufficient thickness of SiO<sub>2</sub> coating, the band relative to Fe–O bond of  $\gamma$ -Fe<sub>2</sub>O<sub>3</sub> totally disappears (red curve in Fig. 9a, corresponding to sample SC3), meaning that the thickness of the silica layer is comparable to the mean free path of electrons emitted from iron. This trend can also be observed from Si 2p and Fe 2p XPS spectra (Fig. 9b and c respectively), in which iron signals are decreasing and the silicon one is growing moving from IONs to SC3. XPS can provide further information on the status of the samples. Fig. 9c, shows that the position of both Fe 2p<sub>1/2</sub> and Fe 2p<sub>3/2</sub> peaks remains unchanged when increasing the silica content, meaning that no changes occur at the maghemite phase. Conversely, Fig. 9b shows a progressive shift of the Si 2p signal towards higher binding energy, excluding IONs sample - black line - in which the broad signal centered at 101 eV is the Fe 3s peak. This effect is explainable by the fact that ionization energy for bulk silica (at 103.5 eV) corresponds to the case in which every Si atom is tetrahedrally coordinated by four strongly electronegative oxygen atoms. By reducing the amount of silicating agent, we created a thinner layer of coating, thus

influencing the coordination of silicon atoms: in this way, we synthesized a silica with defective  $\text{SiO}_{4-x}(4-x)$ - tetrahedra. This means that we are diminishing the electron withdrawing effect due to the lack of highly electronegative oxygen atoms, and consequently the electrons binding energy. This phenomenon does affect not only Si 2p spectra: also O 1s spectra show a similar behavior for the peak ascribed to Si–O bond (Fig. 9a).

#### 2.4 Quantitative evaluation of IONs and SC-IONs

After the synthesis of the silica coated IONs (SC1-SC3), it was important to quantitatively assess the ratios between the magnetic core and the silica shell. The best way is to analyze the samples with ICP-MS technique. Data reported in Table 2 show how the variation of  $\text{SiO}_2$  content consistently increases with the amount of TEOS introduced, going from SC1 to SC3.

**Table 2.** Evaluation of  $\text{SiO}_2/\text{Fe}_2\text{O}_3$  ratio from different techniques (ICP-MS and AGFM) for pure IONs sample and for SC1-SC3 coated samples.

	ICP-MS data					mass ratio ( $\text{SiO}_2/\text{Fe}_2\text{O}_3$ )	
	%Si	%Fe	%SiO <sub>2</sub>	% $\gamma$ - $\text{Fe}_2\text{O}_3$	%total	ICP-MS	AGFM
IONs	-	69.5%	-	99.3%	99.3%	-	-
SC1	3.0%	60.6%	6.5%	86.7%	93.1%	0.07	0.06
SC2	9.3%	53.5%	19.9%	76.5%	96.3%	0.26	0.30
SC3	18.6%	36.0%	40.7%	51.4%	92.1%	0.79	0.51

The total mass calculated as the sum of silica and maghemite (assuming these are the only two possible sources of Si and Fe), always results in a value close to 100%. The most probable uncertainties on the mass may arise from unreacted TEOS, leaving ethoxydangling bonds that are removed during the digestion process; moreover, the formation of volatile  $\text{SiF}_4$  may cause a slight loss of Si. ICP-MS is not the only technique able to quantify Si and Fe amounts among the samples. Also the comparison of the different magnetization curves can provide information regarding the silica/iron oxide ratio of the various samples. Subtraction of a small linear term, attributed to the aforementioned paramagnetic contribution, allows us to isolate the purely superparamagnetic character of each curve. Subsequent normalization evidences how the four curves perfectly overlap, as shown in Figure 10, where all the data points for all samples are represented in the first quadrant of the graph.

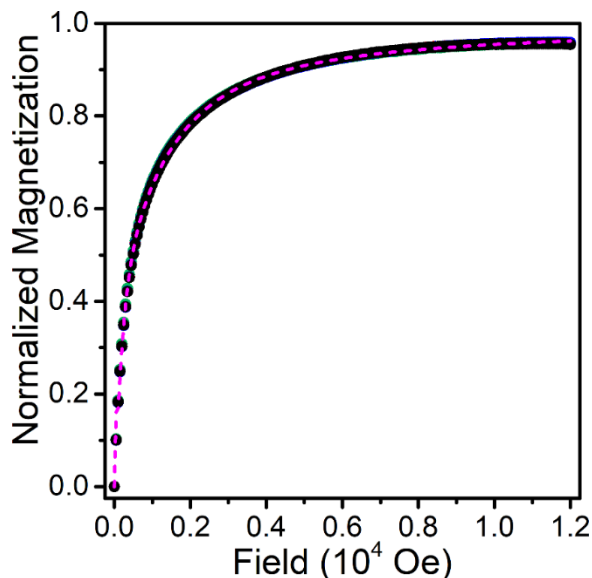


**Figure 10.** normalized magnetization curves. The data points of all samples and for both positive and negative branches are represented all together in the first quadrant and fitted by the pink dashed line according to a double Langevin function (see text). The fitting curve overlaps very well the experimental data points.

This proves that the relevant SP response is not affected by the covering shell. We emphasize that the subtracted linear term is the same for samples SC1, SC2 and SC3, whereas it is slightly larger for sample IONs. This variation may be attributed to a partial reduction of the surface magnetic moment (which, however, does not affect the single-domain core of the particles) due to the extra bonds with the non-magnetic atoms of the covering shell, when present. The normalization factors of the four curves are used to infer the  $\text{SiO}_2/\text{Fe}_2\text{O}_3$  mass. These values are substantially consistent, with the only exception of SC3 sample, with those obtained with ICP-MS technique. Additional quantitative information can be achieved through the analysis of the magnetization curves. The model for single-domain SP particles leads to the well-known Langevin function describing the magnetic induction (B) dependence of the magnetization M of a set of identical single-domain particles, each with a magnetic moment  $\mu$ , at a fixed temperature. Here,  $M_S$  is the saturation magnetization and  $k_B$  is the Boltzmann constant. In a real system, with particles of different sizes and magnetic moments, such a function does not fit exactly the experimental data. The fitting continuous curve shown in Figure 10 is obtained using a double Langevin function. A more accurate fitting, using a continuous distribution of magnetic moments does not improve significantly the agreement with the experimental data. Consequently, we used the above mentioned parameters to calculate the representative average magnetic moments of the distribution. If we assume the bulk magnetization for  $\gamma\text{-Fe}_2\text{O}_3$ , and



spherical shape of the particles, this gives as average diameter of 10.2 nm, in line with the qualitative evaluation obtained with XRD and TEM techniques. However, this parameter should be more appropriately attributed to the inner single-domain part of the IONs, if an outermost region of oxide, in a paramagnetic state, is present. A similar approach to obtain quantitative information about Si/Fe ratio and thickness of the coating can be obtained by a deeper analysis of XPS data. In Table 3 it is possible to observe how, by increasing the amount of TEOS in the synthesis, we ended up with increasing thickness of the coating layer, as already evidenced.

**Table 3.** XPS peak areas and relative Si, O and Fe elemental abundance for IONs sample and SC1-SC3 coated samples.

	Si	O-Si	O-Fe	Fe	Si %	O-Si %	O-Fe %	Fe %	$\gamma$ -Fe <sub>2</sub> O <sub>3</sub> %	SiO <sub>2</sub> %
ION	0	0	41512	132811	0	0	56	44	100	0
SC1	5698	26751	31038	91868	12	29	34	25	67	33
SC2	12792	67000	7056	18566	24	64	7	4	15	85
SC3	19245	90378	1488	3264	29	69	1	1	2	98

From these data, it is possible to notice an overestimation of the silica content. This is due by the surface sensitivity intrinsically present in XPS technique; therefore, few nanometers of coating are sufficient to completely hide the magnetic core, which however, is still present. Aware of this problem, we used the information about the core size obtained from XRD data and the electrons mean free path (MFP) to evaluate the thickness of the silica coating. Considering the variation of the core particle radii passing from 5.09 nm (value for IONs) to 3.65 nm (value for SC3) and electrons MFP of 1.9 nm at ~550 eV (kinetic energy

of emitted Fe 2p electrons that have to be detected after crossing the silica coating), we found silica shell thickness of 0.79 nm for SC1, 1.82 nm for SC2 and 3.13 nm for SC3.

### *2.5 Catalytic tests as an effectiveness proof of silica coating*

In the previous sections, we have extensively evaluated the degree of coating surrounding our magnetic system. Our purpose, already widely stated in the introductory part, is to exploit the magnetic properties of maghemite to easily recover the catalysts that will be heterogenized on the synthesized SC-IONs, having in mind their use in the selective catalytic oxidations of organic substrates, promoted mainly by oxidants like H<sub>2</sub>O<sub>2</sub> or TBHP [20,29,31]. Thus, at the same time, we are strongly interested in proving the effectiveness of the iron oxide shielding, since iron oxides themselves are also employed as catalysts for liquid phase oxidations using peroxides as oxidants [32]. This is the reason why cis-cyclooctene [33] has been chosen as the best candidate to serve as the model substrate for our catalytic test, due to its high reactivity and selectivity in the TBHP promoted oxidation process. However, iron oxides in combination with peroxides, can lead to a decomposition of the oxidizing agent with a Fenton-like mechanism [34], thus affecting negatively the desired main oxidative reaction. Even though hydrogen peroxide is more reactive towards iron species that might remain exposed after silica shell synthesis [35], we decided to replicate reaction conditions that are already employed for liquid phase oxidation reactions with catalysts bearing organometallic complexes anchored onto silica-coated magnetic nanoparticles (namely TBHP as main oxidant in a chlorinated solvent) [14,20]. Having these conditions in mind, we

performed the oxidation of cis-cyclooctene using TBHP (5.5 M in n-decane). The exposure of cis-cyclooctene to TBHP only, naturally leads to the formation of a certain amount of cyclooctene epoxide. As evidenced by the pink line in Figure 11, without the use of any of our samples, at 60° C we observe 27% conversion of cis-cyclooctene with almost 100% selectivity towards epoxide product. Similar behavior is obtained when performing the reaction with all our silica-coated samples, demonstrating the desirable chemical inertia that we are looking for.

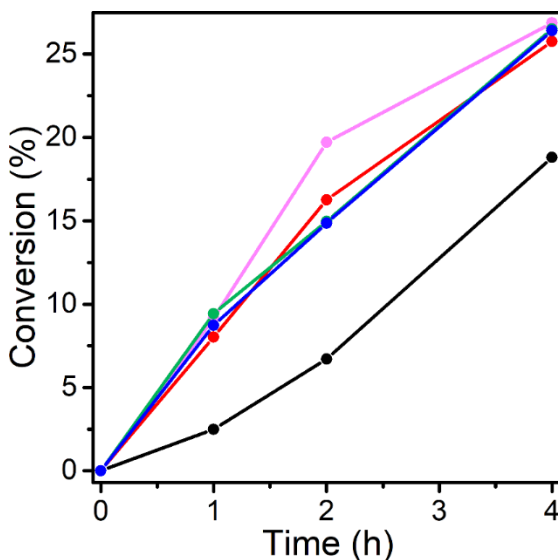
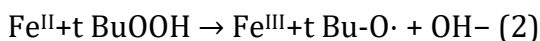
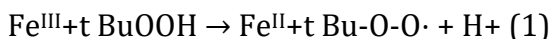


Figure 11. Conversion values for cis-Cyclooctene oxidation reaction with tert-Butyl hydroperoxide: blank reaction (no catalyst - pink line), and with IONs (black line), SC1 (blue line), SC2 (green line), SC3 (red line), as catalysts.

Conversely, reaction performed with IONs sample displays slower rate at the beginning of the reaction (6.7% compared with 15–20% for all other tests after 2 h reaction), inducing us to measure the residual amount of oxidant with iodometric back titration [36]: while for all reactions using coated nanoparticles the residual oxidant is almost the

same remaining after reaction without any catalyst, the residual amount for reaction performed with uncoated nanoparticles is significantly lower. Therefore, a lower conversion with a higher oxidant consumption is the symptom of a Fenton-like side reaction involving iron species at the surface of the particles: [34,36]



$\text{Fe}^{\text{III}}$  from  $\gamma\text{-Fe}_2\text{O}_3$  promotes the formation of peroxy-radicals, converting  $\text{Fe}^{\text{III}}$  into  $\text{Fe}^{\text{II}}$  species (Equation (1)); the new formed species are themselves involved in the conversion of TBHP into tert-butoxy-radicals, restoring the +3 oxidation state of iron atoms (Equation (2)). Therefore, due to this extra side reaction, we ended up with an extra consumption of TBHP in the case of the reaction performed with IONs. Since we clearly observed an iron-catalyzed side reaction that could potentially alter the nature of our magnetic phase, thus endangering the whole aim of magnetic recoverability, we measured again the magnetization of our samples, recovered after performing the reaction. We decided to check the eventual loss of magnetization for the selected IONs and SC2 samples, being the latter, in our opinion, the best candidate to be chosen as support for the next functionalization strategy toward the preparation of novel metal containing catalysts.

## 2.6 Experimental

### 2.6.1 Synthesis of iron oxide magnetic nanoparticles (IONs)

0.86 g of  $\text{FeCl}_2 \cdot 4\text{H}_2\text{O}$  and 2.33 g of  $\text{FeCl}_3 \cdot 6\text{H}_2\text{O}$  in deionized water (40 mL) were kept under stirring at 85 °C for 60 min, under nitrogen gas atmosphere, in a 250 ml round-bottom flask. Upon addition of ammonium hydroxide (30%, 2.5 ml), the solution color turned from light brown (color of the iron salts) to dark grey (color of the nanoparticles). The solution was maintained under magnetic agitation for additional 20 min in the same conditions, then it was cooled to room temperature. The liquid containing the magnetic nanoparticles was centrifuged at 5000 RPM for 20 min. Afterwards, the supernatant was discarded and the particles were washed with a NaOH solution (pH = 9) and centrifuged at 5000 RMP for 10 min (3 times) and then washed with a 0.02 M NaCl solution and centrifuged at 5000 RMP for 10 min (3 times). Finally, the precipitate was dried in air at 150 °C for 15 h.

### 2.6.2 Synthesis of silica coated magnetic nanoparticles (SC-IONs)

100 mg of IONs synthesized in the previous step were suspended in 20 ml of a water/ethanol (1:4) solution in a 50 ml two-necks roundbottom flask, at room temperature, and sonicated for 10 min. Afterwards, different amounts of tetraethyl orthosilicate (TEOS) were added to the solution (respectively 0.1 ml, 0.5 ml and 1 ml) and kept under magnetic stirring for 10 min. Finally, we dropwise added 0.37 ml of 30%

ammonium hydroxide solution. The solution was kept under vigorous stirring and inert atmosphere for 2 h. The suspension containing the SCIONs was centrifuged at 5000 RPM for 20 min. Afterwards, the supernatant was discarded, the particles were washed with absolute ethanol and centrifuged at 5000 RMP for 10 min (3 times) and then dried in air at 150 °C for 15 h.

### *2.6.3 Attenuated Total Reflectance FT-IR spectroscopy (ATR-IR)*

FT-IR measurements were performed with a PerkinElmer Spectrum Two instrument equipped with an atmospheric UATR Two accessory and a DTGS detector. Each spectrum was obtained by averaging 8 scans with 4  $\text{cm}^{-1}$  resolution in the range 4000–360  $\text{cm}^{-1}$ ; spectra are displayed in absorbance in a more restricted spectral window (1400-450  $\text{cm}^{-1}$ ).

### *2.6.4 X-ray Photoelectron Spectroscopy (XPS)*

XPS spectra were collected with a PHI 1257 system, working at a base pressure of  $10^{-9}$  Tor, equipped with a non-monochromatized Mg  $K\alpha$  X-ray source and a hemispherical analyzer. C 1s, O 1s, Si 2p and Fe 2p spectral regions were acquired at a constant pass energy of 23 eV, corresponding to an overall experimental resolution of 0.75 eV. Spectra were aligned by using the C 1s peak centered at 284.8 eV in binding energy (not showed here). Background subtraction was performed using a Shirley function.

### *2.6.5 X-ray Diffraction (XRD)*

The crystalline structure of the samples were investigated by means of X-ray diffraction (XRD) technique, using a Bruker D5000 equipped with Cu K $\alpha$  (wavelength  $\lambda = 0.154$  nm) line excitation source and in Bragg-Brentano geometry.

### *2.6.6 Alternating Gradient Field Magnetometry (AGFM)*

Magnetization curves were obtained using a PMC Micromag 2900 Alternated Gradient Field Magnetometer (AGFM) (Lakeshore Cryotronics). The sample was weighted and placed inside a homemade sampleholder. Measurements were performed at room temperature varying the magnetic field up to a maximum of 12 kOe.

### *2.6.7 Scanning Electron Microscopy (SEM)*

The study of the morphology of magnetic nanoparticles was carried out by Scanning Electron Microscopy, using a FESEM ZEISS Gemini500 instrument, acquiring images at 500k x either with transmitted or backscattered electrons and operating with an HT (accelerating voltage) equal to 20 kV. The samples were dispersed via sonication in methanol; a drop of the suspension was deposited on TEM copper grid (200 mesh) with an amorphous carbon film.

### *2.6.8 Transmission Electron Microscopy (TEM)*

TEM images were collected by using a Philips CM100 instrument equipped with a PHURONA emsis camera. The working potential was set to 100 kV; all images were collected with 450k x magnification.

### *2.6.9 Inductively Coupled Plasma-Mass Spectrometry (ICP-MS)*

ICP-MS characterization was performed with an Agilent Technologies 7500a mass spectrometer equipped with an ASX500 CETAC autosampler. A 60 s wash-up with 2% HNO<sub>3</sub> was performed in between measurements, in order to eliminate any memory effect. All measurements were performed inside an ISO-6 clean room to reduce the risk of possible environmental contamination. 5 mg of each sample were weighted in PFA vials with 50 µl of ultrapure HF, obtained by means of sub-boiling distillation system (DuoPur, Milestone, Italy), and treated inside an ultrasonic bath, at 60 °C, for 60 min. Afterwards, 250 µl of ultrapure HNO<sub>3</sub> were added to the vial, increasing the temperature of the treatment to 120 °C for 60 min. Finally, 8 ml of H<sub>2</sub>O ultrapure by Merck-Millipore purification system was added and kept at 100 °C for 60 min. The samples were centrifuged at 4000 rpm for 20 min, a second etching was carried out with 250 µl of ultrapure HNO<sub>3</sub>, and 5 ml of ultrapure H<sub>2</sub>O to recover the rest of the sample left inside the vials; the obtained solutions were diluted 1:50 to perform ICP-MS analysis. Fig. S1 in the



Supplementary Information shows the analytical curves employed to quantify Fe and Si content.

#### *2.6.10 N<sub>2</sub> adsorption measurements (BET)*

Surface area measurements were performed with the use of a Quantachrome NOVA 2200 instrument. The sample was inserted inside a calibrated-volume sampleholder and treated at 200 °C in dynamic vacuum for 2 h directly on the instrument. Surface area was measured with N<sub>2</sub> adsorption-desorption isotherms at 77K, by using BET method.

#### *2.6.11 Catalytic tests*

Liquid phase oxidation was performed using as substrate cis-cyclooctene. 0.4 mmol of substrate and 2 ml of chloroform were added inside a sealed 5 ml vial. At this point, we took a 20 µl of the solution and mixed it with 980 µl of acetone and 5 µl of mesitylene standard and injected inside an Agilent 7820 GC-FID system, equipped with a J&W HP-5 Intuvo GC fused silica column module (30 m, 0.32 mm, 0.25 µm). The sequence used for reactants and products detection is shown in Fig. S2. This acted as our starting point to calculate epoxide conversion. Afterwards 4–5 mg of each sample were added to the sealed vials and sonicated for 5 min; finally 1.2 equivalent (eq.) of oxidant (tert-Butyl hydroperoxide, TBHP, 5.5 M in n-decane) were added at different times (0.4 eq. when starting the reaction, 0.4 eq. after 1 h and 0.4 eq. after 2 h). The reaction was carried out at 60 °C under magnetic stirring for 4 h,

sampling 20  $\mu\text{l}$  of raw solution after 1, 2 and 4 h. Each sampling was taken after magnetic decantation of the catalyst, in order to avoid the injection of any particles inside the GC-MS instrument. After the reaction, we performed a magnetic decantation of the samples and removed the liquid phase; nanoparticles were washed 3 times with tetrahydrofuran and dried at RT under high vacuum.

#### *2.6.12 Iodometric back-titration*

Iodometric back-titration was performed to evaluate the residual amount of oxidant after cis-cyclooctene epoxidation. The catalyst was magnetically removed, and the reaction liquids were transferred inside a 100 ml flask. Afterwards, 3 ml of glacial acetic acid, 7.5 ml of distilled water and 0.5 ml of KI saturated solution (864 mg/ml) were added to the same flask (wrapped in aluminum foil to prevent light degradation of iodide solution) and kept under magnetic stirring for 5 min, until a deep red color was obtained. The solution was then titrated with a standardized  $\text{Na}_2\text{S}_2\text{O}_3$  0.1 N solution, using a starch paste solution as a colorimetric indicator that will turn from blue to transparent at the equivalence point.

#### *2.7 Conclusions*

In this study, we conducted a straightforward synthetic procedure aimed at preparing a series of silica-coated magnetic systems. The novelty of our work lies in the precision and diversification of the physico-chemical investigation, providing multiple pieces of evidence regarding the

effectiveness of the coating procedure, without significantly impacting the magnetic properties. Our primary objective was to address a gap in the existing literature on magnetic nanocatalysts by employing a comprehensive set of characterization techniques. This approach allowed us to conduct a thorough analysis of magnetic nanoparticles and demonstrate the efficacy of the silica coating layers through testing our core-shell supports under the same experimental conditions intended for future catalytic oxidations. The results from oxidative catalytic tests affirmed that silica coating prevents potential interference from the magnetic core in the target reactions. Furthermore, the magnetic core retains its properties substantially unchanged, regardless of the experimental conditions applied in our reactions. This was confirmed by magnetization measurements performed on the recovered samples. In conclusion, we have provided comprehensive proof of the chemical inertia of these nanostructured catalytic supports, affirming their reliability for the future development of easily recoverable heterogeneous catalysts.

## References

1. Anastas P.T., Kirchoff M.M., Williamson T.C, **2001**, *Appl. Catal. Gen.*, 221, 3–13.
2. Chassaing S., Beneteau V., Pale P., **2018**, *Curr. Opin. Green Sustain. Chem.*, 10, 35–39.
3. Deyris P.A., Grison C., **2018**, *Curr. Opin. Green Sustain. Chem.*, 10, 6–10.
4. Crucianelli M., Bizzarri B.M., Saladino R., **2019**, *Catalysts*, 9 (12), 984.
5. Martins N.M.R., Pombeiro A.J.L., Martins L.M.D.R.S., **2019**, *Catal. Commun.*, 125, 15–20.
6. Spepi A., Duce C, Ferrari C., Gonzalez-Rivera J., Jaglicic Z., Domenici V., Pineider F., Tine M.R., **2016**, *RSC Adv.*, 6 (106), 104366–104374.
7. Sun Y.K., Ma M., Zhang Y., Gu N., **2004**, *Colloid. Surface. Physicochem. Eng. Aspect.*, 245 (1–3), 15–19.
8. Kim W., Suh C.Y., Cho S.W., Roh K.M., Kwon H., Song K., Shon I.J., **2012**, *Talanta*, 94, 348–352.
9. Ruíz-Baltazar A., Esparza R., Rosas G., Perez R., **2015**, *J. Nanomater.*, 2015, 240948.
10. Wang J., Yang J., Tang Y., Liu J., Zhang Y., Liang G., Gauthier M., Karen Chen-Wiegart Y. C., Norouzi Banis M., Li X., Li R., Wang J., Sham T.K., Sun X., **2014**, *Nat. Commun.*, 5, 3415.
11. Dindarloo Inaloo I., Majnooni S., Eslahi H., Esmaeilpour M., **2020**, *ACS Omega*, 5, 7406–7417.
12. Sarkheil M., Lashanizadegan M., Ghiasi M., **2019**, *J. Mol. Struct.*, 1179, 278–288.
13. Kralj S., Drogenik M., Makovec D., **2011**, *J. Nanoparticle Res.*, 13 (7), 2829–2841.

14. Shylesh S., Schweizer J., Demeshko S., Schunemann V., Ernst S., Thiel W.R., **2009**, *Adv. Synth. Catal.*, 351, 1789–1795.
15. C.J. Cheng, C.C. Lin, R.K. Chiang, C.R. Lin, I.S. Lyubutin, E.A. Alkaev, H.Y. Lai, Synthesis of monodisperse magnetic iron oxide nanoparticles from submicrometer hematite powders, *Cryst. Growth Des.* 8 (3) (2008) 877–883, <https://doi.org/10.1021/cg0706013>.
16. Tadic M., Kralj S., Jagodic M., Hanzel D., Makovec D., **2014**, *Appl. Surf. Sci.*, 322, 255–264.
17. Tadic M., Kralj S., Kopanja L., **2019**, *Mater. Char.*, 148, 123–133.
18. Tadic M., Kralj S., Lalatonne Y., Motte L., **2019**, *Appl. Surf. Sci.*, 476, 641–646.
19. Sulek F., Drofenik M., Habulin M., Knez Z., **2012**, *J. Magn. Magn. Mater.*, 322, 179–185.
20. Farzaneh F., Asgharpour Z., **2019**, *Appl. Organomet. Chem.*, e4896.
21. Kang K., Choi J., Nam J.H., Lee S.C., Kim K.J., Lee S. W., Chang J.H., **2009**, *J. Phys. Chem. B*, 113, 536–543.
22. Gill C.S., Price B.A., Jones C.W., **2007**, *J. Catal.*, 251, 145–152.
23. Poston P.E., Rivera D., Uibel R., Harris J.M., **1998**, *Appl. Spectrosc.*, 52, 1391–1398.
24. Mohammadikish M., Masteri-Farahani M., Mahdavi S., **2014**, *J. Magn. Magn. Mater.*, 354, 317–323.
25. Li M., Zeng L., Chen Y., Zhuang L., Wang X., Shen H., **2013**, *Int. J. Photoenergy*, 2013, 352473.
26. Hu L., Percheron A., Chaumont D., Brachais C.H., **2011**, *J. Sol-Gel Sci. Technol.*, 60, 198–205.
27. Yue T., Sun W., Hu Y., Xu, **2018**, *Langmuir*, 34, 15134–15142.

28. Di Giuseppe A., Di Nicola C., Pettinari R., Ferino I., Meloni D., Passacantando M., Crucianelli M., **2013**, *Catal. Sci. Technol.*, 3, 1972–1984.
29. Garade A.C., Bharadwaj M., Bhagwat S.V., Athawale A.A., Rode C.V., **2009**, *Catal. Commun.*, 10, 485–489.
30. Schwaminger S.P., Bauer D., Fraga-García P., Wagner F.E., Berensmeier S., **2017**, *Cryst. Eng. Comm.*, 19, 246–255.
31. Marchetti F., Pettinari C., Di Nicola C., Pettinari R., Crispini A., Crucianelli M., Di Giuseppe A., **2010**, *Appl. Catal. A Gen.*, 378, 211–220.
32. Legros J., Bolm C, **2003**, *Angew. Chem. Int. Ed.*, 42, 5487–5489.
33. Stephenson N.A., Bell A.T., **2005**, *J. Am. Chem. Soc.*, 127, 8635–8643.
34. Barton D.H.R., Le Gloahec V.N., **1998**, *Tetrahedron*, 54, 15457–15468.
35. Kholdeeva O.A., **2013**, *John Wiley & Sons Inc., Hoboken (US)*, 127–219.
36. Barton D.H.R., Le Gloahec V.N., Patin H., Launay F., **1998**, *New J. Chem.*, 22, 559–563.

### **3. Catalytic oxygen atom transfer (OAT) promoted by tethered V(V) and Mo(VI) dioxido complexes onto silica-coated magnetic nanoparticles**

#### *3.1 Introduction*

Oxygen Atom Transfer (OAT) reactions play a pivotal role in various chemical transformations, encompassing a wide range of catalytic processes that involve the transfer of oxygen atoms between reactants. These reactions are essential in the synthesis of diverse organic compounds, pharmaceuticals, and materials. The mechanism typically involves the transfer of an oxygen atom from a donor molecule to an acceptor molecule, leading to the formation of new oxygen-containing functionalities. The use of transition metal catalysts, has been widely explored in OAT reactions due to their ability to facilitate the activation of oxygen-containing substrates. Additionally, bioinspired catalysts, including metalloenzymes like cytochrome P450, have been studied for their capability to mediate OAT reactions under mild conditions. Recent advancements in OAT reactions have also focused on developing sustainable and environmentally friendly methodologies, showcasing the significance of this field in the pursuit of efficient and green chemical processes [1]. For this type of reaction, we have developed the catalysts at the core of this study.

After optimizing the synthesis of the core and coating, we obtained a easily functionalizable support to use in catalysis. We decided to heterogenize both high-valent vanadium (IV) and/or molybdenum (VI)

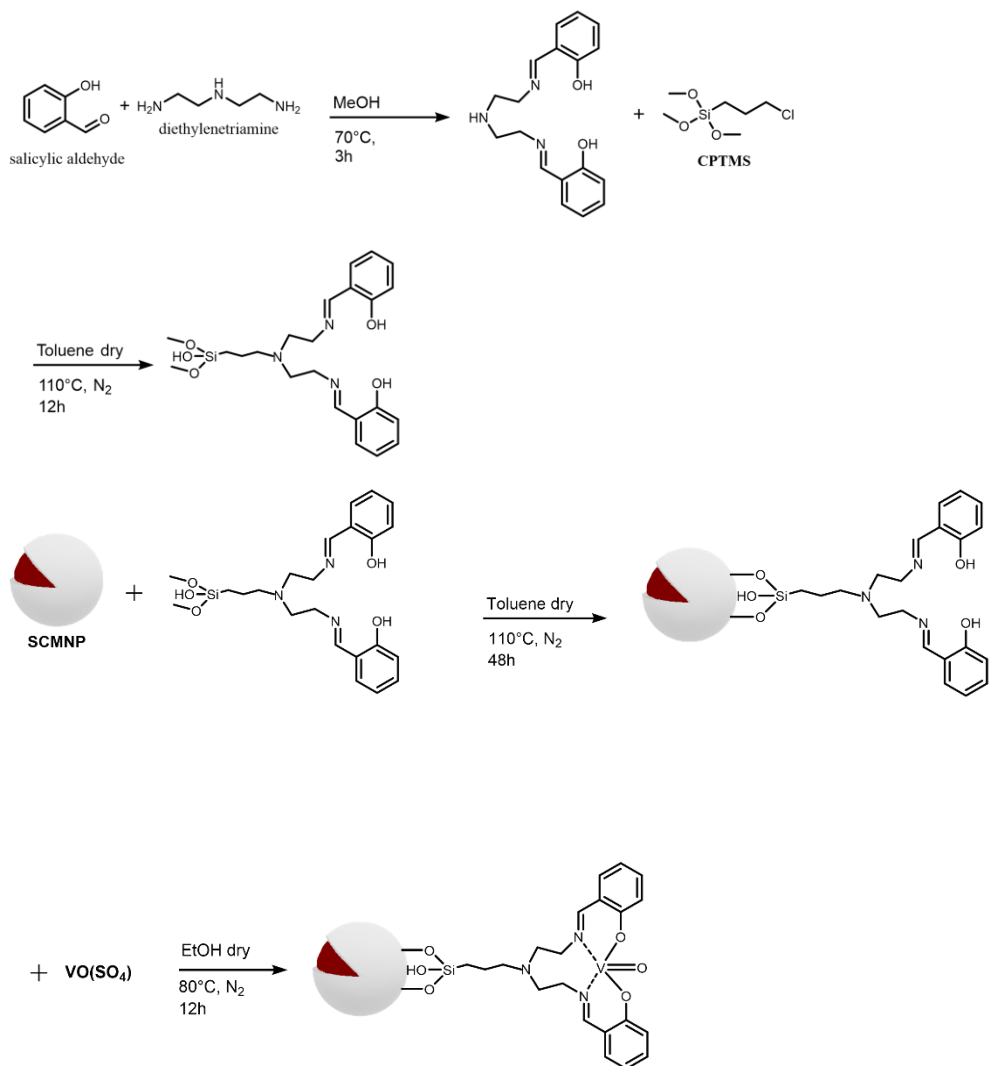
organometallic complexes on the previously synthesized and characterized supports. Propyl silane linkers with different terminations, depending on the chosen ligand, were grafted onto the silica coating. Once the support with the linker was obtained, we proceeded to load the organometallic complex, consisting of acylpyrazolonate ligands and molybdenum oxide. The selected reaction to test the reactivity of these catalysts was the selective oxidation of double bonds in various olefins.

The strength of these catalysts lay not only in their high selectivity towards the desired product but also in their easy recyclability and stability in both organic and aqueous solvents. Once again, characterization was crucial and thorough. In addition to the techniques used in the previous work, NMR was employed to determine the structure of the ligands, and TGA was used to quantitatively assess the loading of the complex after heterogenization.

### *3.2 Synthesis of heterogeneous Vanadium (IV) catalyst*

Initially, a Vanadium (IV) complex with a SALPR-like ligand was synthesized for the purpose of heterogenizing it onto the previously optimized coated core. The synthetic procedure is depicted in the Scheme1.

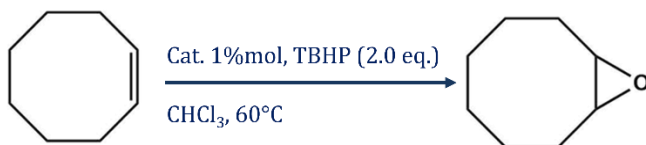




Scheme 1. Summary of the synthetic procedure for Vanadium based heterogeneous catalyst.

Through ICP-MS analysis, it was determined that the loaded metal percentage of vanadium was 8.4%. This catalyst was tested in the epoxidation reaction of *cis*-cyclooctene, and the experimental conditions are outlined in the Scheme2. The vanadium-based catalyst has been tested in various solvents to optimize reaction conditions. The catalyst

performs very well in chloroform and acetonitrile, moderately well in dichloroethane, and almost not at all in ethanol. This suggests that protic solvents are not suitable for this type of system, while chlorinated or coordinating solvents, such as acetonitrile, yield better results. It is also worth noting that in almost all solvents, the reaction is selective for epoxide formation. In the reaction in chloroform, there is also a small percentage of glycol, likely due to an overoxidation reaction, which is possible because the oxidant, TBHP, is aqueous. As chloroform shows the most promising results, it was chosen to conduct the initial catalytic tests.

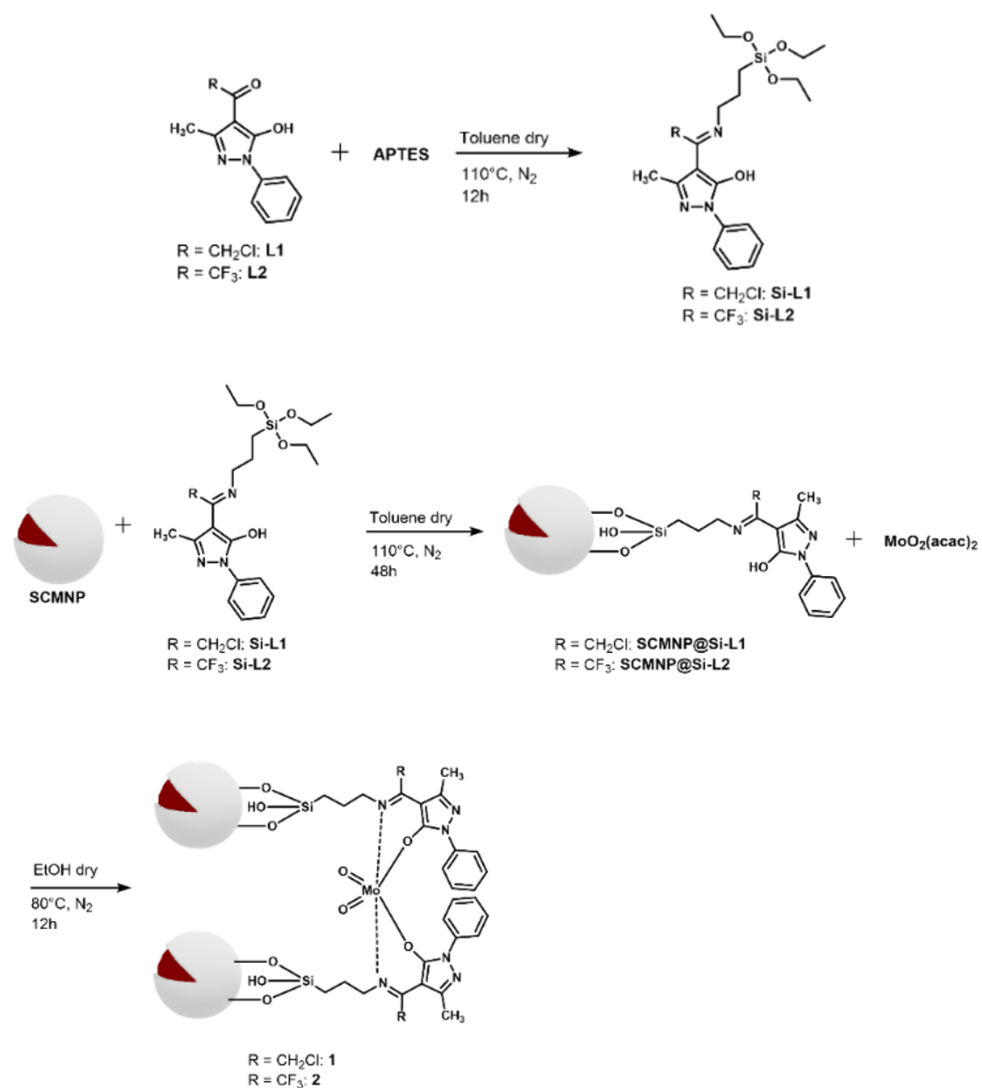


Scheme 2. Experimental conditions tested in the *cis*-cyclooctene reaction.

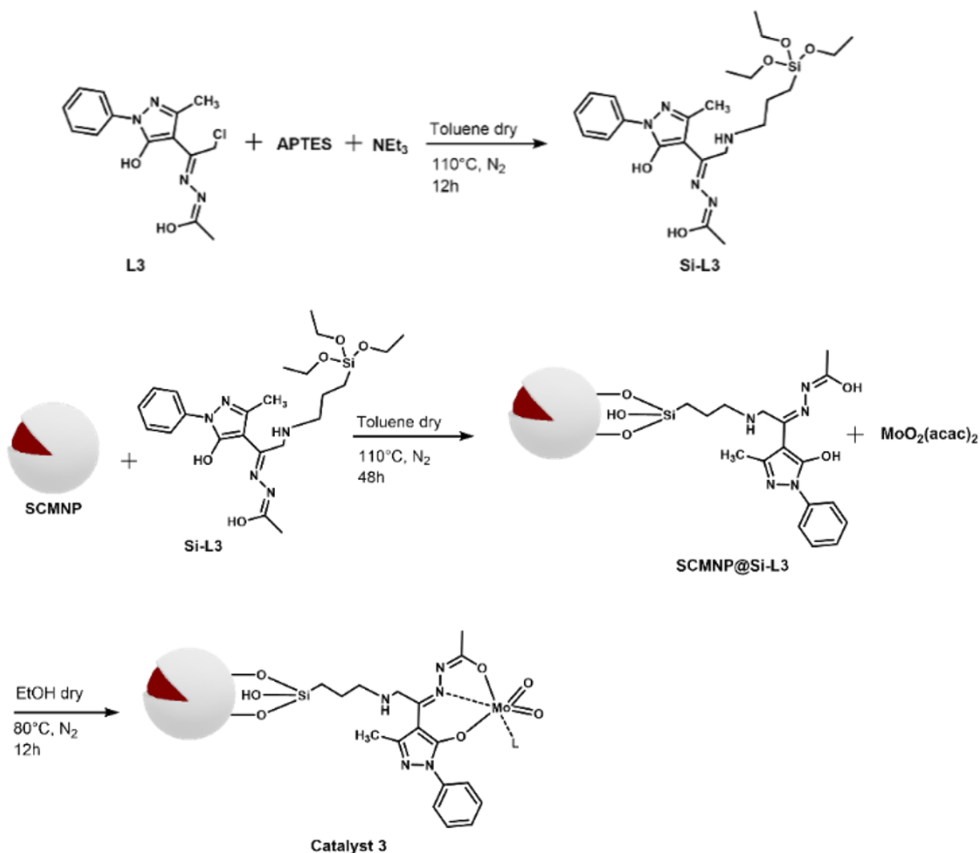
The obtained results appeared very promising, achieving a substrate conversion of 96% with a selectivity for the epoxide of 98%. Subsequently, the catalyst was recycled and tested again in the same reaction. Unfortunately, after the first recycling, the conversion dropped from 96% to 52%, indicating a significant metal leaching, thus impeding good recyclability.

Since the primary goal of this work is focused on the goal of catalyst recycling, our attention shifted towards the synthesis and study of Molybdenum (VI) complexes.

### 3.3 Synthesis of the heterogeneous catalysts 1–3



Scheme 3. Summary of the synthetic procedure for SCMNP, ligands Si-L1 and Si-L2, heterogeneous supports SCMNP@Si-L1 and SCMNP@Si-L2 and catalysts 1 and 2.



Scheme 4. Summary of the synthetic procedure for ligand Si-L3, heterogeneous support SCMNP@Si-L3 and catalyst 3.

The synthetic procedure we have followed for the preparation of the magnetically active heterogeneous catalysts 1–3, are outlined in Schemes 3 and 4. Briefly, the functionalized acylpyrazolones L1 and L2 or the corresponding N-acyl hydrazone derivatized L3 were initially reacted with APTES to obtain the corresponding silylated derivatives Si-L1, Si-L2 and Si-L3. These compounds, become prone to be grafted onto previously synthesized silica-coated magnetic nanoparticles SCMNPs [2], thus obtaining the heterogeneous supports SCMNP@Si-L1, -L2 or -L3 (Schemes 3 and 4). The supports were then loaded with the proper

amount of the molybdenum precursor  $\text{MoO}_2(\text{acac})_2$ , to obtain the final cis-dioxido-Mo(VI) complexes 1–3 (Schemes 3 and 4).

### *3.4 Characterization of heterogeneous molybdenum-based catalysts 1–3 and their precursors*

The silylated ligands Si-L1, Si-L2 and Si-L3 were characterized by means of NMR spectroscopy. In the case of Si-L1 and Si-L2 substrates, the formation of imine bond is clearly confirmed by the appearance of (C=N) peaks at 166.5 and 167.0 ppm, respectively, in their  $^{13}\text{C}$  NMR spectra. For Si-L1, in the  $^1\text{H}$  NMR spectrum, it is also visible the presence of Si-O-Et chemical shifts, occurring at 3.84–3.50 ppm for methylene groups and 1.23–1.20 ppm for the methyl ones; while, for Si-L2 ligand, the same signals fall at 3.69–3.66 ppm and 1.22–1.18 ppm, respectively. The presence of the signals from such chemical species is an indication of the integrity of the ethoxyl groups and the absence of hydrolysis during the synthesis, being their presence necessary for the following anchoring process. Also ligand SiL3 possesses proton signals from such groups at 3.68–3.43 ppm and 1.34–1.28 ppm, respectively. However, in the  $^{13}\text{C}$  NMR spectrum, the presence of the carbon imine group signal (165.8 ppm) in the latter molecule, confirms that the presence of the N-acylhydrazone species is maintained during the silylation step; indeed, the silyl derivatization of L3 is reached via a  $\text{S}_{\text{N}}2$  reaction, between L3 and APTES, with the elimination of HCl and the formation of a secondary amine function (66.0 ppm, for the –N– –C–CH<sub>2</sub>–NH– methylene group).

FT-IR is one of the most sensitive and versatile non-destructive techniques when dealing with chemical species identification. By monitoring the various synthetic steps, it is possible to have a layer-by-layer picture, highlighting the difference between each step. In our study, being the ligands employed to anchor the cis-MoO<sub>2</sub> species very similar among them, we decided to report only the case for the synthetic procedure of catalyst 1. Figure 12 the ATR-FT-IR spectra of SCMNPs (black curve), Si-L1 (blue curve), SCMNP@Si-L1 (red curve) and catalyst 1 (light blue curve) are reported. SCMNPs were largely described in our previous work [2]: briefly, the most prominent features are the symmetric (signal v at 800 cm<sup>-1</sup>) and antisymmetric (signal ii at 1060 cm<sup>-1</sup>) stretching of Si-O bond from silica coating [3], and the band at 535 cm<sup>-1</sup> assigned to Fe-O stretching (signal vi) [4]. The silylated linker shows the typical Si-O stretching in the 1200–1000 cm<sup>-1</sup> region, and several in-plane (1550–1250 cm<sup>-1</sup>) and out-of-plane (900–600 cm<sup>-1</sup>) bending modes of the several C-H species across the whole spectral range. Our target though, was the formation of a Schiff-base via imine formation: the observation of a band centered at 1634 cm<sup>-1</sup> and assigned to C=N stretching mode (signal i) confirms the presence of this new bond [5]. The final support synthesized after anchoring the silylated ligand onto SCMNPs shows the combination of the vibrational bands of the two previous samples, proving the occurring of the linking process. In the end, the molybdenum active species, was efficiently loaded onto the support, as confirmed by the appearance of the symmetric (signal iv) and antisymmetric (signal iii) stretching modes of cis-MoO<sub>2</sub> at 907 and 943 cm<sup>-1</sup> respectively [7,8]. The coordination of the metal species occurs

at the imine site, demonstrated by the shift of C=N stretching from 1634 to 1624  $\text{cm}^{-1}$  (signal i') [9].

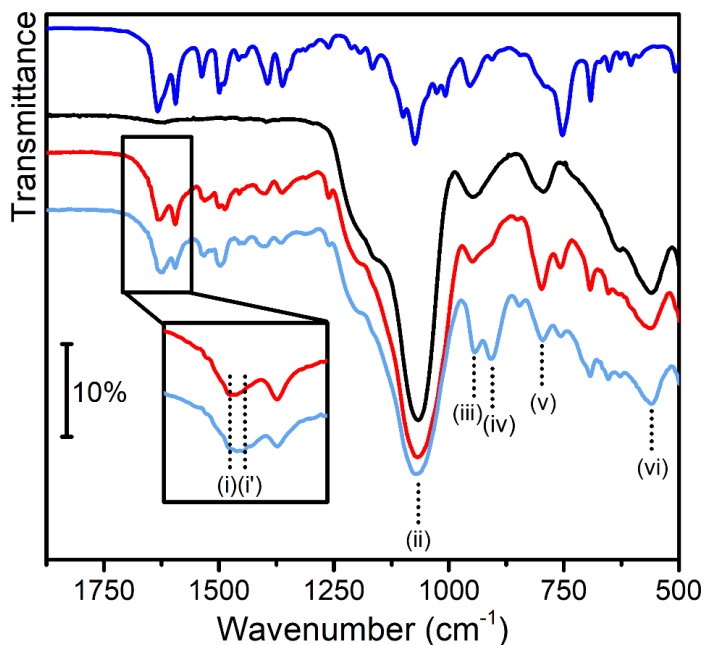


Figure 12. ATR-FT-IR spectra in the 1900-500  $\text{cm}^{-1}$  range of SCMNPs (black curve), Si-L1 (blue curve), SCMNP@Si-L1 (red curve) and catalyst 1 (light blue curve). Inset shows a magnification relative to C=N chemical species.

The amount of ligand loaded onto the SCMNPs supports was evaluated by means of TG analyses (assuming the ligands as the only organic component), while the metal loading in the final catalysts was determined by ICP-MS analyses. The samples SCMNP@Si-L2 and SCMNP@Si-L3 showed a similar ligand loading value (1.03 and 1.12  $\text{mmol}(\text{ligand})/\text{g}(\text{sample})$ , respectively), but lower with respect to SCMNP@Si-L1 [1.65  $\text{mmol}(\text{ligand})/\text{g}(\text{sample})$ ] (Table 4). Regarding the metal loading, the data from elemental analyses gave quite scattered average values (7.2% for catalyst 1, 4.1% for catalyst 2, 10.9% for catalyst 3) (Table 4), calculated on a duplicated synthetic experiments.

However, if we consider the ratio between the amounts of the different silylated ligands and Mo loading, we observe an interesting trend: catalysts 1 and 2 were synthesized using ligands having a quite open coordination site for the metal active species, giving a possible coordination mode where two acylpyrazolone ligands are necessary to bind the cis-MoO<sub>2</sub> active species, thus giving a stable complex where each ligand binds in a N,O bidentate mode the metal (Scheme 3 and Table 7), with a ligand/Mo ratio of 2.12 and 2.40, respectively). Conversely, catalyst 3 was prepared using a ligand having a potential O,N,O-tridentate chelating coordination site (due to the presence of a N-acyl hydrazone species), thus justifying the possibility of a single ligand coordinating the cis-MoO<sub>2</sub> active species, otherwise potentially still coordinated to one other ligand (i.e. L = EtOH) (see Scheme 4 and Table 7), with a Ligand/Mo ratio of 0.99). Despite the combined data from ICP-MS and TGA seems to go in this intriguing direction, we do not have direct observation of this phenomenon for the heterogeneous phase; however, in the case of homogeneous catalysts, the bidentate ligand with two acylpyrazolone molecules having open coordination sites is often observed for dioxido molybdenum complexes [10].



**Table 4.** Ligand loading data (determined by TGA) for SCMNP@Si-L1, SCMNP@Si-L2, SCMNP@Si-L3, and Mo loading factor (L.F.) data (determined by ICP-MS) for catalysts **1**, **2** and **3**.

Catalyst	TGA			ICP-MS		Ligand/Mo loading ratio
	Ligand fragment weight (Da)	Weight loss (%)	Ligand loading (mmol/g)	% <sub>w</sub> Mo	Mo L.F. (mmol/g)	
<b>1</b>	291	48.7	1.65	7.2	0.78	2.12
<b>2</b>	310	31.8	1.03	4.1	0.43	2.40
<b>3</b>	314	35.3	1.12	10.9	1.13	0.99

### *3.5 Catalytic olefins oxidation study: reaction in organic solvents*

The three novel synthesized molybdenum-based catalysts 1–3 were tested in olefins oxidation under various conditions, either in organic or aqueous medium. At the beginning, we focused our attention on the reaction conducted in organic solvents: during the optimization procedure, the reaction conditions were broadly varied by changing solvents, oxidants, reaction temperature and reagents (oxidants and catalysts vs. substrate) ratios. After running the catalytic study for the epoxidation of cis-cyclooctene with TBHP (the most active in comparison to H<sub>2</sub>O<sub>2</sub>) and various solvents, it was found that chloroform was the best solvent among dichloromethane, dichloroethane, acetonitrile and ethanol, showing the highest conversion (>99 %) at 60°C and 2.0 equiv. of oxidant. As already observed, the detrimental role of coordinating solvents like acetonitrile and, especially ethanol, in terms of competition with TBHP toward coordination to Mo(VI), cannot be ruled out [11,12].

The catalyst to substrate ratio was optimized at 1.0 mol % of molybdenum, corresponding to different amounts of catalysts 1–3, depending on their different loading factor (L.F.) of active metal (namely mmol of active metal per gram of support, see Table 4), thus taking into consideration the overall balance between the highest substrate conversion vs. the shortest time of reaction. Analogously, the best oxidant over substrate molar ratio was fixed at 2:1, carefully considering the same factors described for catalyst amount optimal conditions. Afterwards, we tested the catalysts at different temperatures, finding the optimal one for organic solvents being 60°C. Dealing with organic media, we selected TBHP in decane as oxidant, especially for its high solubility in organic solvents. A complete summary of catalytic tests performed in chloroform is reported in Table 5 .

**Table 5.** Summary of catalytic tests performed in CHCl<sub>3</sub>.<sup>a</sup>

Entry	Olefin	Catalyst	Time (h)	Conv. (%)	Epoxide (Y. %)	TOF (h <sup>-1</sup> ) <sup>e</sup>
1	<i>cis</i> -cyclooctene	-	4	27 <sup>b</sup>	>99	-
2	<i>cis</i> -cyclooctene	1	4	95 <sup>b</sup>	>99	23.8
3	<i>cis</i> -cyclooctene	2	4	>99 <sup>b</sup>	>99	25
4	<i>cis</i> -cyclooctene	3	4	97 <sup>b</sup>	>99	24.3
5	1-octene	1	7	94 <sup>c</sup>	>99	13.4
6	1-octene	2	7	97 <sup>c</sup>	>99	13.9
7	1-octene	3	4	65 <sup>b</sup>	97	16.3
8	1-octene	3	7	95 <sup>c</sup>	>99	13.6
9	<i>trans</i> -3-octene	1	7	98 <sup>c</sup>	>99	14
10	<i>trans</i> -3-octene	2	7	>99 <sup>c</sup>	>99	14.3
11	<i>trans</i> -3-octene	3	4	77 <sup>b</sup>	>99	19.3
12	<i>trans</i> -3-octene	3	7	>99 <sup>c</sup>	>99	14.3
13	Vinylcyclohexane	1	4	89 <sup>b</sup>	>99	22.3
14	Vinylcyclohexane	2	4	94 <sup>b</sup>	>99	23.5
15	Vinylcyclohexane	3	4	90 <sup>b</sup>	>99	22.5
16	Allylbenzene	1	7	96 <sup>c</sup>	>99	13.7
17	Allylbenzene	2	7	>99 <sup>c</sup>	>99	14.3
18	Allylbenzene	3	4	78 <sup>b</sup>	98	19.5
19	Allylbenzene	3	7	98 <sup>c</sup>	>99	14
20	styrene	1	7	75 <sup>c</sup>	29 (71) <sup>d</sup>	10.7
21	styrene	2	7	80 <sup>c</sup>	27 (73) <sup>d</sup>	11.4
22	styrene	3	4	52 <sup>b</sup>	19 (81) <sup>d</sup>	13
23	styrene	3	7	77 <sup>c</sup>	30 (70) <sup>d</sup>	11

<sup>a</sup>Experimental conditions: solvent CHCl<sub>3</sub>, substrate (0.2 M), catalyst (1.0 mol %), 60 °C; <sup>b</sup>TBHP: (2.0 eq.); <sup>c</sup>TBHP (3.0 eq.); <sup>d</sup>Yield of benzaldehyde. <sup>e</sup>TOF [Turnover frequency = mmol of converted substrate/(mmol of active metal · time of reaction)]

All catalysts showed excellent activity, whereas 2 showed slightly better activity, irrespective to the substrate employed. In order to rationalize these results, we can consider the different substituents of the Schiff-

base carbon on the acylpyrazolone ligand. In the catalyst 2, the trifluoromethyl group, due to its high electron withdrawing effect, may potentially affect the electrophilicity of molybdenum center, thus increasing its ability toward TBHP activation. A similar trend has been already observed in the selective olefin oxidation with oxovanadium complexes and H<sub>2</sub>O<sub>2</sub> [13]. Cis-cyclooctene behaved as the most reactive olefin, followed by vinylcyclohexane, reaching a quantitative or very high (88–92 %) substrate conversion within 4 h and 2.0 equiv. of TBHP (Table 5, entries 1–3 and 12–14). Their different activity might be justified in terms of internal vs. terminal double bond type. In the other studied substrates, quantitative conversions were obtained by prolonging the time of reaction (7 h) and increasing the amount of TBHP (3.0 equiv.), the only exception being the most challenging styrene, where we observed 80 % of conversion, under the more severe experimental conditions (Table 8, entry 20). Complete selectivity toward epoxide has been detected for all olefins, again with the only exception of styrene, where the benzaldehyde was obtained as the major product in comparison to styrene oxide (Table 8, entries 19–22) [11-13].

### *3.6 Catalytic olefins oxidation study: reaction in aqueous medium*

The optimal activity shown by our catalytic systems 1–3 in chloroform, prompted us to investigate their behaviour under conditions, namely in aqueous medium, also taking in consideration a potential development on the use of these heterogeneous systems, totally sustainable from an environmental point of view, aware that water solvent might affect the final product distribution. This not trivial comparative study, for the

same catalytic systems both in the organic and in the aqueous solvents, can only be carried out in the presence of stable and easily recyclable catalysts. We also decided to use a greener oxidant, such as hydrogen peroxide (30 %v/v, in aqueous solution). A complete survey of catalytic tests performed in water is reported in

**Table 6.**

**Table 6.** Summary of catalytic tests performed in water.<sup>a</sup>

Entry	Olefin	Catalyst	Time (h)	Conv. (%)	Epoxide (Y. %)	Diol (Y. %)	TOF (h <sup>-1</sup> ) <sup>e</sup>
1	<i>cis</i> -cyclooctene	-	4	18	17	83	-
2	<i>cis</i> -cyclooctene	1	6	>99	19	81	16.7
3	<i>cis</i> -cyclooctene	2	6	>99	13	87	16.7
4	<i>cis</i> -cyclooctene	3	4	82 <sup>b</sup>	21	79	20.5
5	<i>cis</i> -cyclooctene	3	6	>99	14	86	16.7
6	1-octene	1	8	94	20	80	11.8
7	1-octene	2	8	97	14	86	12.1
8	1-octene	3	4	52 <sup>b</sup>	14	86	13
9	1-octene	3	8	93	17	83	11.6
10	<i>trans</i> -3-octene	1	8	97	12	88	12.1
11	<i>trans</i> -3-octene	2	8	>99	13	87	12.5
12	<i>trans</i> -3-octene	3	4	58 <sup>b</sup>	17	83	14.5
13	<i>trans</i> -3-octene	3	8	98	12	88	12.3
14	vinylcyclohexane	1	8	98	15	85	12.3
15	vinylcyclohexane	2	8	>99	14	86	12.5
16	vinylcyclohexane	3	4	70 <sup>b</sup>	17	83	17.5
17	vinylcyclohexane	3	8	97	17	83	12.1
18	allylbenzene	1	8	84	12	88	10.5
19	allylbenzene	2	8	90	11	89	11.3
20	allylbenzene	3	4	38 <sup>b</sup>	11	89	9.5
21	allylbenzene	3	8	85	16	84	10.6
22	styrene	1	8	74	13	30 (57) <sup>c</sup>	9.3
23	styrene	2	8	81	16	32 (52) <sup>c</sup>	10.1
24	styrene	3	4	35 <sup>b</sup>	8	35 (57) <sup>c</sup>	8.9
25	styrene	3	8	75	15	33 (52) <sup>c</sup>	9.4

*Experimental conditions:* solvent H<sub>2</sub>O, substrate (0.2 M), catalyst (1.0 mol %), 60 °C, CTAB (5.0 mol %), H<sub>2</sub>O<sub>2</sub> (3.0 eq.); <sup>b</sup>H<sub>2</sub>O<sub>2</sub> (2.0 eq.). <sup>c</sup>Yield of benzaldehyde. <sup>e</sup>TOF [Turnover frequency = mmol of converted substrate/(mmol of active metal · time of reaction)]

Noteworthy, with all the studied catalysts we again obtained substrate conversion values close to completeness, working under reaction conditions extremely similar to the ones employed in chloroform (i.e. 1.0 mol % of catalyst, 3.0 equiv. of H<sub>2</sub>O<sub>2</sub>, 60°C, 8 h), the main variation being the type of oxidant. However, in order to increase the contact between catalyst, oxidant and the organic substrates, thus decreasing the activation energy of the overall process, the use of a catalytic amount (5.0 mol %) of a surfactant like CTAB, was necessary. Also in water, cis-cyclooctene showed to be the most reactive substrate, reaching the quantitative conversion to the corresponding epoxide after only 6 h, in comparison to the other olefins (8 h) (Table 9, entries 1–2 and 4): for shorter reaction time (4 h) and lower amount of oxidant (2.0 equiv.), the difference in terms of reactivity between cis-cyclooctene over all the other unconjugated olefins, is overwhelming (Table 9), compare entry 3 vs. entries 7, 11, 15 and 19). Once more, catalyst 2 showed the highest activity in all cases with conversion values of substrates ranging from 81 % (with styrene) to quantitative ones. Due to the presence of water, 1,2 diols have been the most abundant observed reaction products, with the exception of styrene, where the main oxidation product remains benzaldehyde (Table 9, entries 21–24). Since one of the main goals of our work was to synthesize supported catalysts with the possibility of easy recoverability by means of external magnetic field, we performed recyclability tests on catalyst 2, either in CHCl<sub>3</sub> or H<sub>2</sub>O with two different olefins, namely cis-cyclooctene and vinylcyclohexane, respectively (Figure13).



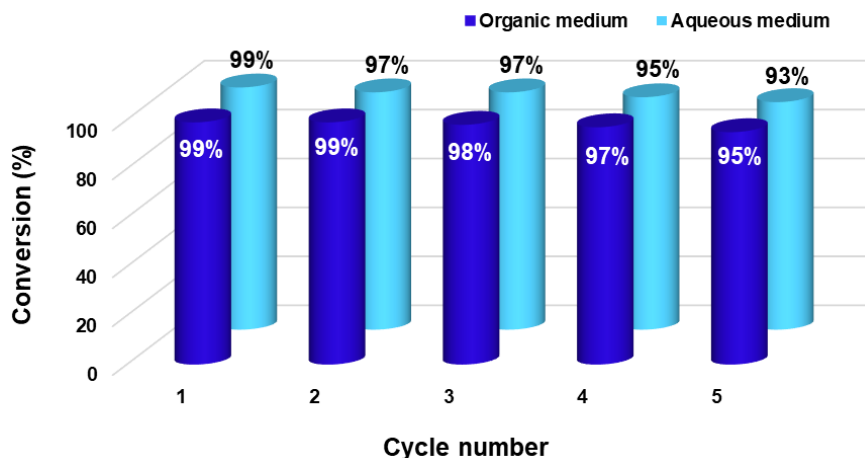


Figure 13. Recycling tests performed either in organic or aqueous solvent with catalyst **2**, relative to Entry 2 and to Entry 14 in (aqueous medium).

After each run, the catalysts were easily recovered, washed and reused for the next cycle, showing very high performances up to the 5th cycle: even if the recyclability in organic solvents was almost expected, the observed stability and recyclability of the catalyst in water, is not trivial. We are aware that acylpyrazolone-based organometallics bearing cis-dioxomolybdenum have never been anchored onto magnetic supports so far; however, the specialized literature reports other examples of Mo complexes grafted on magnetic nano-supports for oxidation of different olefins.

## 3.7 Experimental

### 3.7.1 Synthesis of Vanadium catalyst

In a 100 mL two-necked flask, 1.8 mL of salicylaldehyde is placed in 35 mL of methanol, and the mixture is stirred under nitrogen atmosphere. A solution of diethylenetriamine (0.87 mL) in 15 mL of MeOH is prepared and added dropwise using a dropping funnel. The reaction is stirred under inert atmosphere at 70°C for 1 hour. After 1 hour, a TLC (Thin Layer Chromatography) analysis is performed to verify the completion of the reaction, using a MeOH/EtOAc (80:20) eluent mixture. The product is purified using flash silica gel chromatography, starting with a MeOH/EtOAc (80:20) eluent mixture and progressing to a MeOH/EtOAc (90:10) eluent mixture. Fractions containing the product are collected, and the solvent is evaporated using a rotary evaporator. The newly synthesized Salpr sample is subsequently stored under vacuum in a desiccator. In a 50 mL flask, 0.185 mL of (3-chloropropyl)trimethoxysilane (CPTMS), and 0.3 g of Salpr in 10 mL of anhydrous toluene are placed. The reaction is stirred under nitrogen atmosphere at 110°C for 18 hours. After the reaction is complete, the solvent is evaporated using a rotary evaporator, residual toluene is removed by dichloromethane stripping, and the sample is stored under high vacuum.

In a 50 mL flask, 0.470 g of the previously obtained compound is placed in 15 mL of anhydrous toluene and sonicated to completely solubilize the ligand. To the solution, 0.1 g of magnetically coated silica cores are added, and the mixture is further sonicated to disperse the particles. The reaction is carried out under stirring in an inert atmosphere at 110°C for 48 hours. The mixture is allowed to cool to room temperature, and the functionalized nanoparticles are recovered via centrifugation at 5000 RPM for 20 minutes. Five washes with absolute anhydrous ethanol are performed in a centrifuge at 5000 RPM for 10 minutes each. The product is redispersed in ethanol, the solvent is removed again using a rotary evaporator, and finally, the sample is stored under high vacuum. In a 50 mL flask, 0.04 g of heterogenized ligand, 0.098 g of VOSO<sub>4</sub> in 10 mL of anhydrous ethanol are placed, and the mixture is sonicated to disperse the particles. The reaction is left under stirring, under nitrogen reflux, in an inert atmosphere at 80°C for 18 hours. The mixture is allowed to cool to room temperature, the reaction solvent is removed by centrifugation at 5000 RPM for 20 minutes, and five washes with absolute anhydrous ethanol are performed in a centrifuge at 5000 RPM for 10 minutes each. The product is redispersed in ethanol, the solvent is again removed using a rotary evaporator, and finally, the sample is stored under high vacuum.

### *3.7.2 Synthesis of L1 and L2 ligands*

4-chloroacetyl-3-methyl-N-phenyl-5-pyrazolone (L1) and 4-trifluoroacetyl-3-methyl-N-phenyl-5-pyrazolone (L2) ligands were

synthesized according to the procedure reported on ref. [14,15] respectively.

### *3.7.3 Synthesis of 4-chloroacetyl(N-acylhydrazone)-3-methyl-N-phenyl-5-pyrazolone (L3)*

1 ml of ethyl acetate (10.2 mmol), 800  $\mu$ L of hydrated hydrazine (9.1 mmol) and 2 ml of EtOH were placed in a microwave vial. The reaction was left at 140°C for 20 min (-230 W). Addition of 2 ml of n-hexane induced the precipitation of a white solid, which was washed with nhexane (3  $\times$  1 ml) and dried in vacuo. Yield: 700 mg (75%). Then, 0.041 g (0.55 mmol) of the previously obtained N-acetylhydrazide and 0.125 g (0.5 mmol) of L1 were added to a 25 ml round bottom and dissolved with 5 ml of EtOH. 2/3 drops of CH<sub>3</sub>COOH were then added as catalyst and the reaction was stirred under nitrogen, at 80°C for 4 h. The solution was allowed to cool slowly to room temperature and the volatiles removed under vacuum. Then, the pale yellow solid was triturated with cold diethyl ether, separated by vacuum filtration and dried in vacuo yielding L3 as white powder. Yield: 168 mg (99 %).

### *3.7.4 Synthesis of Si-L1 and Si-L2*

A bright yellow solution of L1 (0.250 g, 1 mmol) in 10 ml of anhydrous toluene was placed in a 25 ml round bottom flask and stirred under nitrogen. 0.238 ml of APTES (1 mmol) were added and the mixture was stirred under N<sub>2</sub> at 110 °C, overnight. After about 30 min the solution

changed the color from pale yellow to dark green, while after 12 h the solution turned dark brown. Once the reaction was over, the solvent was removed under vacuum, obtaining Si-L1 as a brown oil. Yield 396 mg (81%). The same synthetic procedure, starting from L2 was performed for the preparation of Si-L2, which was obtained as dark green oil. Yield 375 mg (89 %).

### *3.7.5 Synthesis of Si-L3*

200 mg of L3 (0.57 mmol) in 10 ml of anhydrous toluene were transferred to a 50 ml flask. 122  $\mu$ L of APTES (0.52 mmol) and 87  $\mu$ L of NEt<sub>3</sub> (0.62 mmol) were added and the reaction was left at 110°C under stirring, overnight. The solution was allowed to cool to room temperature and the volatiles removed under vacuum. Stripping was carried out with DCM and the precipitated salt was removed. The sample was dried under vacuum, obtaining Si-L3 as yellow oil. Yield: 357 mg (96 %).

### *3.7.6 Grafting procedures of silylated ligands Si-L1, Si-L2 and Si-L3 over SCMNPs*

Toluene were placed in a 50 ml round bottom flask and sonicated to completely solubilize the substrate. 0.1 g of SCMNPs were added to the solution and further sonicated, in order to disperse the particles. The reaction was allowed to run under stirring and inert atmosphere, at 110°C, for 48 h. It was then cooled down to R.T. and the reaction solvent was removed by centrifugation at 5000 RPM for 20 min. 4 washes were

carried out with anhydrous ethanol in centrifuge at 5000 RMP for 10min. The product was redispersed in ethanol, which was removed again in the rotavapor and finally stored under high vacuum. Compounds SCMNP@Si-L1, SCMNP@Si-L2, SCMNP@Si-L3 were obtained as reddish powder.

### *3.7.7 Synthesis of catalysts 1–3*

The metal loading procedures were performed as follows: the proper amount of both  $\text{MoO}_2(\text{acac})_2$  and the chosen ligand-anchored supports (SCMNP@Si-L1, -L2 or -L3), were added in 15 ml of ethanol, in a 1.5:1.0 M ratio with the selected ligand, placed in a 50 ml round bottom flask and sonicated to disperse the particles. The suspension was stirred under nitrogen at 80°C, for 12 h. It was allowed to cool down to R.T. and the supernatant was removed by centrifugation at 5000 RPM for 20 min. 4 washes were carried out with anhydrous ethanol in centrifuge at 5000 RMP for 10 min. The product was resuspended in ethanol, which was again removed in the rotavapor, and finally the sample was stored under vacuum. Catalysts 1, 2 and 3 were obtained as reddish powder.

### *3.7.8 General catalysis procedure: oxidation in organic medium*

0.4 mmol of olefin and 2 ml of the organic solvent were placed in a sealed batch reactor. Then 1.0 mol % of catalyst (calculated on the loaded metal) was added, and the suspension was kept under stirring until the particles

were completely dispersed. The chosen amount of tert-butyl hydroperoxide (TBHP) in decane 5.5 M was added stepwise and the reaction was left under stirring, at 60°C, until completeness.

### *3.7.9 General catalysis procedure: oxidation in aqueous medium*

0.4 mmol of olefin, 5.0 mol % of cetyltrimethylammonium bromide (CTAB) and 2 ml of water were placed in a sealed batch reactor, and 20  $\mu$ L of solution were taken for measurement of the initial substrate concentration at GC-FID. The 1.0 mol % of catalyst was added and stirred until the particles were completely dispersed. The chosen amount of hydrogen peroxide (H<sub>2</sub>O<sub>2</sub>) 30 %v/v was added stepwise, and the reaction was left under stirring, at 60 °C, until completeness.

## *3.8 Conclusion*

Within the specific context of heterogeneous catalysis, magnetic nanoparticles have been further explored as alternative catalyst supports, due to their high surface area resulting in high catalyst loading capacity, high dispersion, outstanding stability, and convenient catalyst recycling. In this work, we successfully synthesized and characterized three different Mo catalysts, based on the heterogenization of silylated acylpyrazolone derived Schiff-bases onto Silica Coated Magnetic Nanoparticles. All the catalysts showed successful ligand loading, followed by ability to anchor the cis-MoO<sub>2</sub> active species. The synthesized catalysts were employed in liquid-phase oxidation of six different olefins, giving either epoxide as main product, in the case of reaction in organic solvent, or diols, in the case of reaction performed in aqueous medium. Concerning reactions performed in organic medium, we maintained the same excellent level of substrate conversion and epoxide selectivity with respect to similar homogeneous cis-dioxidomolybdenum (VI) based catalysts [16]. Heterogenization allowed us also to perform reactions in aqueous media, usually unavailable for homogeneous acylpyrazolone-based complexes that are insoluble in water: the level of conversion pairs the one of chloroform, with a diol selectivity above 80% for all the olefins tested with catalysts 1–3. Recoverability tests by means of external magnetic field, confirmed a certain ease of recovery, coupled with excellent recyclability in both solvents, maintaining conversion level well above 90%, also after 5 reaction cycles. Nevertheless, I would like to emphasize the excellent recyclability showed by Mo complexes in water, an achievement that is far from obvious. In this way, we demonstrated the extreme robustness



and versatility of our novel synthesized cis-MoO<sub>2</sub> containing acylpyrazolone-based catalysts, in a wide variety of oxidation reaction applications. Regarding the vanadium-based catalyst, a successful heterogenization of a vanadium organometallic complex has been achieved, which proves to be particularly active and selective in the epoxidation reaction of cis-cyclooctene. Future studies will focus on optimizing the metal grafting process to reduce leaching and enable recyclability.

## References

1. Zhang R., **2018**, *Accounts of Chemical Research*, 51,701–707.
2. Lazzarini A., Colaiezzi R., Passacantando M., D’Orazio F., Arrizza L., Ferella F., Crucianelli M., **2021**, *J. Phys. Chem. Solids*, 153, 110003.
3. Martins N.M.R., Pombeiro A.J.L., Martins L.M.D.R.S., **2019**, *Catal. Commun.*, 125, 15–20.
4. Spepi A., Duce C., Ferrari C., Gonzalez-Rivera J., Jaglicic Z., Domenici V., Pineider F., Tine M.R., **2016**, *RSC Adv.*, 6, 104366–104374.
5. Ghorbani-Choghamarani A., Ghasemi B., Safari Z., Azadi G., **2015**, *Catal. Commun.*, 60, 70–75.
6. Rayati S., Khodaei E., Jafarian M., Wojtczak A., **2017**, *Polyhedron*, 133, 327–335.
7. Mohammadikish M., Masteri-Farahani M., Mahdavi S., **2014**, *J. Magn. Mater.*, 354, 317–323.
8. Chen L., Ma L., Jiang Y., Liu J., Li C., Zhang N., Wang J., **2021**, *Polym. Bull.*, 78, 415–432.
9. Chen L., Ma L., Jiang Y., Liu J., Li C., Zhang N., Wang J., **2021**, *Polym. Bull.*, 78, 415–432.
10. Hills L., Moyano R., Montilla F., Pastor A., Galindo A., Alvarez E., Marchetti F., Pettinari C., **2013**, *Eur. J. Inorg. Chem.*, 2013, 3352–3361.
11. Payami F., Bezaatpour A., Eskandari H., **2018**, *Appl. Organometal. Chem.*, 32, e3986.
12. Abdalghani I., Biancalana L., Aschi M., Pampaloni G., Marchetti F., Crucianelli M., **2018**, *Molec. Catal.*, 446, 39–48.
13. Marchetti F., Pettinari C., Di Nicola C., Pettinari R., Crispini A., Crucianelli M., Di Giuseppe A., **2010**, *Appl. Catal. A: Gen.*, 378, 211–220.

14. Shimojo K., Okamura H., Hirayama N., Umetani S., Imura H., Naganawa H., **2009**, *Dalton Trans.*, 2009, 4850–4852.
15. Jensen B.S., **1959**, *Acta Chem. Scand.*, 13, 1668–1670.
16. Brito J.A., Saffon N., Gomez M., Royo B., **2011**, *Curr. Inorg. Chem.*, 1, 131–139.

## **4. Synthesis and characterization of heterogeneous catalysts for the Suzuki reaction by magnetic induction**

### *4.1 Introduction*

Recent global concern for the environment has led to the need for production technologies with lower environmental impact in the chemical industry. The key to achieving this objective lies, in many cases, in the use of a catalyst. Selective catalytic reactions often allow for the reduction or elimination of by-products and waste and, in appropriate cases, can avoid the use of reagents that are harmful or toxic to humans and the environment. Catalysis can also lead to a reduction in the number of process phases and, consequently, make production processes more economically convenient and sustainable. Both homogeneous and heterogeneous catalysis find wide application in industry and, depending on the specific case, both can lead to considerable advantages. Heterogeneous catalysts generally offer the advantage of simple separation and recovery, are used for both gas and liquid phase reactions, and are suitable for continuous experiments within a reactor. It is in this scenario that magnetic nanoparticles find great application as catalysts as the possibility of recovery by magnetic decantation and reuse for further reaction cycles makes them a particularly attractive catalytic system and capable of dealing with current environmental problems [1].

The aim of this work was to synthesize, optimize and characterize different heterogeneous catalysts that are easily recoverable and reusable. For this purpose, four magnetic cores based on mixed iron oxides were chosen: ferrite, nickel-ferrite, cobalt-ferrite and

nickel/cobalt-ferrite. Their peculiarity lies in the fact that they can easily be recovered from the reaction medium with a magnet, at the end of each reaction. The first magnetic core chosen for this work is magnetite, a mixed iron oxide that has a simple synthesis, a low associated cost and, above all, peculiar magnetic properties. Magnetite has a crystalline system with an inverted spinel structure with the formula  $\text{Fe}_3\text{O}_4$  and the unit cell contains 32  $\text{O}^{2-}$  ions in a cubic FCC structure, 8  $\text{Fe}^{3+}$  ions distributed in the tetrahedral sites and 16 ions between  $\text{Fe}^{2+}$  and  $\text{Fe}^{3+}$  uniformly distributed between the octahedral sites. The  $\text{Fe}^{3+}$  and  $\text{Fe}^{2+}$  ions are found in a 2:1 ratio. This oxide was selected, not only for its properties, but also because its synthesis has already been extensively studied and optimized within the research group [2]. Taking this as a starting point, the aim of the work was to evaluate the influence of bimetallic cation substitution on the magnetic properties of the final catalytic system, in order to optimize the recovery via magnetic decantation and to study the effect of different nuclei on the coating process and catalytic applications. Ferrites with inverted spinel structure are expressed by the formula  $\text{AFe}_2\text{O}_4$ , where A is a divalent metal cation. The unit cell contains 32  $\text{O}^{2-}$  ions in a cubic structure with 16 octahedral and 8 tetrahedral sites occupied. 16  $\text{Fe}^{3+}$  ions are uniformly distributed between the octahedral and tetrahedral sites while 8  $\text{A}^{2+}$  ions are distributed only in the octahedral positions. The properties of ferrites are highly dependent on particle size, so changing particle size can lead to changes in several properties, including saturation magnetization and magnetic moment. Thus, surface structure and electrical/magnetic properties are strongly correlated [3]. Mixed ferrites under consideration include nickel-ferrite, cobalt-ferrite, and

nickel-cobalt-ferrite. These two metal ions were selected because they have different magnetic moments, thus resulting in different ferromagnetic properties in their respective oxides.

#### *4.2 Synthesis and characterization of magnetic cores*

For the preparation of the magnetic cores, the solvothermal synthesis method was chosen [2], as the research group has extensive knowledge and experience with this. To observe the morphology of the obtained nanoparticles, the samples were analyzed with electron microscopy. In particular, the STEM (Scanning Transmission Electron Microscope) technique which involves the use of a scanning electron microscope, set in transmission mode, more suitable for the magnetic samples with which it is often observed. Figure 14 shows the images of the various samples, on the right we observe the SEM (Scanning Electron Microscope) images obtained from the backscattered electrons signal, which provides information on the chemical composition of the sample.

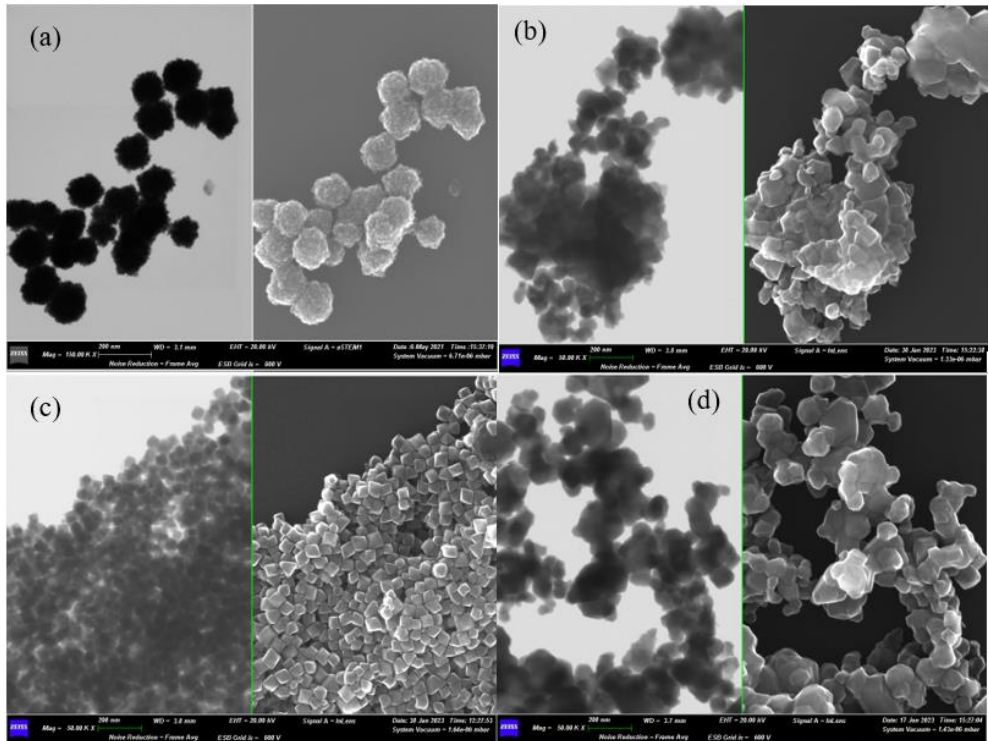


Figure 14. Comparison between the STEM (left) and SEM (right) images of the samples: a)  $\text{Fe}_3\text{O}_4$ , b)  $\text{NiFe}_2\text{O}_4$ , c)  $\text{CoFe}_2\text{O}_4$ , d)  $\text{NiCoFe}_2\text{O}_4$ .

On the left is the STEM image. In the STEM images, black and white areas are observed, the latter, in this case, indicate the presence of atoms that strongly absorb the high-energy electrons of the electron beam. This may be related to the presence of heavier elements and/or a greater density of matter in that area. As regards  $\text{Fe}_3\text{O}_4$ , no nanoparticles are observed individually, but rather aggregates with a size between 100 and 150 nm. From the images of  $\text{NiFe}_2\text{O}_4$ , particles are observed, both single and polycrystalline structures, with a polyhedral shape. It can be seen that the particles are aggregated together and are not present as single species. On average they show a size of about 40 nm.  $\text{CoFe}_2\text{O}_4$  nanoparticles instead show a homogeneous distribution of cubo-

octahedral polycrystalline structures with an average size of about 50 nm. Also in this case, polycrystalline structures are observed, since when we talk about nanoparticles larger than about 5/10 nm, it is not certain that single nanoparticles are observed but polycrystalline species may be present. Finally, the  $\text{NiCoFe}_2\text{O}_4$  particles are observed which have a structure very similar to that of  $\text{NiFe}_2\text{O}_4$  and polycrystals with an average size of approximately 60-70 nm are always observed. The samples were also characterized by ATR-IR spectroscopy (Figure 15), in order to evaluate, with a rapid analysis technique, the formation of iron oxides.

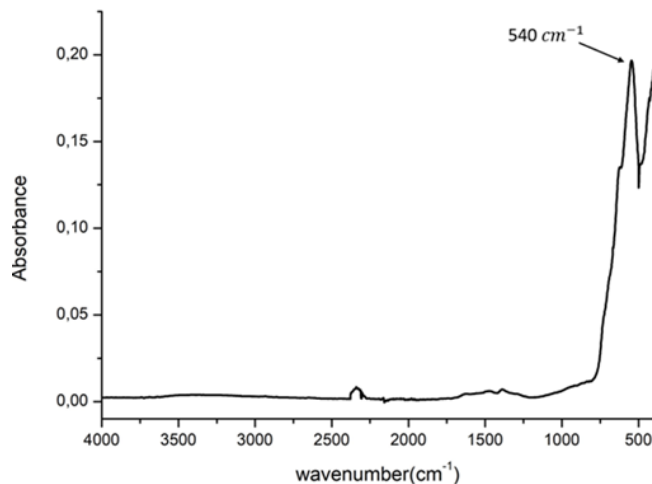


Figure 15. ATR-IR spectrum of the  $\text{Fe}_3\text{O}_4$  sample.

Typically the characteristic signals for the recognition of Ni and Co species are the signals relating to the Ni-O and Co-O stretching modes, which fall at low wavelength values [4], however given the configuration of the instrument, these signals are not detected ( $< 500 \text{ cm}^{-1}$ ). The only observable signals are those relating to Fe-O stretching, therefore only an ATR-IR spectrum will be reported which will also be taken as a reference for the others. As a first estimate we can say that the expected



iron oxide was formed thanks to the presence of the peak between 550 and 540  $\text{cm}^{-1}$ , i.e. the one relating to the stretching of the Fe-O bond. The main difference that was observed in the various ferrites is the shift of this peak, for  $\text{NiFe}_2\text{O}_4$  the stretching of the Fe-O bond was observed at approximately 543  $\text{cm}^{-1}$ .  $\text{CoFe}_2\text{O}_4$  has that same peak at 552  $\text{cm}^{-1}$  while for  $\text{NiCoFe}_2\text{O}_4$  it falls to 540  $\text{cm}^{-1}$ . These differences are due to the different composition of the oxide, by modifying the atoms close to the  $\text{Fe}^{3+}$  ion these differences can be justified. Beyond recognizing the presence of Fe-O stretching, it is difficult to obtain further information from IR spectroscopy. To investigate the crystalline structure formed and trace the composition of the iron oxides formed, X-ray diffraction measurements were performed (Figure 16).

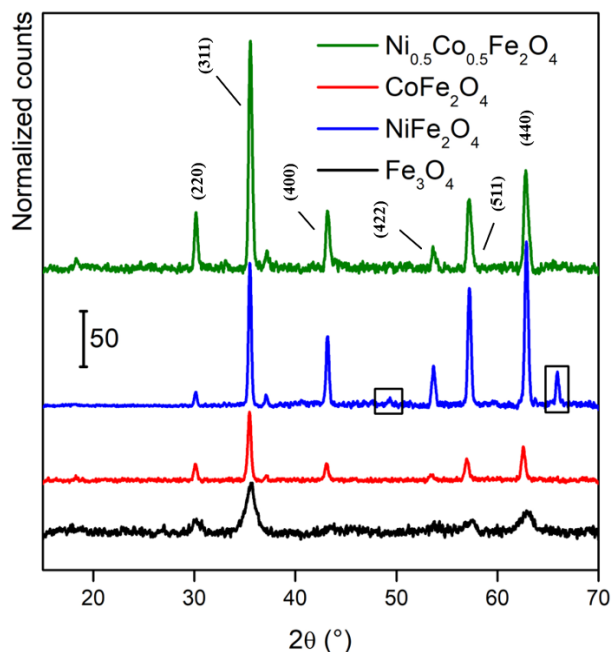


Figure 16. Comparison of the diffraction patterns of the samples.

The sample is then hit by a monochromatic radiation (Cu K<sub>α</sub>), so as to obtain a diffractogram in which the position of the peaks is linked to the elements of the cell while the shape is related to the morphology and size of the crystals. From the comparison of the diffractograms, first of all we observe the almost perfect overlap of the crystallographic peaks and this allows us to confirm, first of all, the obtaining of the oxides of interest, but also that all these oxides present a cubic inverse spinel structure. Therefore they belong to the Fd-3m space group. The diffractogram of NiFe<sub>2</sub>O<sub>4</sub> presents peaks, highlighted in the figure, which indicate the presence of impurities in the oxide formed, unlike the other oxides which appear to show a higher degree of purity. Information on the size of the crystallites can be obtained from the distribution and width of the peaks. Small crystallites have a limited number of reflection planes, unlike large crystallites which are characterized by a large number of them. Thus, the diffraction peaks generated by the constructive interference of X-rays reflected from the crystalline planes and the interference generated by a large number of planes lead to very narrow peaks. Thus, small crystallites instead show broad diffraction peaks. This behavior can be explained by the Scherrer equation [5]:

$$D = \frac{K\lambda}{B \cos(\theta)}$$

where:

D indicates the average diameter of the crystals;

B represents the width at half height of the peak (FWHM: Full Width at Half Maximum);

K is a dimension factor, it has a value of 0.9;

λ is the wavelength, it has a value of 0.154 nm.

By applying the equation it is possible to obtain the dimensions of the individual crystals.  $\text{Fe}_3\text{O}_4$  has the broadest peaks so much smaller nanoparticles are expected compared to the other samples. By applying the equation taking the most intense peak as reference, therefore the one relating to the 311 crystallographic plane, nanoparticles of approximately 10 nm are obtained. The same peak is taken as a reference for the calculation of the dimensions of the nanoparticles of both  $\text{CoFe}_2\text{O}_4$  and  $\text{NiCoFe}_2\text{O}_4$ , which show dimensions of 27 and 24 nm respectively. For  $\text{NiFe}_2\text{O}_4$ , the peak of the 440 crystallographic plane is taken as reference, the nanoparticles are 44 nm. So they are the largest obtained. The dimensions calculated with the Scherrer equation are discordant with what is reported in the STEM images, as when talking about crystallites larger than approximately 5/10 nm, it is likely that polycrystallites will be formed. So the measurements are relative to these structures, not to individual crystals. After observing the morphologies of the structures it was also necessary to investigate the magnetic properties of the different cores. The magnetic susceptibility measurements of the samples were carried out using an Alternating Field Gradient Magnetometer (AGFM). To measure magnetic susceptibility, an increasing oscillating magnetic field is applied to the sample and the trend of the magnetization of the sample is monitored.  $\text{Fe}_3\text{O}_4$  (Figure 17) shows the typical character of superparamagnetic materials, an expected behavior given the extremely small size of the nanoparticles. As explained in the introductory part, below a critical value ( $\approx 20$  nm) superparamagnetic behavior develops, as we move from a multi- to a monodomain configuration. From the curve, in fact, there is no hysteresis as the magnetic moments of the particles orient in a parallel direction,

causing the residual magnetization ( $M_r$ ) and the coercive field ( $H_c$ ) to be zero. The saturation magnetization (i.e. the maximum magnetization of the material) is approximately 54 emu/g.

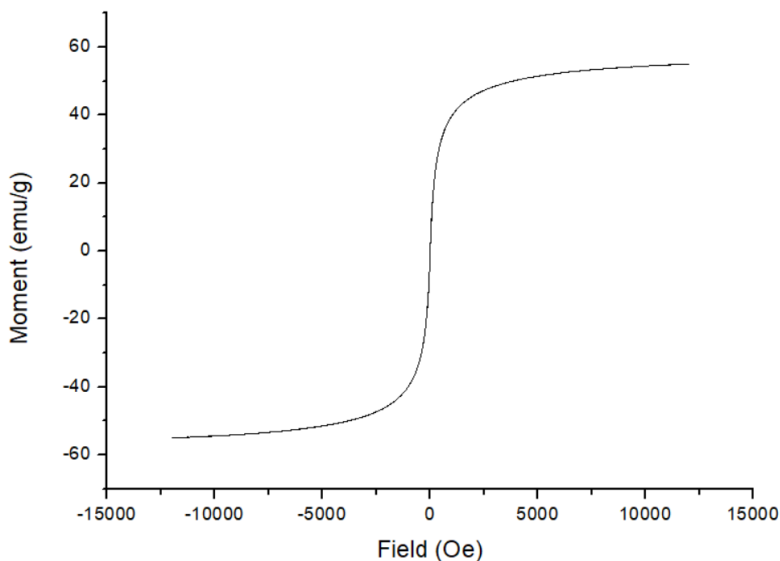


Figure 17. Magnetization curve of the Fe<sub>3</sub>O<sub>4</sub> sample

NiFe<sub>2</sub>O<sub>4</sub> has a hysteresis loop typical of soft ferromagnetic materials, i.e. it is a material with limited hysteresis and can be demagnetized at low magnetic fields. This property is also reflected in the coercivity which, as can be seen from the graph ( Figure 18), is very low for NiFe<sub>2</sub>O<sub>4</sub>. The saturation magnetization (i.e. the maximum magnetization of the material) is approximately 40 emu/g, while the residual magnetization  $M_r \approx 11$  emu/g. The main difference with Fe<sub>3</sub>O<sub>4</sub> can be seen: the addition of Ni<sup>2+</sup> ions to the structure allowed the development of ferromagnetic behaviour; in fact, residual magnetization ( $M_r$ ) and the coercive field ( $H_c$ ) are different from zero. The different behavior is mainly attributable to the larger dimensions of the nanoparticles which are above the critical value, therefore they exhibit ferromagnetic behaviour.

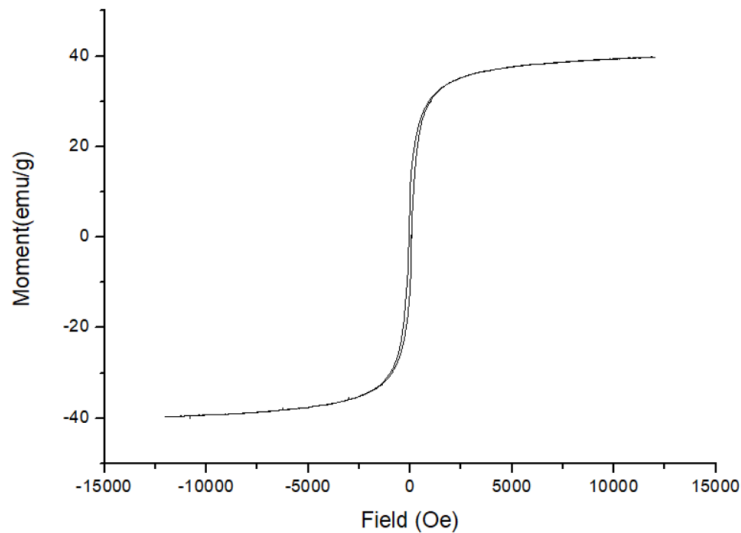


Figure 18. Magnetization curve of the NiFe<sub>2</sub>O<sub>4</sub> sample

CoFe<sub>2</sub>O<sub>4</sub> has a large hysteresis loop typical of hard ferromagnetic materials (Figure 19), which tend to be difficult to magnetize and demagnetize; in fact, they retain their magnetization even after the removal of the external magnetic field. This property is also reflected in the coercivity which, as can be seen from the graph, is greater for CoFe<sub>2</sub>O<sub>4</sub> than for the previous samples. The saturation magnetization (i.e. the maximum magnetization of the material) is approximately 68.5 emu/g while the residual magnetization value is approximately 40 emu/g. The ferromagnetic character of this sample, compared to the superparamagnetic one of Fe<sub>3</sub>O<sub>4</sub>, also in this case is mainly related to the larger dimensions of the nanoparticles. The difference in magnetic behavior between CoFe<sub>2</sub>O<sub>4</sub> and NiFe<sub>2</sub>O<sub>4</sub> is mainly attributed to the disparity of magnetic moments. In particular, Co<sup>2+</sup> has a higher magnetic moment than that of Ni<sup>2+</sup>. A further parameter that can have an effect on the magnetic behavior is attributable to the different order in the crystalline structure, a more rigid structure can influence a hard ferromagnetic character [6].

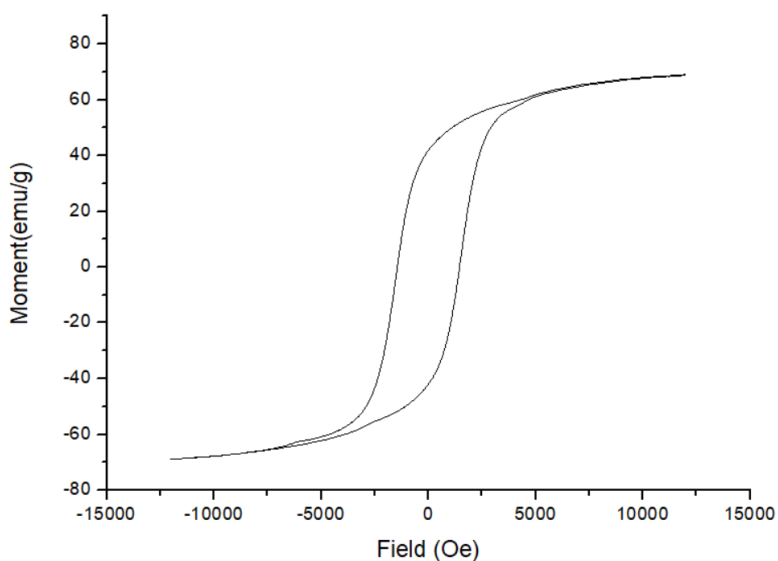


Figure 19. Magnetization curve of the  $\text{CoFe}_2\text{O}_4$  sample

Figure 20 shows an intermediate hysteresis cycle between that of  $\text{NiFe}_2\text{O}_4$  and  $\text{CoFe}_2\text{O}_4$ , so the latter core also has ferromagnetic properties. The result obtained reflects expectations, since  $\text{Ni}^{2+}$  and  $\text{Co}^{2+}$  ions have different magnetic moments. The presence of nickel ions with a lower magnetic moment therefore justifies the intermediate magnetic character. By evaluating the residual magnetization, i.e. the magnetization value of a ferromagnetic material with zero external magnetic field, a value between that of  $\text{NiFe}_2\text{O}_4$  and  $\text{CoFe}_2\text{O}_4$  is obtained. The first has a  $M_r \approx 11$  emu/g while the  $\text{CoFe}_2\text{O}_4$  which has the most intense ferromagnetic character, has a  $M_r \approx 40$  emu/g, the  $\text{Ni}_{0.5}\text{Co}_{0.5}\text{Fe}_2\text{O}_4$  has a value of approximately 26 emu/g. The saturation magnetization also has a value between that of the two oxides, it is approximately 51.7 emu/g.

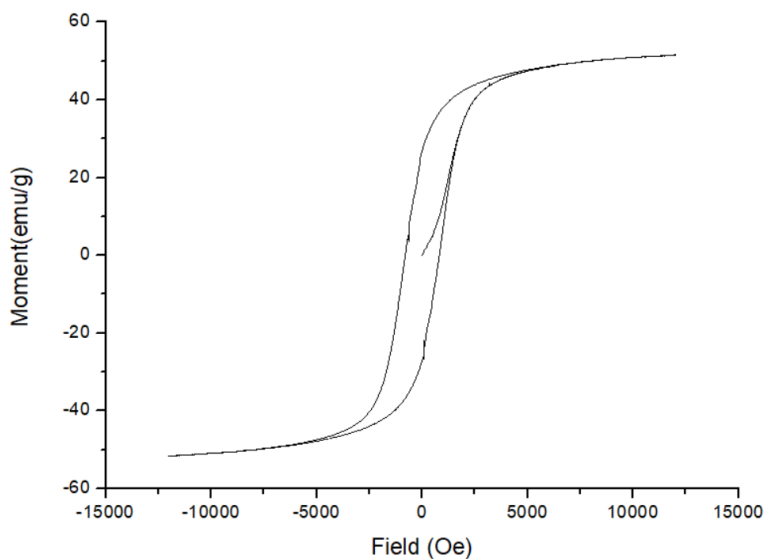


Figure 20. Magnetization curve of the NiCoFe<sub>2</sub>O<sub>4</sub> sample

Finally, the specific surface area of the nanoparticles was determined. This data is fundamental not only for their use as a support, but also for the catalytic properties of these systems, as the greater the area, the greater the quantity of active sites exposed to the reaction environment. In this work, N<sub>2</sub> adsorption isotherms at 77K were carried out to determine the surface area of the samples (Table 7).

**Table 7.** Surface area values obtained for each sample

<b>SAMPLE</b>	<b>SPECIFIC SURFACE AREA (m<sup>2</sup>/g)</b>
<b>Fe<sub>3</sub>O<sub>4</sub></b>	150
<b>NiFe<sub>2</sub>O<sub>4</sub></b>	4
<b>CoFe<sub>2</sub>O<sub>4</sub></b>	5
<b>NiCoFe<sub>2</sub>O<sub>4</sub></b>	3

After optimizing the synthesis of the magnetic cores and completing their characterization, we moved on to the optimization of the covering. Amorphous silica ( $\text{SiO}_2$ ) was chosen as coating agents, formed in-situ on magnetic nanoparticles using tetraethylorthosilicate (TEOS) as precursor. The choice fell on silica, because of an inert coating from a catalytic point of view, resistant to the reaction environment but easily functionalised.

### *4.3 Silica coating*

Various tests were carried out modifying the quantities of TEOS, in order to identify the optimal quantity to guarantee correct coverage. For the  $\text{CoFe}_2\text{O}_4$  sample, tests were carried out, both by modifying the quantity of TEOS and by evaluating how the covering varied by dispersing (or not) the nanoparticles by sonication. For the same quantity of TEOS, sonication had an important effect on the success of the coating. Due to the magnetic properties of  $\text{CoFe}_2\text{O}_4$  the nanoparticles have a high tendency to aggregate in solution so, in addition to dispersion through sonication, the suspension containing the nanoparticles was also added with a surfactant, such as CTAB. Surfactants can form a protective layer around nanoparticles, preventing them from agglomerating or clumping together. This layer can prevent interactions between nanoparticles, reducing the magnetic attraction or interference between them. Finally, surfactants can also influence the surface charge of magnetic nanoparticles. They can adsorb on the surface of particles and provide an electrostatic charge that promotes their stable dispersion, preventing



aggregation due to electrostatic repulsion forces. The syntheses were optimized on each core.

In order to evaluate the quality of the coating method, the samples, once covered, were analyzed by STEM microscopy.

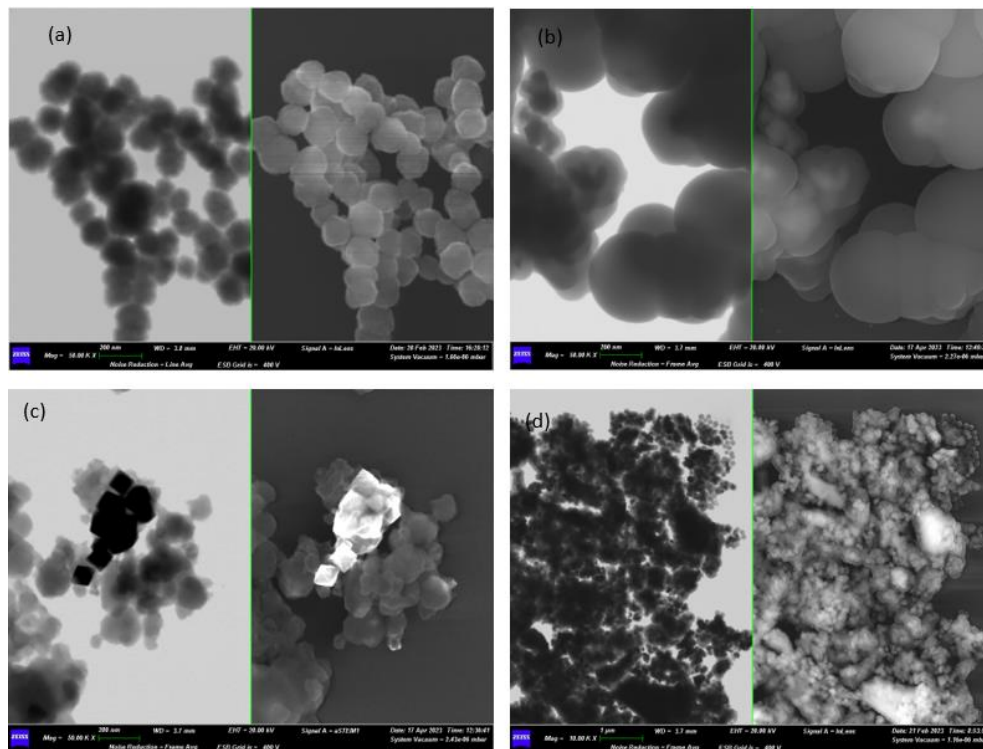


Figure 21. Comparison of STEM (left) and SEM (right) images of the samples: a)  $\text{Fe}_3\text{O}_4@SiO_2$ , b)  $\text{NiFe}_2\text{O}_4@SiO_2$ , c)  $\text{CoFe}_2\text{O}_4@SiO_2$ , d)  $\text{NiCoFe}_2\text{O}_4@SiO_2$ .

The contrast between the light and dark regions (Figure 21) allows the distinction between core and silica, as Fe atoms are heavier than Si. The study of the STEM images shows the correct covering of all four cores, as there are no dark spots (nanoparticles) without coating. The amount of silylating agent used for the cores was found to be optimal for the system under consideration, as no TEOS-only spheres were observed. Again

from the comparison between the light and dark areas, the thickness of the TEOS layer can be estimated, which is approximately 60 nm for the  $\text{Fe}_3\text{O}_4@\text{SiO}_2$  sample, 42 nm for  $\text{NiFe}_2\text{O}_4@\text{SiO}_2$ , 50 nm for  $\text{CoFe}_2\text{O}_4@\text{SiO}_2$  and 33 nm for  $\text{NiCoFe}_2\text{O}_4@\text{SiO}_2$ . From the SEM images the brightest areas can be observed, which correspond to regions in which there are more backscattered electrons, and the signal allows us to highlight the presence of on average uniform and homogeneously distributed spheres of silica. Having confirmed the correct covering of the magnetic cores, we proceeded with the complete characterization. The ATR-IR of the samples does not allow us to obtain very detailed information on the coating, we can only confirm the presence of silica by identifying its relative signals. Exactly as for the core, also in this case the peaks observed are equivalent for all the samples since only the peaks relating to silica are observed, so only an ATR-IR spectrum will be reported which will also be taken as a reference for the others.

The spectrum (Figure 22) confirms the presence of the silylating agent; in fact, the main peak is that relating to the asymmetric stretching of the Si-O bond at approximately  $1068\text{ cm}^{-1}$ . At  $952\text{ cm}^{-1}$  the symmetric stretching of the Si-O bond is observed, while at approximately  $793\text{ cm}^{-1}$  there is instead the symmetric stretching of the Si-O-Si bond. At  $563\text{ cm}^{-1}$  the peak of Si-O-Fe stretching is observed. On the other hand, a decrease in the intensity of the Fe-O symmetric stretching is observed at around  $630\text{ cm}^{-1}$ , a decrease in its intensity may be indicative of the formation of a silica shell. Finally, in the spectrum of the covered core, a shift of the peak at  $540\text{ cm}^{-1}$  relating to the Fe-O stretching is observed. IR is a technique sensitive to structural changes so the presence of silica can justify this shift.

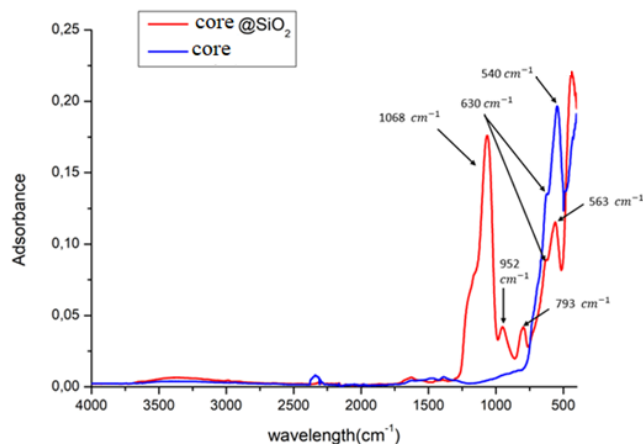


Figure 22. ATR-IR spectrum comparison of the core and core@SiO<sub>2</sub>.

Finally, the specific surface area of the covered systems was determined, the values of which are shown in Table 8.

**Table 8.** Surface area values obtained for each sample.

<b>SAMPLE</b>	<b>SPECIFIC SURFACE AREA (m<sup>2</sup>/g)</b>
<b>Fe<sub>3</sub>O<sub>4</sub>@SiO<sub>2</sub></b>	15
<b>NiFe<sub>2</sub>O<sub>4</sub>@SiO<sub>2</sub></b>	<2
<b>CoFe<sub>2</sub>O<sub>4</sub>@SiO<sub>2</sub>-T</b>	1061
<b>NiCoFe<sub>2</sub>O<sub>4</sub>@SiO<sub>2</sub></b>	20
<b>Fe<sub>3</sub>O<sub>4</sub>@SiO<sub>2</sub>-T</b>	1004
<b>NiFe<sub>2</sub>O<sub>4</sub>@SiO<sub>2</sub>-T</b>	1098

Comparing the different values obtained, the substantial difference in surface area between the various samples and the CoFe<sub>2</sub>O<sub>4</sub>@SiO<sub>2</sub>-T emerges. The result obtained on this sample is attributed to the different covering technique. For its synthesis a surfactant such as CTAB (-T in the

nomenclature of the samples) was used so as to increase the dispersion of the nanoparticles in solution. This surfactant is used as a templating agent for the synthesis of MCM-41. Consequently, the data obtained are justified by the formation of a mesoporous silica, which typically has surface area values of the order of approximately 1000 m<sup>2</sup>/g [7].

#### *4.4 Deposition of catalytically active metals*

Having found the optimal conditions for both the synthesis of the core and the coating, we moved on to the functionalization of the surface of the core covered with catalytically active metals. Functionalization allows catalytic properties to be imparted to the system. The final catalytic systems were then tested for Suzuki coupling reactions. In order to recreate the experimental conditions, the selection of transition metals such as Pd and Ru was chosen. Among the heterogeneous catalytic systems, the Pd/C-based one is the most widely used and the scientific literature contains numerous studies regarding the use of this system. So it was decided to replicate the conditions already tested aiming to deposit 10% pp of Pd and 5% pp by Ru [8], [9]. To deposit the metals on the different supports, the incipient wetness impregnation method was used, one of the most used and typical methods of deposition. This consists in suspending the core with the metal salt of interest, K<sub>2</sub>PdCl<sub>4</sub> or RuCl<sub>3</sub>·H<sub>2</sub>O, in H<sub>2</sub>O, leaving it under magnetic stirring, at R.T, for 3h. The samples were then left in an oven at 100 °C overnight and subsequently calcined at 500 °C for 5 hours with a temperature ramp of 5 °C/min. To try to reproduce the experimental conditions reported in the literature,

we tried to deposit 5% pp of Ru and 10% pp of Pd. Tests were carried out, varying the quantity of metal precursor and modifying the reaction time, so as to observe any variations in the degree of loading. With ICP-MS analysis it was possible to determine the percentage of ruthenium and palladium loaded on the surface of the different samples. Table 9 shows the comparison between the ICP-MS data of the samples, both at different reaction times and at different quantities of starting metal.

**Table 9.** Comparison between the data obtained at different quantities of metal and different reaction times.

ENTRY	SAMPLE	QUANTITY OF METAL	TIME	ICP-MS
1	Fe <sub>3</sub> O <sub>4</sub> @SiO <sub>2</sub> @Ru	5% pp	3h	1.5% pp Ru
2	Fe <sub>3</sub> O <sub>4</sub> @SiO <sub>2</sub> @Ru	5% pp	overnight	1.5% pp Ru
3	Fe <sub>3</sub> O <sub>4</sub> @SiO <sub>2</sub> @Pd	10% pp	3h	1.2% pp Pd
4	Fe <sub>3</sub> O <sub>4</sub> @SiO <sub>2</sub> @Pd	20% pp	3h	5.2% pp Pd
5	Fe <sub>3</sub> O <sub>4</sub> @SiO <sub>2</sub> @Pd	10% pp	overnight	3.0% pp Pd
6	CoFe <sub>2</sub> O <sub>4</sub> @SiO <sub>2</sub> @Ru	5% pp	3h	1.1% pp Ru
7	CoFe <sub>2</sub> O <sub>4</sub> @SiO <sub>2</sub> -T@Pd	10% pp	3h	8.2% pp Pd
8	Fe <sub>3</sub> O <sub>4</sub> @SiO <sub>2</sub> -T@Pd	10% pp	3h	4.8% pp Pd

9	NiFe <sub>2</sub> O <sub>4</sub> @SiO <sub>2</sub> -T@Pd	10% pp	3h	4.4% pp Pd
---	--	--------	----	---------------

From the results obtained by modifying the reaction time, for the loading of Ru, it emerged that an increase in this parameter does not lead to an increase in the quantity of metal deposited, as the percentage of ruthenium measured remained the same obtained at 3h (entry 1 vs 2). Tests were also carried out by increasing the initial quantity of Ru, but the results are not reported, as percentages inconsistent with what was expected were obtained. As regards Pd, contrary to what was observed for ruthenium, both the increase in the quantity of starting metal (entries 2-3) and the reaction time (entries 2-4) led to a better deposition, increasing the reaction time is approximately double that of the metal deposited on the covered core. Even for the CoFe<sub>2</sub>O<sub>4</sub>@SiO<sub>2</sub>-T system, the ruthenium deposition process was not sufficient, the percentage of deposited is far from that expected (entry 6). Contrary to the other samples, on this sample the percentage of Pd deposited is significantly higher. As reported in the previous paragraph, CoFe<sub>2</sub>O<sub>4</sub>@SiO<sub>2</sub> shows the highest value of surface area and this allows us to justify the greater loading of active metal on its surface. From the results obtained on the latter system, it was decided to reproduce the coating in the presence of CTAB on both Fe<sub>3</sub>O<sub>4</sub> and NiFe<sub>2</sub>O<sub>4</sub> (entries 8 and 9 respectively). Considering the results obtained with the other cores, Pd is the metal that in any case was deposited in higher percentages, so it was decided to continue with the optimization of its deposition condition. Significantly higher percentages of metal deposited on these cores compared to the others were obtained, under the same synthesis conditions. From the BET data, specific surface areas of 1098 m<sup>2</sup>/g were obtained for the

NiFe<sub>2</sub>O<sub>4</sub>@SiO<sub>2</sub>-T sample and 1004 m<sup>2</sup>/g for the Fe<sub>3</sub>O<sub>4</sub>@SiO<sub>2</sub>-T sample which justify the greater loading of Pd nanoparticles on the surface. Finally, the Fe<sub>3</sub>O<sub>4</sub>@SiO<sub>2</sub>@Ru and CoFe<sub>2</sub>O<sub>4</sub>@SiO<sub>2</sub>-T@Pd samples were also analyzed by STEM microscopy, in order to estimate the dimensions of the Ru and Pd nanoparticles formed and analyze their distribution on the surface of the support. From the image (Figure 23a) you can see that Ru nanoparticles have not been uniformly deposited, rather crystals distributed non-homogeneously on the surface of the support. From Figure 23b we observe the formation of small Pd nanoparticles, approximately 10 nm. These results can be a starting point for the optimization of the deposition procedure, which in the future will also be extended to ruthenium.

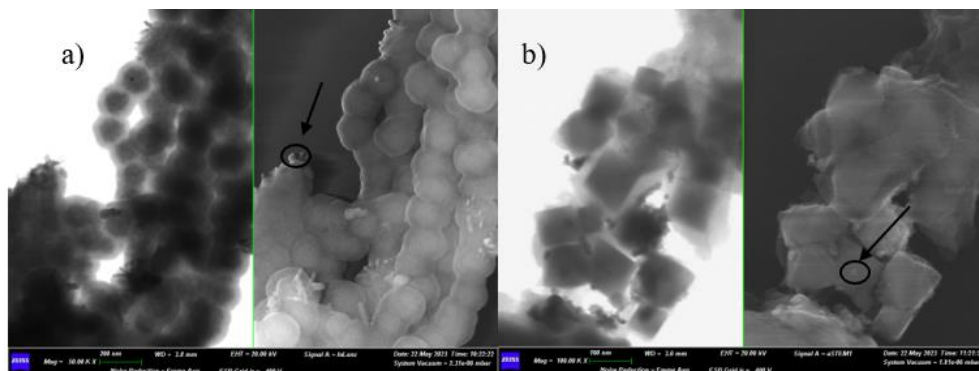
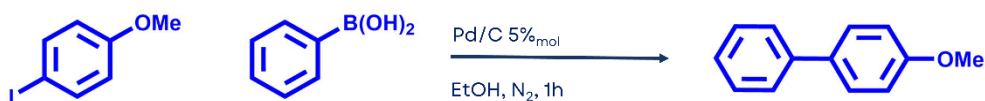


Figure 23. Comparison of STEM (left) and SEM (right) images of the samples: a) Catalyst 1 and b) Catalyst 7.

#### 4.5 Catalytic tests

The chosen reaction for testing the catalysts was the Suzuki coupling; for this reason, catalysts containing ruthenium were not tested, only those with palladium. In particular, the catalyst chosen for the initial tests was  $\text{CoFe}_2\text{O}_3@\text{SiO}_2@\text{Pd}$ . First, a comparison was made between the reaction conducted using magnetic induction and that conducted in an oil bath. The chosen conditions were those reported in the literature for a classic Suzuki reaction, as depicted in the Scheme 5 [10].



Scheme 5. Literature reaction condition for Suzuki reaction

In a Schlenk tube under an inert atmosphere, the reaction mixture was placed, and the Schlenk tube was immersed in an alternating magnetic field of 20 mT with a frequency of 254 KHz. The reaction was monitored for 1 hour every 10 minutes, and it was observed that after 60 minutes, the reaction had reached complete conversion at a temperature of 106°C, although at 99°C, the conversion was already complete after 50 minutes. To compare with the oil bath, the reaction was monitored at temperatures recorded during magnetic induction (25°C, 51°C, 73°C, 80°C, 95°C, 99°C, 106°C). It was observed that after 48 minutes, the temperature had reached 106°C, but the conversion was only 63%.



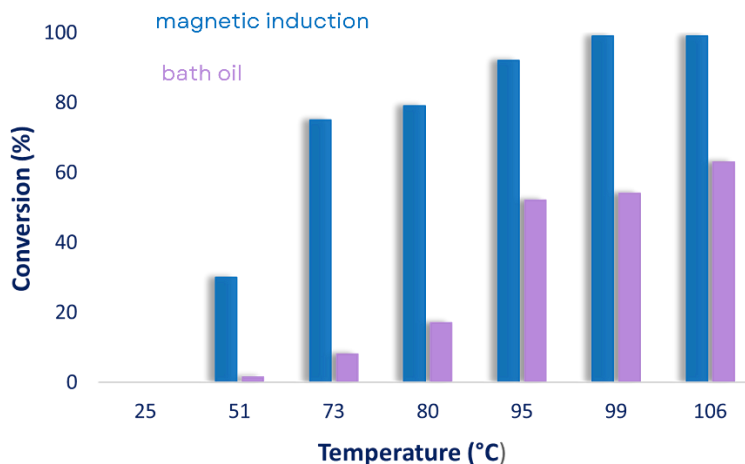


Figure 24. Comparison between bath oil and magnetic induction catalysis.

As shown in the Figure 24, not only is the conversion higher in the case of magnetic induction, but the reaction kinetics are also much faster. To ensure that the conversion of the reaction conducted via magnetic induction was due to the catalyst and not a thermal phenomenon, two controls were conducted using the  $\text{CoFe}_2\text{O}_4$  core itself and the same core coated with silica ( $\text{CoFe}_2\text{O}_4@\text{SiO}_2$ ) as catalysts. In both cases, the conversion is negligible, around 10%, demonstrating that the catalyst is indeed active, and it is the only one accountable for the conversion. Additionally, a preliminary optimization test was conducted by reducing the catalytic loading from 5% to 2%, and it was observed that after 60 minutes, at 106°C, the reaction had achieved complete conversion.

## 4.6 Experimental

### 4.6.1 Synthesis of magnetic cores

**Synthesis of Fe<sub>3</sub>O<sub>4</sub>:** 1.3 g of FeCl<sub>3</sub>·6H<sub>2</sub>O and 0.25 g of sodium citrate are introduced into 35 mL of an ethylene glycol/ethanol mixture (9:1) inside an autoclave liner, followed by sonication for approximately 10 minutes. Subsequently, 1.7 g of sodium acetate is added, and the liner is placed into the reactor (Parr 4848). The mixture is mechanically stirred, and 5 washes with nitrogen at 15 bar are carried out, removing excess pressure. Once the oxidizing atmosphere is eliminated, the reaction is left in the autoclave under agitation at 200 °C overnight. Upon completion of the reaction, the system is cooled to room temperature, and the liquid phase and formed particles are separated through centrifugation at 5000 RPM for 20 minutes. Three washes are performed with an aqueous NaOH solution at pH≈9, in a centrifuge, at 5000 RPM for 10 minutes, followed by three washes with a 0.02M aqueous NaCl solution, in a centrifuge, at 5000 RPM for 10 minutes. The sample is then dried in an oven at 150 °C overnight and subsequently recovered. A total of 351.4 mg of the sample was recovered.

**Synthesis of NiFe<sub>2</sub>O<sub>4</sub>:** 500 mg of Fe(NO<sub>3</sub>)<sub>3</sub>·9H<sub>2</sub>O and 180 mg of Ni(NO<sub>3</sub>)<sub>2</sub>·6H<sub>2</sub>O are placed in a 100 mL flask with 30 mL of EtOH. The solution is left under magnetic stirring until complete dissolution. A 3M solution of citric acid in 10 mL of EtOH is prepared and added to the one with the metal salts. The reaction is left under magnetic stirring at room temperature for 4 hours. The pH is adjusted with citric acid to approximately pH≈2, and the reaction is continued for 24 hours under the previously used conditions. The sample is dried in an oven at 80 °C overnight and subsequently calcined up to 400 °C with a temperature ramp of 2 °C/min and then up to 800 °C with a temperature ramp of 5 °C/min for 1 hour. A total of 800 mg of the sample was recovered.

**Synthesis of CoFe<sub>2</sub>O<sub>4</sub>:** 500 mg of Co(acac)<sub>2</sub>, 1.23 mg of Fe(acac)<sub>3</sub>, 846.3 mg of stearic acid, and 2.23 mL of oleic acid are introduced into a 50 mL flask with 817.5 mL of dibenzyl ether. The solution is degassed at 70 °C for 30 minutes. The mixture is transferred to the autoclave liner (Parr 4848) and left under mechanical stirring in a nitrogen atmosphere at 290 °C for 1 hour. The reaction is then cooled to room temperature, and the liquid phase and formed particles are separated through centrifugation at 5000 RPM for 60 minutes. Three washes with ethanol are performed in a centrifuge at 5000 RPM for 40 minutes. The sample is dried in an oven at 100 °C overnight. A total of 365 mg of the sample was recovered.

**Synthesis of NiCoFe<sub>2</sub>O<sub>4</sub>**: 1 g of Fe(NO<sub>3</sub>)<sub>3</sub>·9H<sub>2</sub>O, 180 g of Ni(NO<sub>3</sub>)<sub>2</sub>·6H<sub>2</sub>O, and 180.4 g of Co(NO<sub>3</sub>)<sub>2</sub>·6H<sub>2</sub>O are placed in a 100 mL flask with 60 mL of EtOH. The solution is stirred magnetically until complete solubilization. A 3M solution of citric acid in 20 mL of EtOH is prepared and added to the one with the metal salts, and the mixture is left under magnetic stirring at room temperature for 4 hours. The pH is adjusted with citric acid to achieve a pH≈2, and the reaction is continued for 24 hours under the previously used conditions. The sample is concentrated and dried in an oven at 80 °C overnight. Subsequently, the sample is calcined up to 400 °C with a temperature ramp of 2 °C/min and then up to 800 °C with a temperature ramp of 5 °C/min for 1 hour. A total of 285.4 mg of the sample was recovered.

#### *4.6.2 Coating of magnetic cores*

**Coating of Fe<sub>3</sub>O<sub>4</sub> and NiCoFe<sub>2</sub>O<sub>4</sub> with silica**: 150 mg of the chosen magnetic core is placed in a 100 mL flask with 30 mL of an H<sub>2</sub>O/EtOH solution (1:4), and it is sonicated to disperse the nanoparticles. 0.75 mL of TEOS is added under a nitrogen atmosphere, and the reaction is left under magnetic stirring at room temperature for 10 minutes. Then, 0.55 mL of a 30% aqueous solution of NH<sub>3</sub>·H<sub>2</sub>O is added dropwise, and the reaction is continued for 2 hours under the previously used conditions. The liquid phase and formed particles are separated through centrifugation at 5000 RPM for 20 minutes.

Three washes with ethanol are performed in a centrifuge at 5000 RPM for 10 minutes. The sample is dried in an oven at 150 °C overnight. A total of 318 mg of the sample was recovered. The same procedure was repeated using 1 mL of TEOS.

**Coating of NiFe<sub>2</sub>O<sub>4</sub> with silica :** 50 mg of NiFe<sub>2</sub>O<sub>4</sub> is placed in a 25 mL flask with the selected amount of TEOS (20 µL, 125 µL), 5 mL of EtOH, and 0.5 mL of H<sub>2</sub>O, and it is sonicated to disperse the nanoparticles. 0.5 mL of a 10% w/w NaOH solution is added, and the mixture is left to sonicate at room temperature for 2 hours. The liquid phase and formed particles are separated through centrifugation at 5000 RPM for 20 minutes. Three washes with ethanol are performed in a centrifuge at 5000 RPM for 10 minutes. The sample is dried in an oven at 80 °C overnight. A total of 48.9 mg of the sample was recovered.

**Coating of CoFe<sub>2</sub>O<sub>4</sub> with silica :** 50 mg of CoFe<sub>2</sub>O<sub>4</sub>, 250 mg of CTAB, and the chosen amount of TEOS (0.5 mL, 1 mL) are placed in a 100 mL flask with 25 mL of a 1M solution of NH<sub>3</sub>·H<sub>2</sub>O. The solution is left under magnetic stirring at room temperature for 18 hours. The solution is transferred to a static autoclave and left in an oven for 10 hours at 110 °C. The liquid phase and formed particles are separated through centrifugation at 5000 RPM for 30 minutes. Three washes with water are performed in a centrifuge at 5000 RPM for 30 minutes. The sample is dried in an oven at 90 °C overnight. The sample is calcined at 550 °C for 5 hours with a temperature ramp of 5 °C/min. A total of 270.6 mg of the sample was recovered.

#### 4.6.3 Metals deposition

**Ruthenium deposition :** 11.2 mg (5% w/w of Ru) of  $\text{RuCl}_3 \cdot \text{H}_2\text{O}$  and 100 mg of the selected coated magnetic core are placed in a 10 mL flask with 2.5 mL of  $\text{H}_2\text{O}$ . The solution is left under magnetic stirring at room temperature for the chosen time (3h, overnight). The sample is dried in an oven at 100 °C overnight and subsequently calcined at 500 °C for 5 hours with a temperature ramp of 5 °C/min. A total of 102.2 mg of the sample was recovered (the same procedure was performed starting from 50 mg of the chosen magnetic core).

**Palladium deposition :** 30.7 mg (10% w/w of Pd) of  $\text{K}_2\text{PdCl}_4$  and 100 mg of the selected coated magnetic core are placed in a 10 mL flask with 2.5 mL of  $\text{H}_2\text{O}$ . The solution is left under magnetic stirring at room temperature for the chosen time (3h, overnight). The sample is dried in an oven at 100 °C overnight and subsequently calcined at 500 °C for 5 hours with a temperature ramp of 5 °C/min. A total of 92.667 mg of the sample was recovered (the same procedure was performed starting from 50 mg of the chosen magnetic core).

**Reduction of metal nanoparticles:** 81.7 mg of previously functionalized core with Pd or Ru and 3 equivalent of NaBH<sub>4</sub> are placed in a 25 mL flask with 10 mL of H<sub>2</sub>O. The solution is left under magnetic stirring at room temperature for 1 hour. The liquid phase and formed particles are separated through centrifugation at 5000 RPM for 30 minutes. Two washes with water are performed in a centrifuge at 5000 RPM for 10 minutes. The sample is dried under vacuum and subsequently recovered.

#### *4.6.4 Catalytic tests*

**Magnetic induction catalysis :** 30.5 mg of phenylboronic acid, 117 mg of p-iodoanisole, 40 mg of NaOH, and 5% of the chosen Pd catalyst were placed in a Schlenk tube with 2 mL of EtOH. The tube was immersed in an alternating magnetic field of 20 mT with a frequency of 254 KHz. The reaction and temperature were measured every 10 minutes, and the conversion was monitored by GC-FID.

**Bath oil catalysis :** 30.5 mg of phenylboronic acid, 117 mg of p-iodoanisole, 40 mg of NaOH, and 5% of the chosen Pd catalyst were placed in a Schlenk tube with 2 mL of EtOH. The tube was place in a bath oil. The reaction conversion was monitored by GC-FID at the following temperatures : 25°C, 51°C, 73°C, 80°C, 95°C, 99°C, 106°C.

## 4.7 Conclusions

In conclusion, four different magnetic cores were synthesized, exhibiting diverse sizes and morphologies, but primarily distinct magnetic properties. The cores were coated with silica, resulting in two types of coatings: one with amorphous silica and the other with mesoporous silica. These distinct coatings led to different surface areas, influencing the loading of catalytically active metallic nanoparticles. Specifically, mesoporous silica resulted in a higher loading of metallic nanoparticles. The  $\text{CoFe}_2\text{O}_3@\text{SiO}_2@\text{Pd}$  catalyst was selected for testing in the Suzuki reaction. The results demonstrated that catalysis via magnetic induction proved to be more efficient than that in an oil bath. Naturally, reaction conditions still need optimization. Due to time constraints, this was not feasible, but the study is currently ongoing within the research group.



## References

1. Sharma R. K., Dutta S., Sharma S., Zboril R., Varma R. S., Gawande M. B., **2016**, *Green. Chem.*, 18, 3184.
2. Lazzarini A., Colaiezzi R., Passacantando M., D'Orazio F., Arrizza L., Ferella F., Crucianelli M., **2021**, *Journal of Physics and Chemistry of Solids*, 153, 1-12, 2021.
3. Sun L., Zhang R., Wang Z., Ju L., Cao E., Zhang Y., **2017**, *Journal of Magnetism and Magnetic Materials*, 421, 65-66.
4. Shahina S. R., Vidya S., *AIP Conference Proceedings*, **2021**, 1, 2379.
5. Patterson A. L., **1939**, *Physical Review*, 56, 978-982.
6. Maaz K., Karim S., Mashiatullah A., Liu J., Hou M.D., Sun Y.M., Duan J.L., Yao H.J., Mo D., Chen Y.F., **2009**, *Physica B*, 404, 3950-3951.
7. Kruk M., Jaroniec M., Sakamoto Y., Terasaki O., Ryoo R., Ko C. H., **2000**, *The Journal of Physical Chemistry B*, 104, 292-301.
8. Ito N., Watahiki T., Maesawa T., Maegawa T., Sajiki H., **2008**, *Synthesis*, 9, 1469.
9. Kurita T., Hattori K., Seki S., Mizumoto T., Aoki F., Yamada Y., Ikawa K., Maegawa T., Monguchi Y., Sajiki H., **2008**, *Chemistry a European Journal*, 14, 664-673.
10. Arcadi A., Cerichelli G., Chiarini M., Correa M., Zorzan D., **2003**, *Eur. J. Org. Chem.*, 4080-4086.

## **5. Synthesis of magnetic nanoparticles in deep eutectic solvents (DES)**

### *5.1 Introduction*

In recent years, there has been a growing focus within the scientific community and industry on the development of straightforward, effective, environmentally friendly, and cost-effective techniques for synthesizing organic compounds. While traditional methodologies have emphasized high-yield processes with rapid reaction times, contemporary approaches prioritize enhancing reusability, minimizing waste generation, and reducing toxicity. It is imperative to replace hazardous reagents with safer alternatives and adopt greener, more sustainable methodologies to minimize the generation of toxic byproducts [1]. Deep eutectic solvents (DESs), like an alternative type of ionic solvents to classical Ionic Liquids, have emerged as particularly promising candidates for organic synthesis due to their ability to dissolve both polar and nonpolar reactants and their facile recovery [3-6]. Initially reported in the early 21st century by Abbot and colleagues, DESs entail the combination of quaternary ammonium or phosphonium salts with an organic compound typically containing hydrogen-bond donor groups. Over time, various types of DESs with significant advantages have been synthesized [3,4]. For instance, a highly efficient DES capable of serving as a stable Lewis acid and environmentally friendly solvent for organic syntheses was recently developed through the reaction between choline chloride and zinc chloride [5-6].

This DES offers several advantages over others, including straightforward preparation, low melting point, high purity, non-toxicity, biodegradability, and cost-effectiveness. Furthermore, they exhibit a wide range of applications (Figure 25), rendering them extremely versatile systems [6].

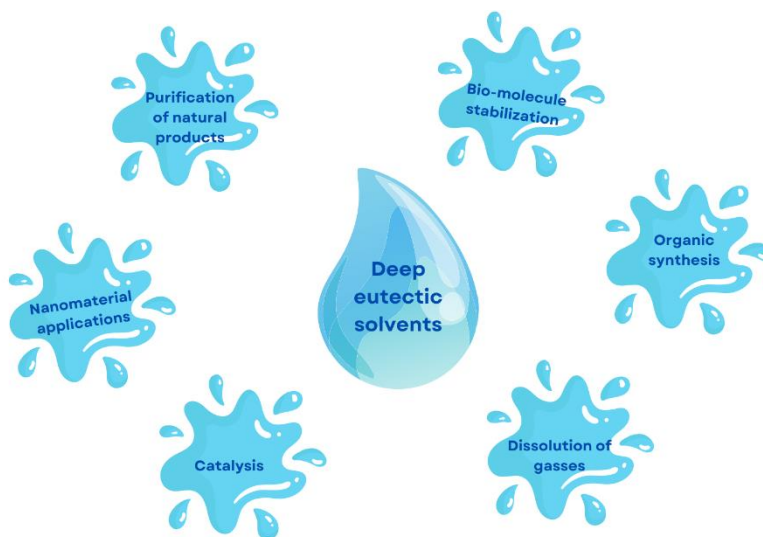


Figure 25. The main applications of deep eutectic solvents.

Another possibility for the use of DESs is the processing of metals, based on the ability to solvate a wide range of transition metal species, including metal oxides and hydroxides, without the highly acidic conditions that are needed in analogous aqueous systems. Extensive studies have been performed on the solubility of metal oxides in a variety of deep eutectic solvents [7]. Anyway, the ability of DESs to dissolve compounds like zinc oxide, magnetite, or copper oxide is not fully understood, thus further studies on the formed species have to be

undertaken, and are necessary. Despite the great potential that deep eutectic solvents play, they have some limitations that need to be solved, in order to enable their widespread use [8]. The main disadvantages include the difficulty in significantly scaling up their preparation, the viscosity and density of the materials and the prediction of their properties using theoretical methods [9]. Generally speaking, DES are formed by coupling a hydrogen bond donor and a hydrogen bond acceptor, which typically exist as solids and, at the correct ratio, produce a variably viscous liquid phase, namely DES. Ten years ago, the synthesis of magnetic Fe<sub>3</sub>O<sub>4</sub> nanoparticles, through co-precipitation, was carried out in a choline chloride/urea DES medium [10]. From a comparison with the same preparation performed in deionized water, under otherwise identical conditions, authors observed that in water Fe<sub>3</sub>O<sub>4</sub> particles were bigger (5–50 μm) and mostly irregular, if compared with analogous preparation carried out in DES. The hypothesis that some urea molecules may be adsorbed on the surface of Fe<sub>3</sub>O<sub>4</sub> particle via hydrogen bonding with the terminal hydroxyl group of the choline cation, thus affecting the magnetic particle growth, cannot be ruled out. Likewise in the spirit of seeking to analyse the role, if any, played in the growth of magnetic nanoparticles, in this study, we opted to synthesize magnetic nanoparticles in various DES to investigate how the nature of DES influences the magnetic properties and morphology of the nanoparticles.

## *5.2 Synthesis and characterization of deep eutectic solvents (DES)*

For the synthesis of nanoparticles in DES, we decided to employ the same conditions previously optimized in the hydrothermal method.

In this method, as described in Chapter 2, the use of a base is necessary. Therefore, to determine which DESs to synthesize, we considered the basicity of the two components comprising the DES. Specifically, we selected two hydrogen bond acceptors, choline chloride and guanidine chloride. Choline chloride was chosen as the starting point, being the most commonly used acceptor in the literature, while guanidinium chloride was selected for its slightly more basic character. With each of these two acceptors, we synthesized three DESs using hydrogen bond donors with different acid-base properties. A basic donor, urea (U), a neutral donor, triethylene glycol (TEG), and an acidic donor, gallic acid (GA), were chosen. After selecting donors and acceptors, the reciprocal ratios were optimized to obtain the DES (Figure 26).

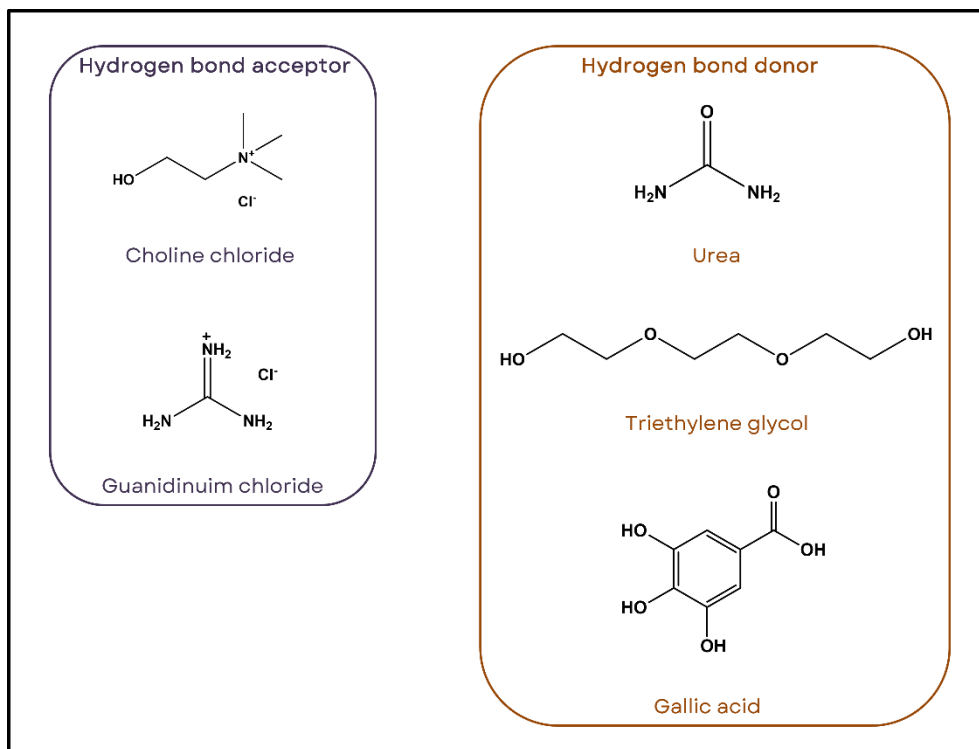


Figure 26. Hydrogen bonds acceptors and donors selected in this study.

The optimized ratios are reported in Table 13.

**Table 13.** optimized ratios for the synthesis of DES

Hydrogen bond acceptor	Hydrogen bond donor	Ratio
Choline chloride (ChCl)	Urea (U)	1:2
Choline chloride (ChCl)	Triethylene glycol (TEG)	1:3
Choline chloride (ChCl)	Gallic acid (GA)	3:1
Guanidinium chloride (GC)	Urea (U)	1:2

Guanidinium chloride (GC)	Triethylene glycol (TEG)	1:2
Guanidinium chloride (GC)	Gallic acid (GA)	-

As evident from the table, the sixth DES, intended to be composed of GC:GA, did not form despite numerous attempts at different ratios. Consequently, the study proceeded with only five DES. At this point, we proceeded with the characterization of the DESs. Firstly, we examined the phase diagram of the two DESs, GC:U and GC:TEG, which were not previously reported in the literature. Figure 27 illustrates the phase diagrams for both systems.

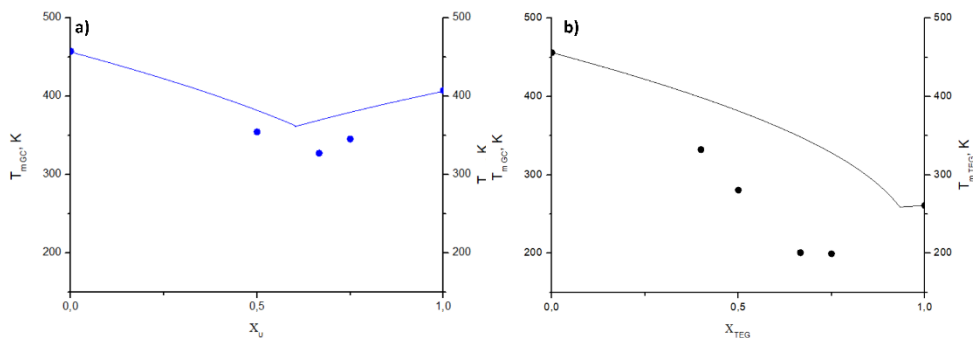


Figure 27. (a) phase diagram of the DES GU:U. (b) phase diagram of the DES GU:TEG.

In both cases, it is evident that the optimized ratios we determined (series of points) deviate from the ideal diagram (continuous line), confirming the actual formation of the DES.

The five DESs have been characterized at this stage, and their densities, viscosities, and conductivities have been measured.



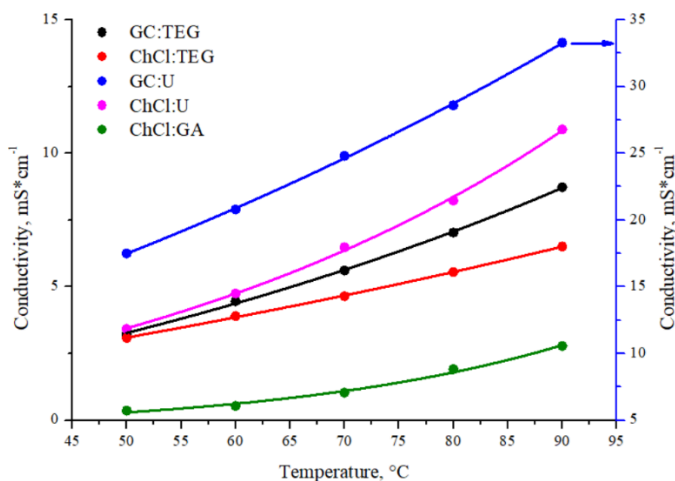


Figure 28. DES conductivity

Figure 28 depicts the conductivity graph, from which it is evident that GC:U exhibits the highest conductivity, with a value of  $33 \text{ mS}\cdot\text{cm}^{-1}$ , significantly higher than the other DESs, ranging from 3 to  $11 \text{ mS}\cdot\text{cm}^{-1}$ . This indicates that in the DES GC:U, electric charges are freer to move compared to the other samples.

After measuring conductivity, we proceeded to measure viscosity. In this case, the DESs exhibiting higher viscosity are ChCl:GA and GC:U (Figure 29).

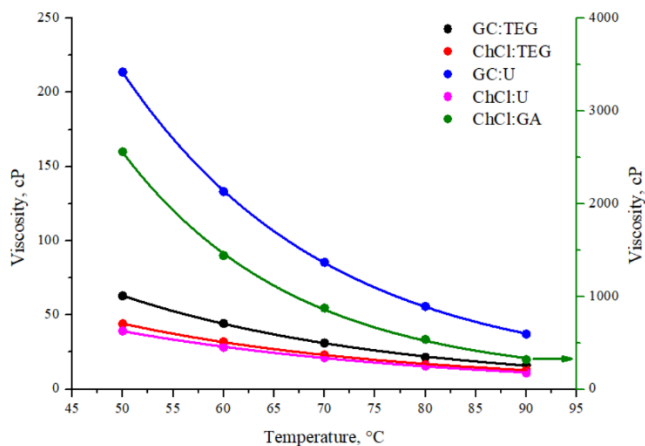


Figure 29. DES viscosity

Particularly, the ChCl:GA DES shows viscosity an order of magnitude higher than the other DESs. This parameter is crucial in the nanoparticle synthesis phase, as high viscosity could pose challenges during synthesis. Finally, to complete the characterization of the DESs, density measurements were also conducted, and the results are depicted in Figure 30. In this case, the DES displaying higher density is GC:U, whereas the one exhibiting lower density is ChCl:TEG, although regarding density, there are no very significant differences among the five DES.

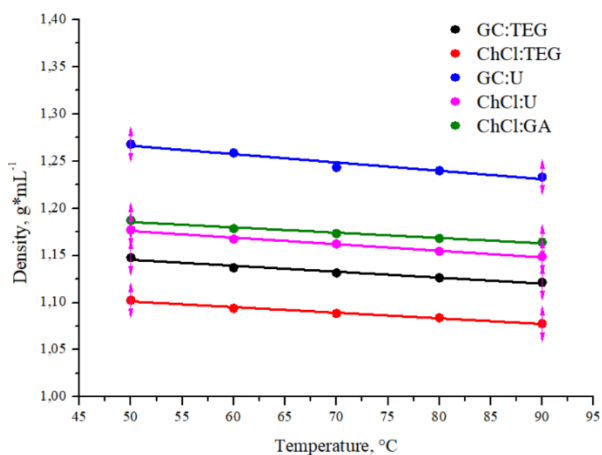


Figure 30. DES density

### 5.3 Synthesis and characterization of magnetic nanoparticles

Once the DESs were obtained and characterized, we proceeded with the synthesis and characterization of magnetic nanoparticles. As mentioned earlier, we decided to utilize the previously optimized conditions for hydrothermal synthesis, employing precipitation via pH gradient by adding a base [citation needed]. After synthesizing the five samples, we proceeded with their characterization. Firstly, we evaluated the magnetic properties of the nanoparticles. In Figure 31, the diffraction patterns of the samples are presented.

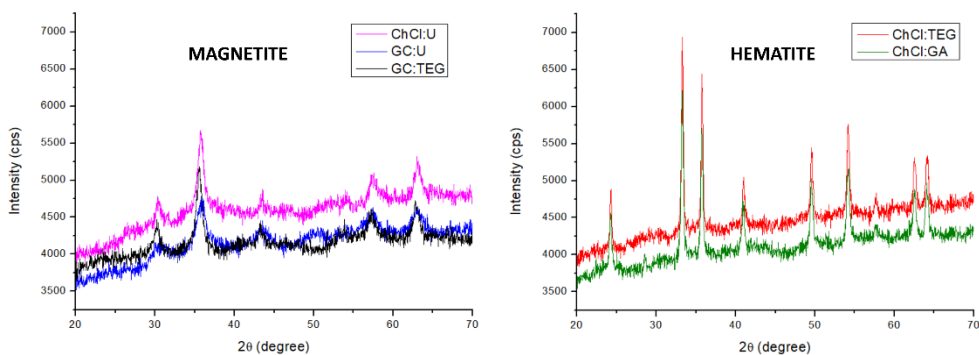


Figure 31. Diffraction patterns of the five samples of magnetic nanoparticles.

As evident from the patterns, three of them, ChCl:U, GC:U, and GC:TEG, exhibit the same pattern corresponding to magnetite, while ChCl:TEG and ChCl:GA display the pattern of hematite. These two different phases of ferrite possess distinct magnetic properties, as demonstrated by the magnetization data obtained via AGFM (Figure 32).

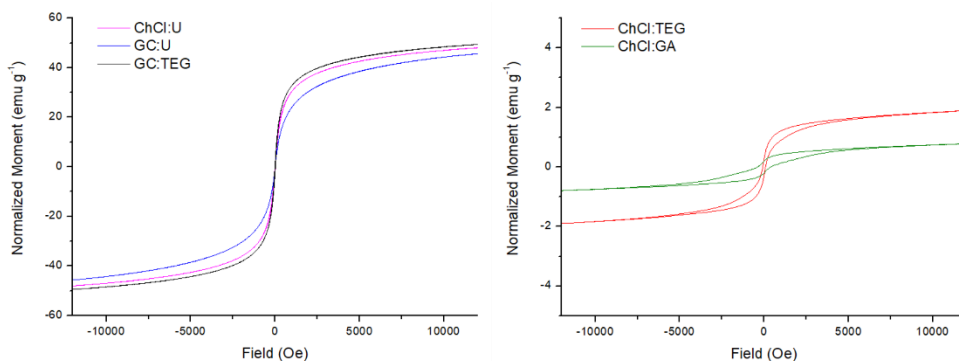


Figure 32. Normalized magnetization curves of the five samples of magnetic nanoparticles.

As evident from the magnetization curves, the samples synthesized in ChCl:U, GC:U, and GC:TEG exhibit superparamagnetic behavior with relatively high magnetization, comparable to that obtained for samples previously synthesized using the hydrothermal method. Conversely, from the curves of the samples synthesized in ChCl:TEG and ChCl:GA, it emerges that the magnetization is relatively low, as expected for hematite. Additionally, the nanoparticles exhibit hysteresis, indicating that they are not superparamagnetic. It is interesting to note that in the literature, there are few examples of magnetic nanoparticles synthesized in DES, and the most commonly used DES is ChCl:U. However, in these studies, unlike ours, magnetite does not exhibit superparamagnetic behavior, but rather a hysteresis loop is visible [11, 12]. This indicates that our conditions lead to magnetic properties that have not yet been reported. Finally, to obtain a comprehensive characterization of the nanoparticles, their morphology and dimensions were studied using electron microscopy (Figure 33). All nanoparticles exhibit very small sizes, with an average diameter around 10 nm. The main difference lies in the two samples synthesized in GC:U and GC:TEG, which appear to be more aggregated compared to the others.

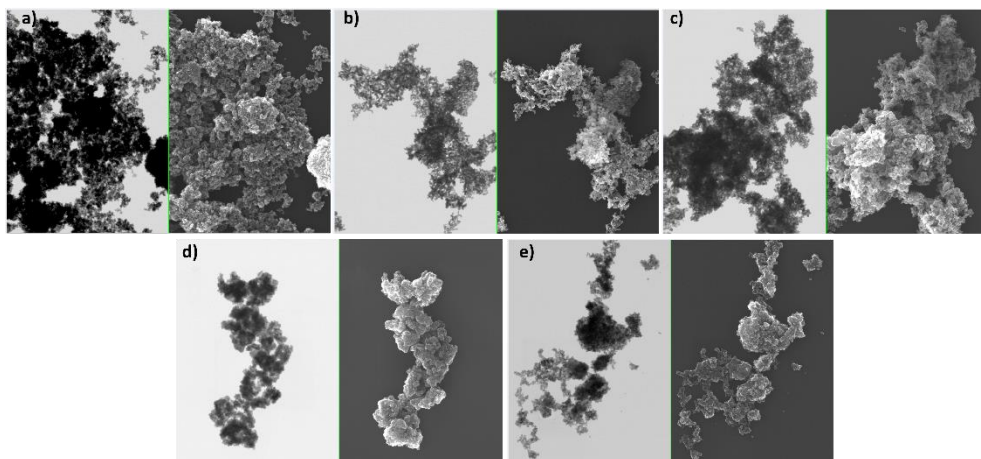


Figure 33. S-TEM images collected at 20k x magnification either in transmission (left part) or with backscattered electrons (right) of magnetic nanoparticles synthesized in ChCl:U (part a), ChCl:TEG (part b), ChCl:GA (part c), GC:U (part d) and GC:TEG (part e).

## 5.4 Experimental

### 5.4.1 Synthesis of DES

All DESs were synthesized following this procedure. The chosen amount of hydrogen bond donor and hydrogen bond acceptor (1:2 for ChCl:U, 1:3 for ChCl:TEG, 3:1 for ChCl:GA, 1 :2 for GC :U, 1 :2 for GC :TEG) is placed in a flask. The two reactants are stirred at 80°C until complete disappearance of the solid and formation of the liquid.

### 5.4.2 Synthesis of magnetic nanoparticles

0.17 g of  $\text{FeCl}_2 \cdot 4\text{H}_2\text{O}$  and 0.46 g of  $\text{FeCl}_3 \cdot 6\text{H}_2\text{O}$  in 2g of the chosen DES were kept under stirring at 85°C for 60 min, under nitrogen gas atmosphere, in a 250 ml round-bottom flask.

Upon addition of KOH (0.60 g), the solution color turned from light brown (color of the iron salts) to dark grey (color of the nanoparticles). The solution was maintained under magnetic agitation for additional 20 min in the same conditions, then it was cooled to room temperature. The liquid containing the magnetic nanoparticles was centrifuged at 5000 RPM for 20 min. Afterwards, the supernatant was discarded and the particles were washed with a NaOH solution (pH = 9) and centrifuged at 5000 RMP for 10 min (3 times) and then washed with a 0.02 M NaCl solution and centrifuged at 5000 RMP for 10 min (3 times). Finally, the precipitate was dried in air at 150 °C for 15 h.

### *5.5 Conclusions*

In this study, we aimed to demonstrate the influence of the medium in which magnetic nanoparticles are synthesized on their properties. To achieve this, we selected five different DES solvents, two of which were synthesized and characterized for the first time, as they were not previously reported in the literature. To decide which DESs to synthesize, we first chose the nanoparticle synthesis method. We opted to utilize the conditions optimized for hydrothermal synthesis, which involved the use of a base to precipitate the nanoparticles. For this reason, we considered the basicity of the hydrogen bond donors and acceptors. The five synthesized samples exhibit different morphologies and, notably, diverse magnetic properties.

In conclusion, although this work is still ongoing and we do not yet have all the information to understand why DES influence the properties of the nanoparticles synthesized in them, we can assert that this influence

exists, even if further investigation is needed to rationalize the main causes.



## References

1. Poliakoff M., Fitzpatrick J. M., Farren T. R., Anastas P. T., **2002**, *Science*, 297, 807–810.
2. Constable D. J., Curzons A. D., Cunningham V. L., **2002**, *Green Chem.* 4, 521–527.
3. Smith E. L., Abbott A. P., Ryder K. S., **2014**, *Chem. Rev.*, 114, 11060–11082.
4. Abbott A. P., Capper G., Davies D. L., Munro H. L., Rasheed R. K., Tambyrajah V., **2001**, *Chem. Commun.*, 2010–2011.
5. Abbott A. P., Capper G., Davies D. L., McKenzie K. J., Obi S. U., **2006**, *J. Chem. Eng. Data*, 51, 1280–1282.
6. Liu P., Hao J. W., Mo L. P., Zhang Z. H., **2015**, *RSC Adv.*, 5, 48675–48704.
7. Söldner A., Zach , Iwanow M., Gärtner T., Schlosser M., Pfitzner A., König B., **2016**, *Chem. Eur. J.*, 22, 13108 – 13113.
8. Długosz O., **2023**, *Materials*, 16, 627.
9. Tolmachev D., Lukashева N., Ramazanov R., Nazarychev V., Borzdun N., Volgin I., Andreeva M., Glova A., Melnikova S., Dobrovskiy A., **2022**, *Int. J. Mol. Sci.*, 23, 645.
10. Chen F., Xie S., Zhang J., Liu R., **2013**, *Materials Letters*, 112, 177–179.
11. Sri S. P. N., Taj J., George M., **2020**, *Surfaces and Interfaces*, 20, 100609.
12. Chen F., Xie S., Zhang J., Liu R., **2013**, *Materials Letters*, 112, 177–179.

## **6. Hybrid polyphenolic Network/SPIONs aggregates with potential synergistic effects in MRI applications**

### *6.1 Introduction*

Magnetic resonance imaging (MRI) contrast agents are widely used to increase the contrast difference between normal and abnormal tissues [1]. Shortly after the introduction of clinical MRI, the first contrast-enhanced human MRI study was reported in 1981 using ferric chloride as the contrast agent in the gastrointestinal (GI) tract [2]. MRI contrast agents may be generally classified according to the following features: magnetic properties, chemical composition, the presence or absence of metal atoms, different route of administration, effect on the magnetic resonance image, biodistribution, safety and application [3]. The majority of MRI contrast agents are either paramagnetic gadolinium ion complexes or superparamagnetic (iron oxide) magnetite particles. The paramagnetic contrast agents are usually made from dysprosium ( $\text{Dy}^{3+}$ ), the lanthanide metal gadolinium ( $\text{Gd}^{3+}$ ), or the transition metal manganese ( $\text{Mn}^{2+}$ ) and possess water soluble properties. The most commonly selected metal atom used in MRI contrast agents is the lanthanide ion gadolinium (III) as it possesses a high magnetic moment and it is the most stable ion with unpaired electrons. Due to the presence of unpaired electrons, these contrast agents possess paramagnetic properties. Generally, contrast agents containing gadolinium shorten the T1 (or longitudinal) and T2 (or transverse) relaxation time of neighbouring water protons, within analyzed tissues.

These effects increase the signal intensity of T1-weighted images, and reduce the signal intensity of T2-weighted images. For example, superparamagnetic iron oxide such as iron (III) oxides, are known to affect the T2 relaxation strongly [4,5].

In the realm of development of novel and more efficient contrast agents for medical diagnostic applications, is necessary to lower the dosage of such substances that might accumulate in patients with relevant toxic effects and to define new agents which effect could go beyond the simplified scheme of T1 or T2 relaxation properties.

Within this context, novel directions for MRI contrast agents based on magnetic nanoparticles entrapped inside a polyphenolic network to gain water dispersibility, were explored.

Having said this, in this part of my thesis, the use of our magnetic nanoparticles for potential applications in biological and biomedical fields, were investigated [6–8], having in mind to test their efficacy as contrast agents for MRI [9,10]. Our main goal was based on the possible preparation of dual-mode hybrid contrast agents chelating  $Gd^{3+}$  ions on the nanoparticles coating, with tunable T1 and T2 relaxation times.

Indeed, these nanoparticles should exhibit, at least from a theoretical point of view, a low intrinsic level of toxicity compared to other contrast agents like commercial products based upon Gd-organometallic complexes, till now widely used in clinical MRI applications. However, as solids (even in reduced dimensions), the stability of these systems under physiological conditions (i.e., 36–37 °C, aqueous environment, pH  $\approx$  7) is not guaranteed. Therefore, it is necessary to modify the surface of these materials to make them compatible with the operating environment.

This modification must be performed without negatively altering the crucial magnetic properties for their effectiveness.

Surface functionalization in commercially available systems of magnetic nanoparticles is already carried out using biocompatible polymers, such as dextran and its derivatives [11-12], resulting in a stable suspension in an aqueous medium. Similar results have been achieved with polyethylene glycol (PEG), through an entanglement effect between magnetic nanoparticles and PEG chains of various lengths [13,14]. Even though magnetic nanoparticles are stably suspended with these functionalizations, Gd-based contrast agents remain the preferred option in clinical practice [15,16]. However, scientific efforts are directed towards the efficient use of Gd-based contrast agents at lower dosages, aiming for improved results.

In this work, it was considered advantageous to combine the relaxivity effects of both magnetic nanoparticles and Gd ions, although the potential impact of both systems on relaxivity cannot be overlooked.

MRI contrast agents are generally classified as positive or negative. Positive agents, also known as T1 agents, induce a bright signal by reducing the longitudinal relaxation time. Negative agents, on the other hand, defined as T2 agents, induce a dark signal by shortening the transverse relaxation time. The former group typically relies on paramagnetic elements (Gd or Mn ions) while, as already said above, iron oxide particles are often the active element for the latter. Typically, polymers used as coatings for iron oxide nanoparticles lack anchoring points capable of stably coordinating Gd ions. Therefore, the aim of this research was to find innovative solutions to overcome this challenge.

The solution may come from a novel class of materials called Metal Phenolic Networks (MPNs). MPNs are a category of self-assembling materials capable of coating surfaces of different natures (oxides, polymers, 2D materials, cells, and bacteria, etc.). They are prepared by mixing polyphenolic molecules with trivalent metal ions [17,18]. Typically, Tannic Acid (TA) is the adopted polyphenol for MPN production, thanks to its widespread availability and extensive number of phenolic units. These features make it suitable for forming supramolecular coordination structures consisting of different metal ions and polyphenol units [17]. MPNs have been previously used as coatings for magnetic supports, albeit with different targeted applications. They have been employed as systems capable of adsorbing and degrading environmental pollutants [19] or as catalytic materials [20]. MPNs have also found application in biomedicine, especially in cancer diagnostics and treatment [21,22]. However, the combination of magnetic nanoparticles coated with metal phenolic networks has not been explored so far for potential MRI applications.

One of the main reasons for this gap is likely related to the intrinsic fragility of MPNs, mainly due to changes in the working pH of the solution [17]. To enhance the stability of such systems without compromising their coordinative properties, two different strategies were adopted. The first strategy is based on partial covalent bonding among TA molecules, while the second relies on the controlled reticulation of TA with a linear biocompatible polymer.

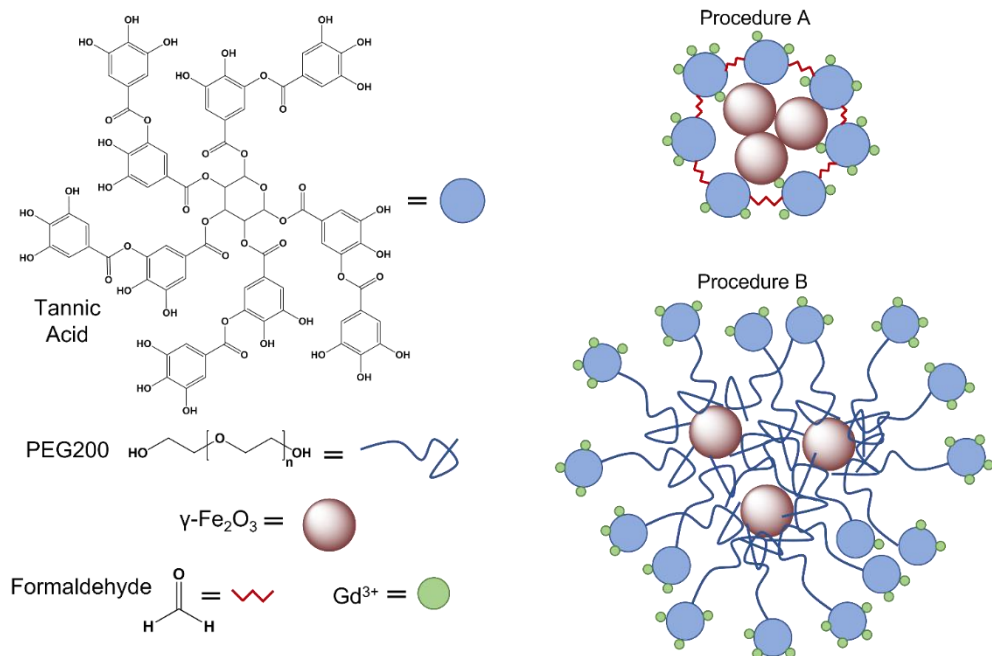
The two synthetic routes (A and B, see below, Scheme 7) are expected to yield stable phenolic-based systems, capable of improving the effective stability of coated magnetic nanoparticles in aqueous suspensions.

In procedure A, the framework surrounding the magnetic nanoparticles was created by chemically cross-linking TA molecules using formaldehyde in a basic environment (TA reticulation). Gd species were added to the formulation, either during the reticulation step or through a post-synthetic procedure (samples An). The anchoring of Gd ions was expected to follow a metal-catechol coordination assembly process (Scheme 7 - Procedure A).

In procedure B, TA PEGylation was performed in the presence of magnetic nanoparticles using the Mitsunobu polymerization reaction [23]. In this way, magnetic nanoparticles were entangled within the functionalized polymer chains (PEGylated TA). Subsequently, the coordination capabilities of the polyphenolic part of the polymer were exploited to anchor Gd species (samples Bn) (Scheme 7 - Procedure B). The two newly prepared series of samples (An and Bn) underwent complete physico-chemical characterization, including Fourier-transform infrared spectroscopy (FT-IR) and X-Ray Photoelectron Spectroscopy (XPS), thermogravimetric analyses (TGA), scanning electron microscopy (SEM), compositional (ICP-MS), and dimensional (Particle Size Distribution - DLS) analyses.

Subsequent assays were performed to evaluate their stability in a physiological buffer, and their longitudinal ( $r_1$ ) and transverse ( $r_2$ ) relaxivity values were measured. The presented results can be considered as a preliminary overview of the potential of these systems as contrast agents for magnetic resonance imaging (MRI) applications. Nevertheless, this research also aims to advance the development of dual-mode T1-T2 contrast agents beyond existing systems. Regarding the functionalization of magnetic nanoparticles, the two presented

routes are expected to produce fully customizable systems capable of carrying the desired ratio of positive/negative agents without significantly affecting suspension stability. If successful, this outcome will represent the initial step in the preparation of tunable positive-negative contrast agents, potentially tailored towards a more patient-oriented medical diagnosis.



Scheme 7. Reagents (left part) and products expected from the synthetic procedure A (right upper part) and B (right lower part).

## 6.2 Results and discussion

As previously stated, the metal-catechol coordination assembly process aimed to stabilize aqueous suspensions of SPIONs, was based on two different A and B synthetic procedures. Both procedures were optimized: in the case of route A, different SPIONs/TA and TA/formaldehyde ratios,

with different reaction temperatures were tested. For procedure B, instead, different molecular weights intervals for PEG, different PEG/TA ratios, and different reaction temperatures were considered. Herein, for both A and B procedure, only the An and Bn samples produced under optimized synthetic conditions that guaranteed a good stability in aqueous media, are reported. The synthetic differences between the two procedures could be reflected in morphological dissimilarity among them. For such reason, scanning electron microscopy (SEM) measurements were performed, either with transmitted or backscattered electrons (Figure 34).

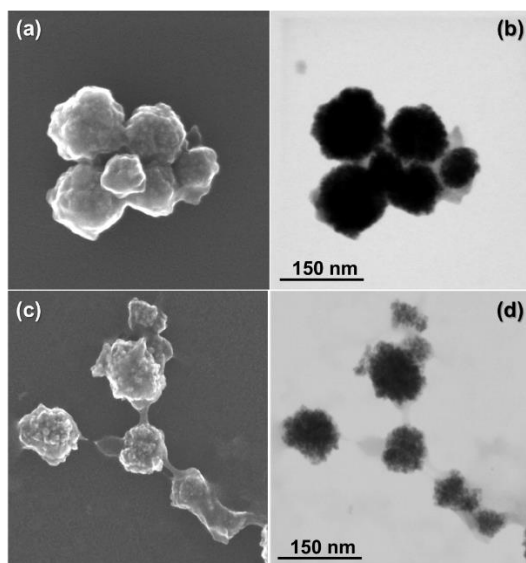


Figure 34. SEM images collected at 300kx either in transmission (b - d) or with backscattered electrons (a - c) for samples A<sub>1</sub> (a - b) and B<sub>1</sub> (c - d).

The presence of a more compact texture in the case of the sample A<sub>1</sub> was expected. In this case, the covalent binding between TA molecules



surrounding the magnetic nanoparticles create a rigid structure encapsulating them. Fig. 34a shows the complete packing of the particles in sample A1 and a loop around a small compact group of particles, indicating the formation of a rigid framework surrounding those SPIONs (Fig. 34b). Images of sample B1 collected with either backscattered (Fig. 34c) or transmitted electrons (Fig. 34d) show a less rigid system. This is evidenced by the distance present among the SPIONs, which are still connected through filaments of PEGylated TA. Comparison of A and B sample images also shows the enhanced superficial smoothness provided by the organic coating. However, picturing an image for these samples only in a dry environment (as for SEM technique) might draw to misleading conclusions for systems working in the liquid phase. To collect further dimensional data in liquid phase, thus avoiding any ambiguity, knowing the particle size distribution of all systems in aqueous medium, is mandatory. Such data were obtained by means of dynamic light scattering (DLS) measurements (Table 14).

**Table 14.** Mean particle size, Gd amount and relaxivity data ( $r_1$  and  $r_2$  parameters) for the  $A_n$  and  $B_n$  series of samples.

Sample name	Particle size (nm)	Gd content (%w/w)	$r_1$ value ( $\frac{ms^{-1}}{\mu g/ml}$ )	$r_2$ value ( $\frac{ms^{-1}}{\mu g/ml}$ )
<b>SPIONs</b>	$131.2 \pm 4.2$	-	$2.0 \cdot 10^{-5}$	$4.0 \cdot 10^{-4}$
<b>A<sub>1</sub></b>	$125.5 \pm 3.1$	4.57	$8.4 \cdot 10^{-3}$	0.97
<b>A<sub>2</sub></b>	$117.9 \pm 1.2$	0.62	$8.7 \cdot 10^{-3}$	1.22
<b>B<sub>1</sub></b>	$141.2 \pm 1.2$	-	$9.1 \cdot 10^{-3}$	1.68
<b>B<sub>2</sub></b>	$124.9 \pm 1.8$	0.66	$14.5 \cdot 10^{-3}$	0.22
<b>B<sub>3</sub></b>	$140.8 \pm 3.3$	2.64	-	-
<b>B<sub>4</sub></b>	$127.8 \pm 4.6$	12.95	-	-

For samples An, there are not consistent variations in the mean size of the aggregates, independently whether the addition of Gd<sup>3+</sup> precursor happened before (A1) or after (A2) the reticulation step. Nevertheless, it is possible to observe the formation of small populations of larger aggregates, potentially due to intermolecular H-bonding between TA molecules covering the SPIONs. However, their presence is not affecting samples stability in suspension, which are stable up to several weeks. Despite such similarities in particle dimensions, a large difference in Gd loading for the two procedures (4.6%w/w for A1 vs 0.6%w/w for A2) is displayed. Also for Bn samples, the observed average particle size does not show a clear trend in relation to Gd content. Nonetheless, it is possible to ascribe a certain tendency of the particles towards aggregation with the increase of gadolinium content. In the case of samples B1 and B2, particle size populations are pretty homogeneous. Conversely, samples B3 and B4 display a certain inhomogeneity in particle size, with the appearance of populations towards much larger dimensions than the average one. It is reasonable to expect that the presence of larger aggregates might possibly have a negative influence on the stability of the system in aqueous suspension. Such effect is potentially related to Gd amount loaded in Bn samples. Aggregation phenomenon will then tend to reduce the surface-to-bulk ratio of our systems, causing the substantial loss of solubility [58–60]. Apparently, there might also be a negative trend relating Bn samples stability and Gd content. Indeed, samples without (B1) and with the lowest amount of gadolinium (0.66 %w/w - B2) show a long stability in suspension, ending in a shelf life of the particles in aqueous medium up to several weeks. Conversely, samples potentially behaving as positive contrast agents by

carrying a higher amount of  $Gd^{3+}$  ions (B3: 2.64 %w/w; B4: 12.95 %w/w), tend to form macroscopic flakes within few minutes after being suspended in aqueous medium. Besides knowing the amount of Gd present in our materials, it is likewise important to quantitatively evaluate the degree of effective coverage of SPIONS due to the polyphenolic network. This information is pivotal to understand the way Gd ions could be possibly loaded in our materials. Such quantity has been measured via thermogravimetric analyses. Concerning the synthetic route A, sample A1 suffered a weight loss of 19.5 %, while sample A2 had a weight reduction of 10.5 % (net of initial water loss). It is important to notice that the amount of initial water contained in the two samples is quite similar (7.5 % for A1 vs 8.1 % for A2). Furthermore, after the degradation of the organic component a plateau is reached. Therefore, there is no evidence for the formation of a condensed hydroxylated Gd phase, such as  $Gd(OH)_3$ . Indeed, its presence could have altered either the initial hydration level or given rise to further weight loss above 430°C [24]. In addition, their nature appears quite similar as evidenced by the same final temperature for organic degradation (430°C). Hence, further investigations are needed to unravel the nature of condensed Gd species potentially present in An samples. Compared to them, sample B1 had a weight reduction of 13.6 % (net of initial water loss). Despite the difference in terms of organic content, what emerges about the final degradation temperature is crucial. For sample B1, in which TA molecules are PEGylated and wrapped around SPIONs by entanglement effect, degradation process terminates close to 380 ° C, quite lower than for An. This evidence is the first step to understand the nature of the coating (stronger in the An series with respect to Bn) generated around

the magnetic nanoparticles. Once the amount of organic layer coating and the amount of Gd carried by each sample have been determined, the influence on water relaxation time  $T_1$  and  $T_2$  of the samples suspended in physiological buffer, was measured. All the samples were suspended in a 20 mM MOPS (3-(*N*-morpholino) propane sulfonic acid) buffer solution at physiological pH (7.4), with a concentration of 30  $\mu\text{g/ml}$ . At this point, the first drawback with the samples has emerged. As previously stated, samples B3 and B4 are not stable in suspension. Indeed, after 30 min from the redispersion, both samples display aggregates visible by naked eye, making impossible the relaxivity measurements for these samples. Concerning samples A1, A2, B1, and B2, they were shelf stable up to several weeks at the highest concentrations. Therefore, they were diluted according to the proportions previously reported, namely 0.8:1, 0.5:1, 0.3:1 and 0.1:1, with respect to the mother solutions. In this way, it was possible to measure the relaxation times with different concentrations. The relaxivity parameters  $r_1$  and  $r_2$ , namely the slope of the lines interpolating the data in the graphs  $1/T_1$  or  $1/T_2$  vs concentration, were obtained. Samples A1 and A2 show two distinct behaviors in relaxivity parameters. Indeed, their influence on  $T_2$  is much larger than on  $T_1$ , while for a  $\text{Gd}^{3+}$  salt these two values are generally quite close to each other [63].  $r_1$  and  $r_2$  values for either A1 or A2 differ by almost two orders of magnitude, thus resembling the behavior of commercially available coated SPIONs [64]. In fact, such systems are characterized by a strong  $T_2$  effect, due to the magnetic field inhomogeneities generated by superparamagnetic particles. This could drive the conclusion that the form in which Gd is present in samples A1 and A2 is not useful to

influence the water relaxivities, i.e. as isolated  $Gd^{3+}$  ions, but in some other aggregate form. Their formation may be ascribed to the synthetic procedure A, in which high temperature and basic environment were employed, namely the same conditions in which metal oxide nanoparticles are commonly prepared. Nevertheless, this event has been observed for sample A1 only, in which Gd is added prior to the reticulation step. On the other hand, the lower amount of Gd in sample A2 with respect to A1 might reveal an additional phenomenon standing behind its poor performances, as clarified from FT-IR analysis. FT-IR spectra of A1 and A2 (Figure 35) display a strong reduction of phenolic hydroxyls peak ( $\delta_{ph(OH)}$  signal at  $\sim 1200\text{ cm}^{-1}$ ), with respect to TA [25].

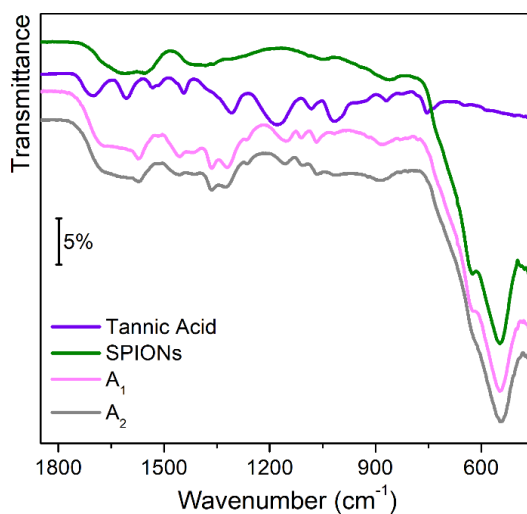


Figure 35. Normalized ATR-IR spectra in the 1850-450  $\text{cm}^{-1}$  range for samples A<sub>1</sub> (pink curve) and A<sub>2</sub> (grey curve) compared to their precursors, namely SPIONs (green curve) and TA (violet curve). Spectra are shifted for a better comparison.

This confirms that the crosslinking process, mediated by formaldehyde, occurs via water elimination and the consequent formation of  $-\text{CH}_2-$

bonds, between phenyl units [26]. However, crosslinking could not explain completely the Ph-OH elimination process. Indeed, TA catechol units may also be converted into cyclic acetals via acetalization process in the presence of formaldehyde at high temperature, thus enhancing the hydroxyls derivatization of TA phenolic units [27]. The large occurrence of these phenomena could contribute to the depletion of anchoring points for  $Gd^{3+}$  ions, thus limiting its effect on  $r_1$  relaxivity, in the case of sample A2. Concerning the other synthetic procedure, relaxivities measurements for sample B1 (having no gadolinium loaded) seem to confirm the hypothesis that only magnetic nanoparticles are influencing relaxivity. Indeed,  $r_1$  and  $r_2$  parameters resemble the ones of pure SPIONs, similarly to A1 and A2. Sample B2, instead, reveals hints of Gd presence in isolated form. Even with a minimum loading (0.66 %w/w), an increase of almost 50 % for  $r_1$  value, with respect to sample B1, has been recorded. However, in the subsequent T2 measurements,  $r_2$  value was reduced with respect to all other samples, due to a total loss of data linearity. This appears to be the clue of a SPION aggregation process that occurs as a consequence of prolonged exposure of the sample to magnetic fields. When inter-particle magnetic forces increase their intensities, they push together sample particles that, in a situation of closer vicinity, might interact. This is confirmed by the post-MRI observation of aggregates inside the vials containing the most concentrated solutions, which appeared no longer stable in suspension. Such aggregates reduce the water-particles surface area, available for waterhydrogen magnetic interactions, and can be responsible of reduced relaxivities. A validation of this hypothesis can be drawn analyzing the signals detected with ATR-MIR spectroscopy for Bn samples.

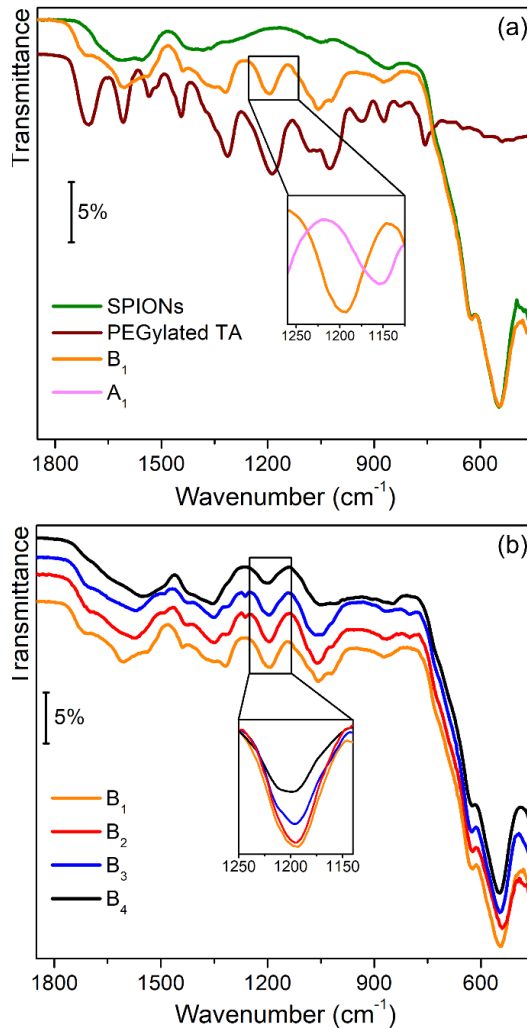
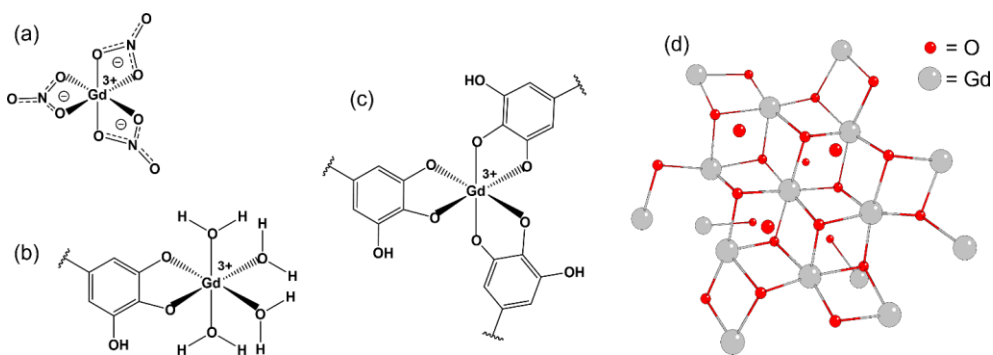


Figure 36. Part a: normalized ATR-IR spectra in the 1850-450 cm<sup>-1</sup> range for sample B<sub>1</sub> (orange curve) compared to its precursors, namely SPIONs (green curve) and PEGylated TA (brown curve); inset highlights the spectral region for δ<sub>ph</sub>(O-H) vibrations for phenolic species relative to samples A<sub>1</sub> (pink curve) and B<sub>1</sub> (orange curve). Part b: ATR-IR spectra in the 1850-450 cm<sup>-1</sup> range for samples B<sub>1</sub> (orange curve), B<sub>2</sub> (red curve), B<sub>3</sub> (blue curve) and B<sub>4</sub> (black curve); inset highlights the spectral region for δ<sub>ph</sub>(O-H) vibrations for phenolic species for the B<sub>n</sub> series. Spectra in the main figures are vertically shifted for a better comparison, spectra in the insets are not shifted.

In the inset of Figure 36 it is possible to observe the difference in δ<sub>ph</sub>(OH) intensity between samples A<sub>1</sub> and sample B<sub>1</sub>. While in the first

one the phenolic hydroxyls were almost completely used for the sake of TA reticulation, in the second one the synthetic procedure leaves them almost unaltered and able to serve as anchoring points for  $Gd^{3+}$  ions. Furthermore, in Fig. 36b,  $\delta_{ph(OH)}$  signal decreases noticeably with the increase of gadolinium loading (see inset). For sample B2, a Gd local environment similar to the one represented in Scheme 8b, have been hypothesized.



Scheme 8. Schematic representation of the hypothesized Gd local environment in the case of  $Gd(NO_3)_3$  (a);  $B_n$  in low coordination (b);  $B_n$  in high coordination (c);  $Gd_2O_3$  possibly describing the local environment of Gd for samples  $A_n$  (d).

In such configuration, the coordination sphere of the metal is only partially saturated by the phenolate bidentate ions. However, the loaded metal is pretty oxophilic and characterized by a large coordination sphere. Hence, in the presence of a high Gd loading and/or high concentrations of phenolic groups, various coated particles endowed with polyphenolic arms will start to interact with each other, under the templating effect of  $Gd^{3+}$  ion (Scheme 8c). Once a critical dimensions are reached, they will cause a precipitation phenomenon. This might explain



the behavior observed with B3 and B4 samples. A similar situation in the case of sample B2, could appear after the material has been subjected to a strong magnetic field, as during relaxivity measurements. The magnetic force could have pushed together B2 particles to such an extent able to cause particles interaction and precipitation. To confirm this hypothesis, a careful investigation of Gd local coordination environment and its prevalent oxidation state by means of XPS measurements, is needed (Figure 37).

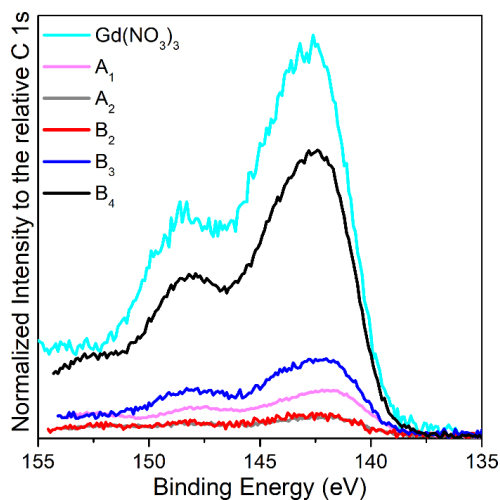


Figure 37. Gd 4d XPS spectra for  $\text{Gd}(\text{NO}_3)_3$  (light blue), and for samples A<sub>1</sub> (pink), A<sub>2</sub> (grey), B<sub>2</sub> (red), B<sub>3</sub> (blue), B<sub>4</sub> (black). All the curves have been aligned to C 1s signal at 284.8 eV and their intensity was normalized to according to the same peak (Figure S17a).

Indeed, it is known that TA, among others, has also been used as reducing agent in the sustainable synthesis of different metal nanoparticles [28]. Such activity, potentially leading to a reduction of Gd species and a total loss of its relaxivity, should be avoided. Since isolated  $\text{Gd}^{3+}$  ions are among the most active species for imaging contrast applications, it is of pivotal importance excluding this side-reaction. The likely formation of

a Gd precipitate, possibly in the form of  $\text{Gd}_2\text{O}_3$ , have been previously hypothesized in the case of An samples. Peaks position, relative to Gd  $4d_{5/2}$  binding energy at 142 eV and to Gd  $4d_{3/2}$  at 148 eV, confirm the presence of oxidic clusters [29]. Indeed, the binding energy associated to the same emission from a metallic zerovalent Gd species is almost 2 eV lower [30], thus excluding any reducing effect of TA. Contemporarily, it is also possible to exclude the presence of  $\text{Gd}(\text{OH})_3$ , since its  $4d_{5/2}$  and  $4d_{3/2}$  XPS signals are at 141.5 and 147.5 eV respectively [31]. However, the formation of oxidic precipitates is the consequence of a two-step process, potentially taking place during the synthetic route A. Such process starts with the formation of a  $\text{Gd}(\text{OH})_3$  precursor in the presence of a basic environment and high temperature [24], followed by a dehydration step at  $T > \text{r.t.}$  The last step reduces Gd coordination number, changing from 9 (in the case of hydroxide) to 6 (in the case of the oxide) [32], thus leaving only  $\text{Gd}_2\text{O}_3$  as final product. Comparing this datum with the value for Gd  $4d_{5/2}$  binding energy of  $\text{Gd}(\text{NO}_3)_3$  ( $\sim 143$  eV) [33], it is possible to conclude that the surrounding environment of Gd atoms is pretty similar. In fact, in gadolinium oxide the metal atoms may interact with up to six oxygen atoms in the first coordination shell (Scheme 8d) [33-35]. Similarly,  $\text{Gd}^{3+}$  ions in the nitrate salt are coordinated by six oxygen atoms in the first shell (Scheme 8a) [80]. Samples B2, B3 and B4, for which a situation as the ones in Scheme 8b-c have been pictured, show a Gd  $4d_{5/2}$  band pretty similar to all the other samples. On one hand, the presence of gadolinium species is confirmed to be associated only to the (III) oxidation state. This should influence the relaxivity of the system, similarly to  $\text{Gd}^{3+}$  isolated ions (as in the case of B2). On the other hand, with the techniques employed so far, it is not

possible to clearly distinguish the diverse Gd local environments, since in all the samples Gd is always surrounded by six oxygen atoms.

### *6.3 Experimental*

#### *6.3.1 SPIONs synthesis*

The synthesis of SPIONs is based on an adjusted literature procedure [5]3, here shortly reported. 1.3 g of  $\text{FeCl}_3 \cdot 6\text{H}_2\text{O}$  and 0.25 g of trisodium citrate were added into a glass autoclave liner with 35 ml of a 9:1 ethylene glycol:ethanol solution, and dissolved using an ultrasound bath. Afterwards, 1.7 g of sodium acetate was added to the solution, and the glass liner inserted in a rotating Parr reactor head. Once the reactor is closed, oxygen was removed by means of 5 washing cycles with  $\text{N}_2$  gas (15 bar each), also checking for any leak. The chamber was filled with 5 bar of nitrogen and let react at  $200^\circ\text{C}$  for 15 h under mechanical stirring. After that, the reaction was allowed to cool at room temperature and the solid was separated by centrifugation at 5000 rpm for 20 min. The obtained sample was washed 3 times with ethanol and 3 more times with 0.02 M NaCl solution, followed by centrifugation at 5000 rpm for 20 min after each washing. The sample was resuspended in ethanol and dried in an oven at  $110^\circ\text{C}$ .

#### *6.3.2 An-series samples synthesis*

The series of An samples was prepared through a modified literature procedure [36], and it's pictured in Scheme 6. In detail, for sample A1, 50 mg of SPIONs were inserted in a Schlenk tube with 6.2 ml of deionized water and 1.3 ml of ethanol and resuspended through ultrasound irradiation. Then, 70  $\mu$ l of ammonia solution were added and the suspension magnetically stirred. Afterwards, 33 mg of tannic acid were added. After 90 min, 65  $\mu$ l of formaldehyde solution were added and the suspension was kept under stirring at room temperature (r.t.) for 4 h. Subsequently, 16.5 mg of  $\text{Gd}(\text{NO}_3)_3 \cdot 6\text{H}_2\text{O}$  were dissolved in 350  $\mu$ l of deionized water, added to the suspension and kept under stirring at r.t. for 24 h. After that, the temperature was risen to 130°C for 15 h. The reaction was then allowed to cool to r.t. and the solid was separated by centrifugation at 4000 rpm for 40 min. The obtained sample was washed 6 times with deionized water, followed by centrifugation at 4000 rpm for 40 min after each washing. The obtained sample was dried in high vacuum at 60°C for 8 h. For sample A2, the same preparation procedure of A1 was employed, skipping the  $\text{Gd}^{3+}$  ions addition that was performed as follows. The synthesized powder was resuspended in 8 ml of deionized water and 16.5 mg of  $\text{Gd}(\text{NO}_3)_3 \cdot 6\text{H}_2\text{O}$  were added; the suspension was kept at r.t. under stirring for 5 h. The solid was separated by centrifugation at 4000 rpm for 40 min. After supernatant removal, it was washed 3 times with deionized water, followed by centrifugation at 4000 rpm for 40 min after each washing. The obtained sample was dried in high vacuum at 60°C for 8 h. Summarizing, in sample A1, Gd precursor was added to the material prior to the reticulation step, while for sample A2 its addition has been made after the TA crosslinking step.

### 6.3.3 Bn-series samples synthesis

The synthesis procedure for the series of Bn samples has been adapted from the literature [37], and it is pictured in Scheme 7. For sample B1, 50  $\mu\text{l}$  of PEG200 and 800 mg of  $\text{PPh}_3$  were dissolved in 80 ml of acetonitrile and kept under vigorous stirring over an ice bath. Separately, 1 g of TA and 100 mg of SPIONs were dissolved in 20 ml of acetonitrile and irradiated with ultrasound until complete suspension of the magnetic nanoparticles. Then, the two previously prepared solutions were joined and kept at  $0^\circ\text{C}$  for 10 min. Afterwards, 590  $\mu\text{l}$  of DIAD (Diisopropyl azodicarboxylate) were added dropwise. The reaction ran for 60 min at  $0^\circ\text{C}$ , then was removed from the ice bath and kept at r.t. for 90 min. Finally, it was brought to  $60^\circ\text{C}$  for additional 90 min. The reaction slurry was transferred inside a centrifuge tube and magnetically decanted. After supernatant removal, three washing cycles with acetonitrile followed by magnetic decantation were performed. The obtained sample was dried at r.t. overnight, followed by 2 h in high vacuum at r.t. Samples B2, B3 and B4, were prepared as follows: 10 mg of B1 were suspended in 4.2 ml of MOPS buffer solution (20 mM, pH = 7.4) inside a 10 ml reaction balloon. Then, aqueous solutions of  $\text{Gd}(\text{NO}_3)_3 \cdot 6\text{H}_2\text{O}$  were added to the suspensions (0.444  $\mu\text{molGd}$  in the case of B2, 2.22  $\mu\text{molGd}$  in the case of B3, 22.2  $\mu\text{molGd}$  in the case of B4) and were kept under vigorous magnetic stirring for 30 min at r.t. The solutions were then transferred inside a dialysis membrane and dialyzed against 210 ml MOPS buffer solution. In the case of Bn samples, the use of dialysis workup in place of centrifugation is necessary due to the higher fragility of the entangled TA network with respect to the covalently bound one in the An series. The

suspension containing the samples were removed from the membrane and stored in sealed vials. Summarizing, sample B1 was prepared by means of TA PEGylation in presence of SPIONs. Afterwards, portions of B1 were suspended in aqueous solutions containing different amount of  $Gd^{3+}$  precursor, obtaining samples B2, B3, and B4, respectively.

#### *6.3.4 Attenuated Total Reflectance-Mid Infrared (ATR-MIR) spectroscopy*

FT-IR spectra were collected by means of a PerkinElmer Spectrum Two instrument equipped with an atmospheric UATR Two accessory and a DTGS detector. Each measurement was the average of 8 scans with  $4\text{ cm}^{-1}$  resolution, collected in the  $4000\text{--}400\text{ cm}^{-1}$  range.

#### *6.3.5 X-ray Photoelectron Spectroscopy (XPS)*

XPS spectra were acquired with a PHI 1257 system, with a working pressure of  $10^{-9}$  Torr, using a non-monochromatized Mg  $K\alpha$  X-ray source and a hemispherical analyzer. C 1s, O 1s, Gd 4d and Fe 2p spectral regions were collected with a constant pass energy of 23 eV, corresponding to a spectral resolution of 0.75 eV. The obtained spectra were aligned exploiting the C 1s peak at 284.8 eV in binding energy (BE - not showed here). Background compensation was performed by means of a Shirley function.

### *6.3.6 Scanning Electron Microscopy (SEM)*

SEM images were acquired using a FESEM ZEISS Gemini500 instrument. Images were collected with either transmitted or backscattered electrons, operating with an HT (accelerating voltage) of 20 kV. The samples were dispersed via sonication and a drop of the suspension was deposited on TEM copper grids (200 mesh) covered with an amorphous carbon film.

### *6.3.7 Thermogravimetric Analyses (TGA)*

TGA was performed with a Linseis L-81 instrument. The measurements were performed in air with a temperature ramp of 10°C/min from r.t. to 750°C.

### *6.3.8 Dynamic Light Scattering (DLS)*

Particle size measurements were performed by means of a Nanosight NS300 instrument using a blue laser ( $\lambda = 488 \text{ nm}$ ). The samples (0.1 ppm in milliQ water) were injected in the instrument cell with a syringe pump using a flow rate of 50  $\mu\text{l/s}$ . Five acquisitions of 60 s are made, each one collecting 25 frames/s. The particle size values were obtained by merging and averaging all the data together.

### *6.3.9 Magnetic Resonance Imaging (MRI) analyses*

Prior to MRI measurement, the samples were prepared starting from a mother solution of 30  $\mu\text{g/ml}$  in MOPS buffer (20 mM, pH = 7.4). T1 and T2 were measured using the mother solution, 4 different dilutions (0.8:1, 0.5:1, 0.3:1, 0.1:1) and the pure buffer. MRI was performed with a preclinical M3 Aspect Imaging scanner with about 1 T magnetic field (45 MHz). The radiofrequency coil was a solenoid with 3.5 cm inner diameter and 8 cm length, which allowed the insertion of up to six vials with different contrast agent concentration at the same time. T1 relaxation time was acquired from axial Spin Echo images with FOV of 32x32 mm<sup>2</sup>, 1 mm in-plane resolution and 8 mm slice thickness, TE = 4.1 ms and 19 different TR values in the 50–10000 ms range for a total acquisition time of 25 min. T1 was extracted by the exponential recovery of each image voxel intensity, and the values from each vial voxels averaged. The absence of a multi-echo Spin Echo sequence prevented T2 relaxation determination from images. The use of a Fast Spin Echo sequence with echo train length equal to 192 and all gradients disabled, instead, allowed to effectively perform a whole sample CPMG acquisition. In this case, multiple echoes from a single vial with TE = 4.4 ms and a total measurement time of 2 min were acquired, finally extracting T2 from the echoes amplitude exponential decay.

### *6.3.10 Inductively Coupled Plasma-Mass Spectrometry (ICP-MS)*



ICP-MS analyses were performed with a mass spectrometer Agilent Technologies 7500a equipped with an ASX500 CETAC autosampler. During sequences, a rinsing with HNO<sub>3</sub> 2% solution was carried out to eliminate any memory effect. Mass spectrometer is installed inside ISO-6 clean room to reduce risk of environmental contamination. The procedure for samples solubilization is described in the following part: 4 mg of each sample were weighed in previously conditioned PFA vials. Dissolution of samples was carried out with 1 ml of HNO<sub>3</sub> and 100 µl of HF, heat treated at 120°C for 60 min. Subsequently, 8 ml of H<sub>2</sub>O were added into PFA vials at 100°C for additional 60 min. Samples were centrifuged at 4000 rpm for 20 min to remove the supernatant. A second etching was performed with same procedure using 1 ml HNO<sub>3</sub> and 5 ml H<sub>2</sub>O in two different steps of 60 min each. The goal of second etching is related to recouping eventual traces of non-solubilized samples inside the vials. The obtained solutions were united and then diluted 1:50 to performed ICP-MS characterization.

#### *6.4 Conclusions*

In this work, two methodologies capable to stably suspend SPIONs in physiological environment, alternative to the commercially available ones, were optimized. The prepared materials can be considered a preliminary step for the preparation of new hybrid systems for MRI applications, by coupling the coating/entanglement effect of bio-compatible polymers (responsible for the solubility) with chemical species able to bear Gd<sup>3+</sup> ions, thus conferring dual modal MRI

responsivity. Both synthetic routes were able to provide a set of samples stable in physiological conditions, capable of carrying Gd species to a certain extent. However, the sample that is most positively affected by the presence of Gd<sup>3+</sup> ions (B2), is also the one displaying the lowest operational stability. Contrarywise, the other stable samples do not show appreciable deviation from pure SPIONs relaxivity behavior, despite some of them are loaded with a non-negligible amount of Gd (A1). Nevertheless, they possess elevated stability also after being exposed to intense magnetic fields. The right balance between T1-T2 tunability and stability is far to be achieved at the moment. However, a way for further development of new and alternative routes to stably suspend magnetic nanoparticles to be employed as potential dual-mode T1-T2 contrast agents has been opened. With the right experimental adjustments, we strongly believe that exploitation of synergic SPIONs and Gd relaxivities effects, for tailored MRI applications, will be available soon.

## References

1. Xiao Y. D., Paudel R., Liu J., Ma C., Zhang Z. S., Zhou S. K., **2016**, *Inter. J. of Molec., Med.*, 38, 1319-1326.
2. Young I. R., Clarke G. J., Bailes D. R., Pennock J. M., Doyle F. H., Bydder G. M., **1981**, *J. Comput. Tomogr.*, 5, 543-547.
3. Gerald C. F. G. C., Laurent S., **2009**, *Contrast. Media Mol. Imaging*, 4, 1-23.
4. Shokrollahi H., **2013**, *Mater Sci Eng C*, 33, 4485-4497.
5. Yurt A., Kazanci N., **2008**, *J. Mol. Struct.*, 892, 392-397.
6. Laurent S., Forge D., Port M., Roch A., Robic , Elst L.V., Muller R.N., **2008**, *Chem. Rev.*, 108, 2064–2110.
7. Lee N., Yoo D., Ling D., Cho M.H., Hyeon T., **2015**, *Chem. Rev.*, 115, 10637–10689.
8. Lim E.K., Kim T., Paik S., Haam S., Huh Y.M., Lee K., **2015**, *Chem. Rev.*, 115, 327–394.
9. Antonelli A., Magnani M., **2022**, *J. Magn. Magn. Mater.*, 54, 168520.
10. Khan M.I., Hossain M.I., Hossain M.K., Rubel M.H.K., Hossain K.M., Mahfuz A.M.U. B., Anik M.I., **2022**, *ACS Appl. Bio Mater.*, 5, 971–1012.
11. Ludwig F., Wawrzik T., Yoshida T., Gehrke N., Briel A., Eberbeck D., Schilling M., **2012**, *IEEE Trans. Magn.*, 48, 3780–3783.
12. Frericks B.B., Wacker F., Loddenkemper C., Valdeig S., Hotz B., Wolf K.J., Misselwitz B., Kuhl A., Hoffmann J.C., **2009**, *Invest. Radiol.*, 44, 23–30.
13. Liu D., Wu W., Ling J., Wen S., Gu N., Zhang X., **2011**, *Adv. Funct. Mater.*, 21, 1498–1504.
14. Gupta A.K., Wells S., **2004**, *IEEE Trans. Nanobiosci.*, 3, 66–73.
15. Suarez-Garcia S., Solorzano R., Novio F., Alibes R., Busque F., Ruiz-Molina D., **2021**, *Chem. Rev.*, 432, 213716.

16. Hermann P., Kotek J., Kubíček V., Lukes I., **2008**, *Dalton Trans.*, 3027-3047.
17. Ejima H., Richardson J.J., Liang K., Best J.P., van Koeuverden M.P., Such G.K., Cui J., Caruso F., **2013**, *Science*, 341, 154–157.
18. Guo J., Ping Y., Ejima H., Alt K., Meissner M., Richardson J.J., Yan Y., Peter K., vonElverfeldt D., Hagemeyer C.E., Caruso F., **2014**, *Angew. Chem.-Int. Edit.*, 53, 5546–5551.
19. Qian Y., Chen S., He C., Ye C., Zhao W., Sun S., Xie Y.i., Zhao C., **2020**, *ACS Omega*, 5, 6566–6575.
20. Jia X., Wu J., Lu K.e., Li Y., Qiao X., Kaelin J., Lu, S., Cheng Y., Wu X., Qin W., **2019**, *J. Mater. Chem. A*, 7, 14302–14308.
21. Chen T., Huang R., Liang J., Zhou B.o., Guo X.-L., Shen X.C, Jiang B.P., **2020**, *Chem. Eur. J.*, 26, 15159–15169.
22. Yang B.o., Zhou S., Zeng J., Zhang L., Zhang R., Liang K., Xie L., Shao B., Song S., Huang G., Zhao D., Chen P.u., Kong B., **2020**, *Nano Res.*, 13, 1013–1019.
23. Mitsunobu O., Yamada M., **1967**, *Bull. Chem. Soc. Jpn.*, 40, 2380–2382.
24. Kang J.G., Min B. K., Sohn Y., **2015**, *Ceram. Int.*, 41, 1243–1248.
25. Ranošek-Soliwoda K., Tomaszewska E., Socha E., Krzyczmonik P., Ignaczak A., Orłowski P., Krzyczowska M., Celichowski G., Grobelny J., **2017**, *J. Nanopart. Res.*, 19, 273.
26. Qin J., Liang G., Feng B., Wang G., Wu N.a., Deng Y., Elzatahry A.A., Alghamdi A., Zhao Y., Wei J., **2021**, *Chin. Chem. Lett.*, 32, 842–848.
27. Leibig D., Lange A. K., Birke A., Frey H., **2017**, *Macromol. Chem. Phys.*, 218, 1600553.
28. Veisi H., Pirhayati M., Kakanejadifard A., Mohammadi P., Abdi M.R., Gholami J., Hemmati S., **2018**, *Chemistry Select.*, 3, 1820–1826.
29. Dolo J.J., Swart H.C., Coetsee E., Terblans J.J., Ntwaeaborwa O.M., Dejene B.F., **2010**, *Hyperfine Interact.*, 197, 129–134.

30. Saha A., Mohanta S.C., Deka K., Deb P., Devi P.S., **2017**, *ACS Appl. Mater. Interfaces*, 9, 4126–4141.
31. Ullah N., Imran M., Liang K., Yuan C. Z., Zeb A., Jiang N., Qazi U.Y., Sahar S., Xu A. W., **2017**, *Nanoscale*, 9, 13800–13807.
32. de Almeida M.S., dos Santos M.A.B., Goncalves R.D., Santos M.R.D., Marques A.P. D., Longo E., La Porta F.D., Pinatti I.M., Silva M.D.P., Godinho M.J., **2016**, *Mater. Res.*, 19, 1155–1161.
33. Raiser D., Deville J.P., **1991**, *J. Electron Spectrosc. Relat. Phenom.*, 57, 91–97.
34. Jadhav A.P., Oh J.H., Park S.W., Choi H., Moon B.K., Choi B.C., Jang K., Jeong J. H., Yi S.S., Kim J.H., **2016**, *Curr. Appl. Phys.*, 16, 1374–1381.
35. Liu B., Zhang W., Yang F., Feng H., Yang X., **2011**, *J. Phys. Chem. C*, 115, 15875–15884.
36. Qin J., Liang G., Feng B., Wang G., Wu N.a., Deng Y., Elzatahry A.A., Alghamdi A., Zhao Y., Wei J., **2021**, *Chin. Chem. Lett.*, 32, 842–848.
37. Chen C., Geng X. W., Pan Y. H., Ma Y. N., Ma Y. X., Gao S. Z., Huang X. J., **2020**, *RSC Adv.*, 10, 1724–1732.

## **7. Selective N-methylation and reduction of variously substituted nitroarenes using catalytic precursors of Ruthenium(II) half-sandwich complexes with dioxime ligands**

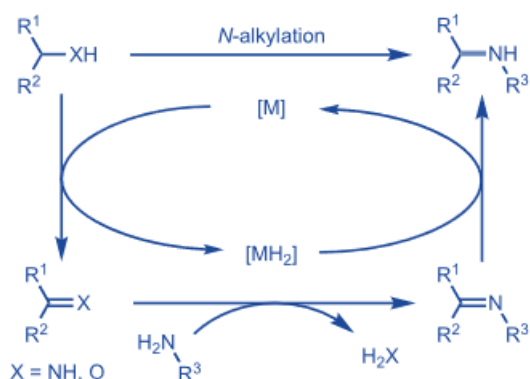
### *7.1 Introduction*

N-Methyl anilines are utilized as components or enhancers in dyes, polymers, explosives, herbicides, and fuels [1]. Typically derived from the methylation of the parent aniline, methylation of NH groups stands as a critical late-stage functionalization method for a variety of fine chemicals and pharmaceuticals [2]. To circumvent the use of highly hazardous methylating agents (e.g. MeI, Me<sub>2</sub>SO<sub>4</sub>, methyl triflate), a convenient, atom-economic approach for synthesizing N-methyl anilines (amines) involves methanol in a borrowing hydrogen strategy (Scheme 9) [3].

Borrowing hydrogen chemistry, also referred to as hydrogen autotransfer, operates within this framework, albeit with a significant distinction. In a borrowing hydrogen reaction, a pair of transfer hydrogenations is integrated with an intermediate reaction involving the reactive intermediate generated in situ. The process commences with a transition-metal-mediated dehydrogenation of an alcohol or amine, yielding a reactive carbonyl (or imine) intermediate. This unsaturated species is capable of undergoing various subsequent transformations,

including condensation with an amine. The resulting species can then be reduced by  $[MH_2]$ , which is produced in the initial dehydrogenation step, thereby regenerating the active catalyst and releasing the reaction product (in this instance, an *N*-alkylated amine), thereby completing the catalytic cycle. The borrowing hydrogen approach typically exhibits selectivity towards monoalkylation, offering a complementary aspect to numerous traditional alkylation methodologies [4].

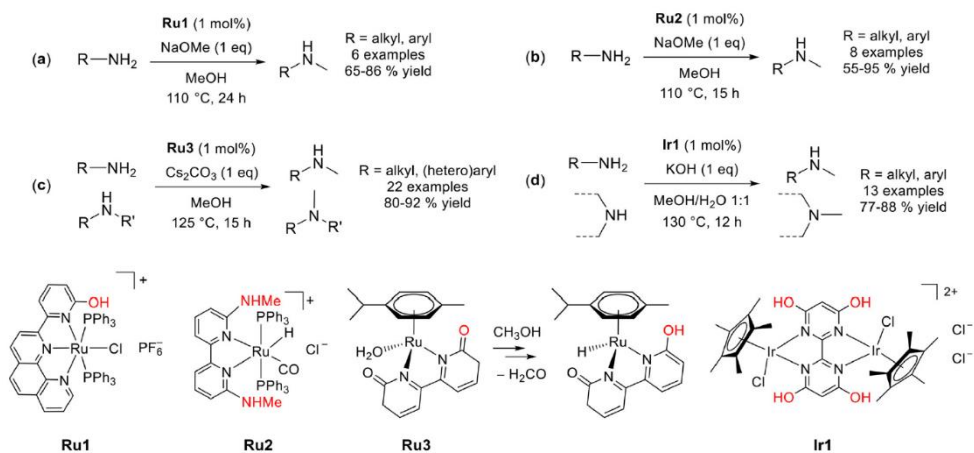
In this reaction, methanol is involved in a dehydrogenation/condensation/hydrogenation sequence, yielding water as the sole co-product.



Scheme 9. General transition-metal-catalyzed borrowing hydrogen reaction pathway

However, the dehydrogenation of methanol ( $\Delta H^\circ = +130.5 \text{ kJ mol}^{-1}$ ) poses a greater challenge compared to commonly used alkanols such as ethanol ( $\Delta H^\circ = +85.9 \text{ kJ mol}^{-1}$ ), isopropanol ( $\Delta H^\circ = +70.0 \text{ kJ mol}^{-1}$ ), or benzylic alcohol ( $\Delta H^\circ = +73.7 \text{ kJ mol}^{-1}$ ).<sup>4</sup> Ruthenium complexes are renowned for catalyzing  $H_2$ -autotransfer processes, including *N*-alkylation of amines with alcohols. Various Ru-based systems have been reported for the

catalytic N-methylation of alkyl or arylamines with methanol [5], with a recent focus on ruthenium(II)  $\eta^6$ -arene precursors [6]. Introducing ancillary (non-coordinating) OH or NHMe groups on polydentate *N*-donor ligands has enhanced catalytic performance in some cases (Ru1–Ru3 in Scheme). Cooperative effects from peripheral hydroxyl groups were also observed in a pentamethylcyclopentadienyl (Cp\*) iridium(III) catalyst (Ir1 in Scheme 10) [7].

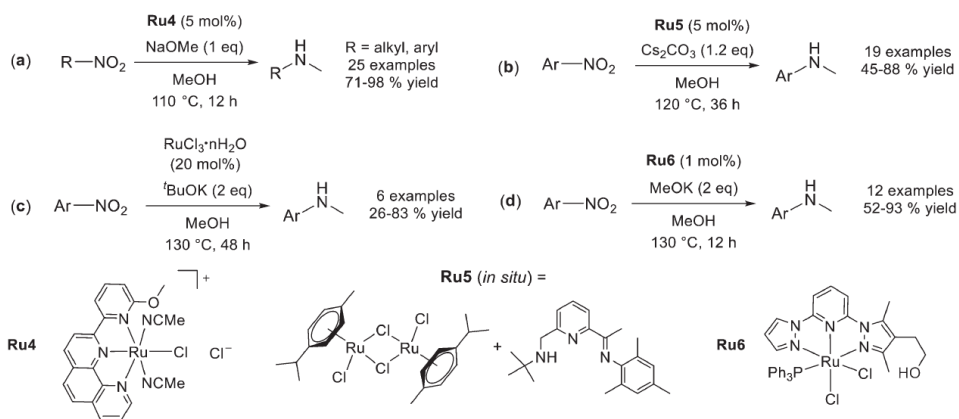


Scheme 10. Literature catalytic systems for the N-methylation of amines (anilines), taking advantage of cooperative effects from ancillary hydroxy or amino functions (in red) on the catalyst precursors Ru1 (a, 2018), Ru2 (b, 2018), Ru3 (c, 2021) or Ir1 (d, 2020). Year of publication is indicated.

The hydrogenation of readily available nitroarenes is commonly used to access the respective aniline, including some industrially relevant cases. Consequently, an efficient one-pot process for the preparation of *N*-methyl anilines from nitroarenes using methanol simultaneously as the solvent, C1 synthon, and H<sub>2</sub> donor is highly appealing (Scheme 9). Ruthenium complexes have shown significant success as homogeneous catalytic precursors for the transfer hydrogenation of various organic



substrates [8]. However, to our knowledge, only four Ru-based catalytic systems have been evaluated for the one-pot reductive N-methylation of nitroarenes (Scheme 11) [9]. These protocols operate under solvothermal conditions (110–130°C) for 12–48h and necessitate a stoichiometric amount of a potent Brønsted base, which in principle, serves as a cocatalyst. Such base loading and temperature requirements are frequently encountered in the catalytic N-methylation of amines/anilines with methanol [10].



Scheme 11. Catalytic systems for the tandem reductive N-methylation of nitro compounds employing Ru-based catalytic precursors Ru4 (a, 2017), Ru5 (b, 2019), RuCl<sub>3</sub> hydrate (c, 2021) or Ru6 functionalized with a peripheral hydroxyl group (d, 2022). Year of publication is indicated.

The catalytic precursors Ru4–Ru6 feature sophisticated  $\kappa^3\text{N}$  pincer-type ligands. Alternatively, commercial RuCl<sub>3</sub>·*n*H<sub>2</sub>O was employed at very high loading. Interestingly, a remote hydroxyl group of the bis-pyrazolyl-pyridine ligand in Ru6 substantially improved catalytic efficiency by engaging in crucial hydrogen bonding interactions throughout the DFT-optimized catalytic cycle. In the course of our ongoing interest in the development of ruthenium(II)  $\eta^6$ -arene complexes employing simple, commercially-available ligands within the realm of metal–ligand

bifunctional catalysis, we turned our attention to dioxime ligands, which combine a chelating *N,N* unit with ancillary (potentially non-coordinating) OH groups. Transition metal complexes of dioximes exhibit a rich coordination chemistry and those of cobalt(III) have been extensively examined as models of cobalamin or electrocatalysts for H<sub>2</sub> production [11]. Dimethylglyoxime and nioxime have historically served as gravimetric reagents for nickel analysis, albeit investigations on the catalytic activity of ruthenium dioxime complexes have been largely overlooked until now [12]. In this context, ruthenium(II) arene complexes featuring bidentate amino-, pyridyl- and phosphane-(mono)oxime ligands have been tested for the transfer hydrogenation of ketones and nitroarenes, dehydrogenation of hydrazine, and alkyne hydration (Fig. 37a).<sup>18</sup> Surprisingly, the NOH/NO<sup>-</sup> moiety played a passive role in proposed mechanisms, even when the oxime complexes exhibited superior catalytic activity compared to structurally similar compounds [13]. Furthermore, relatively few dioxime complexes of other 4d and 5d metals have been explored for their catalytic activity [14]. Among these, a notable case involves in situ formed Ir(III) Cp\* complexes with amino-substituted dioxime ligands, which have been reported as highly effective for formic acid dehydrogenation (Fig. 37b). Herein, we utilized commercially available dioximes to create a novel series of mononuclear ruthenium(II) compounds with different arene and halide co-ligands and counter ions (Fig. 37c). The complexes' catalytic activity in the tandem reduction/N-methylation of nitroarenes with methanol was investigated, revealing the dioxime ligand's critical role in the process's selectivity.

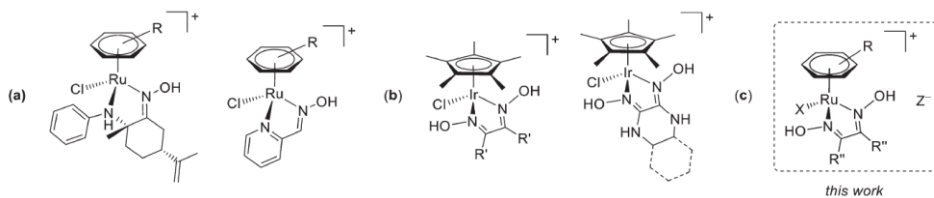
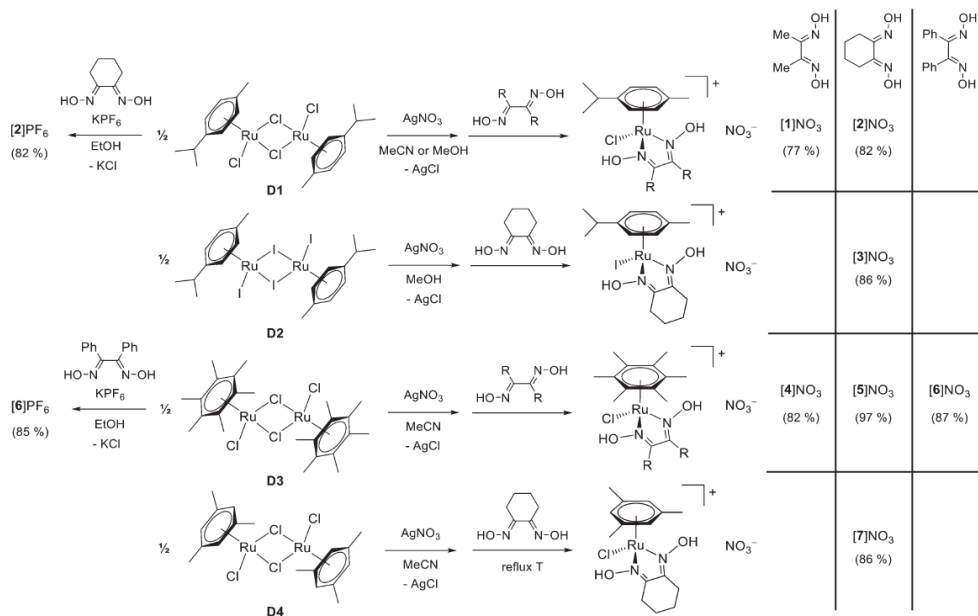


Figure 37. Previously-reported Ru(II) arene complexes with pyridyl-oxime or amino-oxime ligands (a) and Ir(III) Cp\* dioxime complexes ( $R' = \text{H, Me, Cl, NH}_2$ ) (b) investigated as catalytic precursors (Cl-salts). General structure of the ruthenium(II) dioxime compounds investigated in this work (c).

## 7.2 Synthesis of Ru compounds

Ruthenium arene dioxime complexes  $[\text{RuX}(\text{dioxime})(\eta^6\text{-arene})]^+$ ,  $[1-7]^+$ , were synthesized via a two-step procedure involving the cleavage of halido-bridged dimers  $[\text{RuX}_2(\eta^6\text{-arene})]_2$  with  $\text{AgNO}_3$  in MeCN or MeOH, followed by the addition of the selected dioxime at room temperature (or reflux for  $[\text{RuCl}_2(\eta^6\text{-1,3,5-C}_6\text{H}_3\text{Me}_3)]_2$ ; Scheme 12). These reactions were carried out under strict stoichiometric conditions: an excess of  $\text{AgNO}_3$  resulted in the production of by-products, while excess dioxime proved challenging to remove during the work-up process. Intriguingly, the interaction of the supposed  $[\text{RuX}(\text{MeCN})_2(\eta^6\text{-p-cymene})]^+$  intermediates with nioxime led to a variable (5–20%) release of p-cymene and the consequent formation of unidentified nioxime complexes [15]. The successful synthesis of  $[2-3]\text{NO}_3$  necessitated MeOH as a solvent for both reaction steps. The resulting compounds,  $[1-7]\text{NO}_3$ , were obtained as air-stable yellow/orange powders in yields ranging from 77–93%. Similarly, the one-pot reaction of  $[\text{RuCl}_2(\eta^6\text{-arene})]_2$  with  $\text{KPF}_6$  and nioxime in EtOH led to the isolation of  $[2]^+$  and  $[6]^+$  as  $\text{PF}_6^-$  salts in yields of 82–85%

(Scheme 12). These compounds were synthesized as an alternative to the nitrate salts.



Scheme 12. Preparation of ruthenium  $\eta^6$ -arene dioxime complexes [1–7]<sup>+</sup> from the corresponding halido-bridged dimers D1–D4. All reactions were carried out in stoichiometric conditions at room temperature, except where otherwise noted.

### 7.3 Reactivity of dioxime complexes in methanol

In essence,  $[\text{RuX}(\kappa_2\text{N}\{-\text{RC}\text{-NOH}\}_2)(\eta^6\text{-arene})]^+$  complexes feature two Brønsted-acidic groups (OH) and a halide ligand, potentially substitutable by a solvent molecule or the N-oxy group of another complex, leading to the formation of bimetallic oximato-bridged species. The network of acid/base and halide/solvent equilibria, appears to be considerably subdued in methanol. Predominantly, the undissociated cationic dioxime complex [1–7]<sup>+</sup> is observed in solution, indicated by a unique set of signals in the <sup>1</sup>H NMR spectra of [1–7]NO<sub>3</sub> and [2,6]PF<sub>6</sub>, the

absence of the diagnostic signal for the chloride ion in the  $^{35}\text{Cl}$  NMR spectra of  $[1,5,6]\text{NO}_3$  and  $[2]\text{PF}_6$ , and conductivity data of  $[2,4]\text{NO}_3$  aligning with that of a reference 1:1 electrolyte ( $\text{KNO}_3$ ). The identity of  $[3]^+$  in MeOH was further confirmed by ESI-MS (Fig. S42†). Subsequently, reactions of representative dioxime complexes ( $[2]\text{PF}_6$  and  $[3-4]\text{NO}_3$ ) in methanol with various Brønsted bases ( $\text{Et}_3\text{N}$ ,  $\text{NaHCO}_3$ ,  $\text{K}_2\text{CO}_3$ , or  $^t\text{BuOK}$ ) were investigated by  $^1\text{H}$  NMR. Complexes  $[2-4]^+$  can undergo single or double deprotonation, as evidenced by the progressive shielding of the  $^1\text{H}$  NMR resonances. The formation of the dioximato complex  $[3-2\text{H}]^-$  from  $[3]^+$  and  $^t\text{BuOK}$  (3.0 eq.) was also verified by ESI-MS. Species resulting from the dissociation of chloride/iodide from the two *p*-cymene complexes were not observed in solution, confirmed by their independent preparation from  $[\text{Ru}(\text{NO}_3)_2(\eta^6\text{-}p\text{-cymene})]$ , nioxime, and  $^t\text{BuOK}$ . Overall, these results suggest that the dissociation or absence of the halide ligand results in the labilization of the *p*-cymene ligand in methanol. Consistently with this hypothesis and with the greater lability of Ru-Cl bonds with respect to Ru-I, reactions of the chloride analogue  $[2]^+$  with Brønsted bases often caused a partial cleavage of *p*-cymene.

#### *7.4 Catalytic activity in the hydrogenation/N-methylation of nitroarenes*

The catalytic capabilities of Ru(II)-dioxime complexes  $[1-7]^+$  in the reduction/*N*-methylation of nitroarenes were assessed via GC-FID,

employing nitrobenzene (a1) as a model compound and methanol as both the reductive agent and C1 alkylating source (Table 105).

**Table 105.** Optimization of the N-methylation of nitrobenzene with methanol mediated by [3]NO<sub>3</sub>.<sup>a</sup>

Entry	[3]NO <sub>3</sub> (mol%)	T (°C)	t (h)	Base (eq.) <sup>b</sup>	Conv. (%) <sup>c</sup>	Selectivity (%) <sup>d</sup>	
						b1	c1
1	5	100	24	<sup>t</sup> BuOK (1.0)	50	50	50
2 <sup>e</sup>	5	100	24	<sup>t</sup> BuOK (1.0)	34	28	72
3	5	130	24	<sup>t</sup> BuOK (1.0)	>99	96	4
4	5	130	18	<sup>t</sup> BuOK (1.0)	>99	95	4
5	5	130	10	<sup>t</sup> BuOK (1.0)	81	72	28
6	4	130	18	<sup>t</sup> BuOK (1.0)	98	96	4
7	3	130	18	<sup>t</sup> BuOK (1.0)	90	90	10
8	2	130	18	<sup>t</sup> BuOK (1.0)	85	93	7
9	-	130	18	<sup>t</sup> BuOK (1.0)	0	-	-
10	4	130	18	Cs <sub>2</sub> CO <sub>3</sub> (1.0)	64	92	8
11	4	130	18	NaOCH <sub>3</sub> (1.0)	71	89	11
12	4	130	18	KOH (1.0)	78	94	6
13	4	130	18	<sup>t</sup> BuOK (0.5)	75	88	12
14	4	130	18	-	53	41	59
15 <sup>f</sup>	4	130	18	<sup>t</sup> BuOK (0.04)	64	58	42

16 <sup>g</sup>	4	130	18	<sup>t</sup> BuOK (1.0)	94	90	10
-----------------	---	-----	----	----------------------------	----	----	----

<sup>a</sup> Reaction conditions: nitrobenzene (0.5 mmol), catalyst [3]NO<sub>3</sub> (mol%), base (eq.) in methanol (1 mL). <sup>b</sup> Equivalents calculated on the mol. of nitrobenzene. <sup>c</sup> Conversion based on the consumption of nitrobenzene, determined by GC-FID using mesitylene as an internal standard. <sup>d</sup> Selectivity determined by GC-FID using mesitylene as an internal standard. <sup>e</sup> Reaction under air. <sup>f</sup> Reaction performed in the presence of 3 Å molecular sieves. <sup>g</sup> Reaction performed in the presence of 1.5 g of Hg (7.5 mmol, 378 eq.).

In an initial experiment using 5 mol% of [3]NO<sub>3</sub> as a catalyst with 1 eq. of potassium tert-butoxide (<sup>t</sup>BuOK) at 100°C for 24 h under nitrogen, a 50% conversion was observed, with a 50% selectivity towards the desired N-methylaniline (b1) and 50% towards aniline (c1) (entry 1). Notably, no N,N-dimethyl aniline was detected. The presence of air adversely affected [3]NO<sub>3</sub>'s catalytic performance, reducing conversion to 34% and selectivity for b1 to 28% (entry 2). Optimizing conditions for [3]NO<sub>3</sub>, a temperature increase to 130 °C yielded full conversion of a1 and increased selectivity to 96% for b1 (entry 3). Operating at this temperature allowed shortening the reaction time to 18 h without loss of conversion or selectivity (entry 4). However, a notable decrease in b1 yield was observed with shorter reaction times (entry 5). The catalyst amount could be reduced to 4 mol% without affecting the reaction outcome (98% conversion, 96% b1, entry 6). Further reductions to 3 and 2 mol% had negative effects on both conversion and selectivity (entries 7, 8). The reaction did not proceed in the absence of [3]NO<sub>3</sub> (entry 9). [3]NO<sub>3</sub>'s catalytic performance was significantly influenced by the type and amount of base. Conversion strongly depended on base strength (entries 10–12 vs. 6). Decreasing <sup>t</sup>BuOK from 1 to 0.5 eq. negatively impacted efficiency (75% conversion, 88% selectivity, entry 13). The absence of a base further reduced efficiency (entry 14). Stoichiometric

base amounts are commonly used in catalytic N-methylation or reduction/N-methylation reactions. A test with a catalytic amount of  $t\text{BuOK}$  and 3 Å molecular sieves resulted in very low conversion (entry 15), suggesting that  $t\text{BuOK}$  consumption by water generated during  $\text{PhNO}_2$  hydrogenation and  $\text{PhNH}_2$  methylation did not affect the catalytic process. Thus, optimized conditions are  $[\text{nitroarene}] = 0.5 \text{ M}$ , 4 mol% catalytic precursor, 1 eq.  $t\text{BuOK}$ ,  $130^\circ\text{C}$  for 18 h. To distinguish homogeneous molecular catalysis from nanoparticle metal catalysis, a mercury poisoning test was performed. No significant difference was observed under optimized conditions in the presence of Hg (entry 16), suggesting a homogeneous nature of the catalytic system. Under these conditions, the reaction selectively provided N-methylaniline, with no detection of theoretically possible by-products such as nitrosobenzene, azobenzene, or azoxybenzene, highlighting the excellent selectivity of the procedure. Following identification of the optimal conditions, a comparison of the catalytic performances of dioxime-based compounds [1-7]<sup>+</sup> and selected Ru complexes in the benchmark reaction was conducted (see Table 16 for an overview).



**Table 16.** Comparison of the catalytic properties of Ru complexes in the reduction/N-methylation of nitrobenzene with methanol.<sup>a</sup>

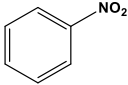
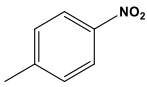
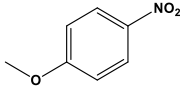
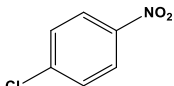
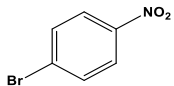
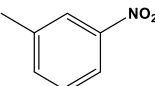
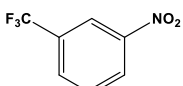
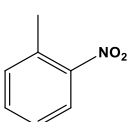
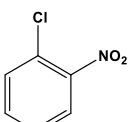
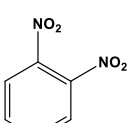
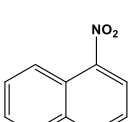
Entry	Catalyst	Conv. (%) <sup>b</sup>	Selectivity (%) <sup>c</sup>	
			b1	c1
1	<b>RuCl<sub>3</sub>·xH<sub>2</sub>O</b>	> 99	59	41
2	<b>D1</b>	> 99	66	34
3	<b>D2</b>	> 99	52	48
4	<b>D3</b>	84	63	37
5	<b>D4</b>	70	67	33
6	<b>D5</b>	89	66	34
7	[1]NO <sub>3</sub>	91	91	9
8	[2]PF <sub>6</sub>	95	87	13
9	[3]NO <sub>3</sub>	98	96	4
10	[4]NO <sub>3</sub>	95	90	10
11	[5]NO <sub>3</sub>	> 99	87	13
12	[6]PF <sub>6</sub>	45	80	20
13	[7]NO <sub>3</sub>	94	84	16
14	<b>2<sup>H</sup></b>	78	51	49
15	<b>4<sup>H</sup></b>	58	65	35
16	<b>N1</b>	96	55	45
17	<b>N2</b>	73	74	26
18	<b>N3</b>	86	65	35

<sup>a</sup> Reaction conditions: nitrobenzene (0.5 mmol), catalyst (4 mol%), <sup>t</sup>BuOK (1 eq.) in methanol (1 mL) at 130°C for 18h. <sup>b</sup> Conversion based on the consumption of nitrobenzene, determined by GC-FID using mesitylene as an internal standard. <sup>c</sup> Selectivity determined by GC-FID using mesitylene as internal standard.

Table 16 indicates significant variability in catalyst activity, with notable differences in selectivity toward the N-methylation product.  $\text{RuCl}_3 \cdot n\text{H}_2\text{O}$  catalyzed complete nitrobenzene conversion, but at this low catalyst loading, selectivity was suboptimal, resulting in a 41/59 mixture of aniline/*N*-methylaniline (entry 1).  $\eta^6$ -coordination of an arene in  $[\text{RuCl}_2(\text{arene})]_2$  complexes (D1, D3, D4) slightly improved selectivity, with *N*-methylaniline yield ranging from 63 to 67% (entries 2, 4, 5). Complex activity depended on the coordinated arene, as evidenced by differences between D1, D3, and D4. The coordinated halide also influenced catalytic performance, with the iodide complex D2 providing 14% less *N*-methylaniline than its chlorido counterpart D1 (entry 3 vs. 2). Cationic Ru(II) dioxime complexes generally demonstrated significant improvement in catalytic performance compared to their starting materials (entries 7–13).  $[1-5]^+$  and  $[7]^+$  exhibited high activities (91 to 99% conversion) and excellent selectivity toward *N*-methylaniline (80–96%), outperforming halido-bridged dimers (52–67%). Comparison of  $[\text{RuCl}(\text{C}_6\text{Me}_6)(\text{dioxime})]^+$  complexes highlighted the influence of aliphatic substituents, with methyl- or cyclohexyl-substituted complexes demonstrating high activity and selectivity, while phenyl ring modifications in  $[6]\text{PF}_6$  decreased both conversion and selectivity (entry 12). The effect of  $\eta^6$ -arene on catalytic activity was less pronounced for dimethylglyoxime or nioxime complexes than for the respective dimers (D1, D3, and D4). For nioxime/*p*cymene complexes, the presence of iodido instead of chlorido significantly increased catalytic properties, especially selectivity to b1, rising from 87% to a remarkable 96% (entry 9 vs. 8). Interestingly, the opposite effect was observed for diruthenium precursors. Overall,  $[3]\text{NO}_3$  exhibited the best

catalytic performance among dioxime complexes and was selected for further investigations. Ru-dioxime complexes are easily deprotonated, and the strong basic reaction conditions suggest the in situ formation of dioximato complexes. However, a drastic drop in conversion and selectivity was observed when isolated oxime-oximato complexes 2-H and 4-H were tested as catalysts for the methylation of nitrobenzene (entries 14, 15 vs. 8, 10). Finally, we compared dioxime-based complexes to related ruthenium(II) p-cymene compounds containing different types of  $\kappa_2N$  ligands. The catalytic performance of N1, containing a bidentate  $\alpha$ -diimine ligand without pendant OH groups, was analyzed. In comparison with [1-7]<sup>+</sup>, N1 exhibited similar activity but 51% lower selectivity (entry 16). The activity of the ethylenediamine compound N2 and one of the Noyori-Ikariya complexes (N3) was also evaluated. Both compounds, containing NH groups, which can be deprotonated in basic conditions, acted as proton buffers. Notably, both N2 and N3 were less active and significantly less selective than dioxime compounds (entries 17, 18). These comparisons highlight the crucial role played by the dioxime ligand in the transfer hydrogenation/N-methylation of nitrobenzene with methanol, aligning with the beneficial effects provided by ancillary hydroxyl groups on the catalyst, as discussed in the introduction. Encouraged by the promising results, particularly the high activity and selectivity of [3]NO<sub>3</sub> towards *N*-methylaniline, we further explored the scope of this catalytic methodology for the *N*-methylation of a series of substituted nitroarenes (Table 17).

**Table 17.** Reduction/*N*-methylation of a series of nitroarenes with methanol catalyzed by [3]NO<sub>3</sub>.<sup>a</sup>

Entry	Substrate	Conv. (%) <sup>b</sup>	Selectivity (%) <sup>c</sup>	
			b	c
1		98	96 (89) <sup>d</sup>	4
2		> 99	96 (91) <sup>d</sup>	4
3		87	80 (65) <sup>d</sup>	20
4 <sup>e</sup>		> 99 <sup>e</sup>	99 <sup>f</sup>	/
5 <sup>e</sup>		92 <sup>e</sup>	99 <sup>g</sup>	/
6		96	85 (78) <sup>d</sup>	15
7		95	92 (82) <sup>d</sup>	8
8		96	70 (64) <sup>d</sup>	30
9 <sup>e</sup>		97	87 <sup>h</sup>	13
10		97 <sup>g</sup>	90 <sup>i</sup> (84) <sup>d</sup>	10 <sup>j</sup>
11		74	79 (52) <sup>d</sup>	21

<sup>a</sup> Reaction conditions: nitroarene (0.5 mmol), [3]NO<sub>3</sub> (4 mol%), <sup>t</sup>BuOK (1 eq.) in methanol (1 mL) at 130 °C for 18h. <sup>b</sup> Conversion based on the consumption of nitrobenzene, determined by GC-FID using mesitylene as an internal standard. <sup>c</sup> Selectivity determined by GC-FID using mesitylene as internal standard. <sup>d</sup> Isolated yield of ammonium salt after treatment with 4 M HCl in dioxane. <sup>e</sup> Halogen was partially substituted by a methoxy group. <sup>f</sup> 88% of 4-methoxy-*N*-methylaniline and 11% of 4-chloro-*N*-methylaniline (not isolated). <sup>g</sup> 94% of 4-methoxy-*N*-methylaniline and 3% of 4-bromo-*N*-methylaniline (not isolated). <sup>h</sup> 57% of 2-methoxy-*N*-methylaniline and 30% of 2-chloro-*N*-methylaniline (not isolated). <sup>i</sup> Amount of 2-nitro-*N*-methylaniline. <sup>j</sup> Amount of 2-nitroaniline.

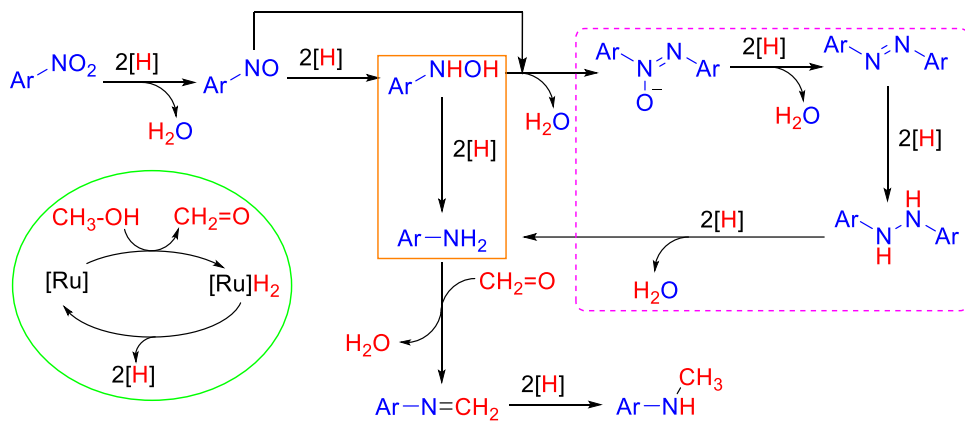
Interestingly, for all different substrates, the corresponding *N*-methylaniline was formed with high selectivity, accompanied by a minor amount of aniline. Other potential compounds, such as the corresponding nitrosobenzene, azobenzene, or azoxybenzene derivatives, were never detected. The *N*-methylated anilines were purified by silica chromatography and finally isolated as ammonium salts by treatment with 4 M HCl in dioxane. Good to excellent yields of the corresponding *N*-monomethylated products were obtained with para-substituted nitroarenes (entries 1–5). Nitrobenzene and *p*-nitrotoluene gave isolated yields of 89% (entry 1) and 91% (entry 2), respectively, of the corresponding ammonium salt. Halogen-substituted nitroarenes underwent nucleophilic aromatic substitution, resulting in the formation of methoxy derivatives, as previously reported for similar systems (entries 4, 5, 9). The presence of a strong electron-donating group, such as 4-methoxy (entry 3), slightly decreased the reactivity of our catalytic system, while an electron-withdrawing group, such as 3-CF<sub>3</sub>, was well tolerated, giving an excellent yield of the corresponding *N*-methylaniline (entry 7). Interestingly, this electron-poor substrate, studied for the first time in this work for Ru catalysts, was much less reactive than the corresponding electron-rich nitroarenes for Ir(I)–NHC

complexes. In agreement with the results obtained with other homogeneous catalytic systems for the N-methylation of nitroarenes, meta and ortho substituents were less reactive than their para analogues (entries 6, 8, and 11). In particular, the presence of ortho sterically demanding substituents or an extended aromatic scaffold, as in the case of 1-nitronaphthalene, had a negative influence on both conversion and selectivity (entries 8, 9, 11). An exception in the reactivity of ortho-substituted substrates is 1,2-dinitrobenzene, which was efficiently converted to *N*-methyl-2-nitroaniline (entry 10). This peculiar substrate, containing two reducible/methylable nitro groups, could provide up to five different products (nitro/NH<sub>2</sub>, nitro/*N*-methyl, NH<sub>2</sub>/NH<sub>2</sub>, NH<sub>2</sub>/*N*-methyl, *N*-methyl/*N*-methyl), but only the compound of transfer hydrogenation/methylation of a single NO<sub>2</sub> group was obtained (together with a 10% of 2-nitroaniline).

### 7.5 Mechanistic insights: organic intermediates

In accordance with existing literature, the catalytic transfer hydrogenation/*N*-methylation of nitrocompounds occurs through the oxidation of methanol to formaldehyde, leading to the formation of M-H species (Scheme 13, green oval). These metal hydride species subsequently catalyze the gradual reduction of nitroarenes to aniline in the first catalytic cycle, involving intermediates such as nitrosobenzene, *N*-hydroxyaniline, azoxybenzene, azobenzene, and diphenylhydrazine. This reduction can occur directly through the hydrogenation of *N*-hydroxyaniline (Scheme13, orange rectangle) or indirectly via the formation of azobenzene, originating from the reduction of

azoxybenzene generated through the coupling of nitrosobenzene and *N*-hydroxyaniline (Scheme 13, purple dashed rectangle). In the second catalytic cycle, aniline reacts with in situ generated formaldehyde to form *N*-methyleneaniline (imine), which is then hydrogenated to produce *N*-methylaniline.



Scheme 13. Overview of the reaction pathways for the Ru-catalyzed transfer hydrogenation / N-methylation of nitroarenes with methanol.

Compound [3]NO<sub>3</sub> demonstrated efficacy as a catalyst for the mono-*N*-methylation of various nitroarenes, displaying excellent activity and selectivity. Consequently, selected experiments were conducted to provide insights into the reaction mechanism. Firstly, the reaction profile of the reduction/*N*-methylation of nitrobenzene catalyzed by [3]NO<sub>3</sub>, under optimized conditions, was monitored by GC-MS to detect organic intermediates. The results revealed a marked decrease in the amount of a1 after 4 hours (approximately 70% conversion), accompanied by the formation of approximately 40% aniline (c1) and 30% *N*-methyl aniline

(b1). Subsequently, both nitrobenzene and aniline gradually decreased, reaching a final conversion of a1 of 98% at 18 h, with a selectivity for b1 of 96%. The observed accumulation of aniline until a maximum of 40% at 4 h, followed by its conversion to b1, aligns well with the two reaction cycles with aniline as a common species (Scheme 13). Importantly, no side products of the reduction of nitroarene or imine were detected at any time interval, suggesting that the conversion of these putative intermediates is rapid. To further understand the nitroarene reduction step, the reactivity of azobenzene as the starting material was evaluated. While a Pd-based catalytic system was reported to be incapable of mediating the conversion of azobenzene or azoxybenzene to b1, [3]NO<sub>3</sub> catalyzed the full conversion of azobenzene to *N*-methylaniline, confirming the effectiveness of both direct and indirect hydrogenation of nitroarenes. To elucidate the activation of methanol, the [3]NO<sub>3</sub>-catalyzed *N*-methylation of nitrobenzene was performed using either methanol-d<sub>4</sub> or methanol-d<sub>1</sub>. The results, analyzed by GC-FID, <sup>1</sup>H and <sup>13</sup>C NMR, confirmed that methanol serves as both a carbon and hydrogen source. The absence of deuterium incorporation in the *N*-methyl group using CH<sub>3</sub>OD suggested the formation of a ruthenium monohydride intermediate. A small decrease in selectivity in the experiment with CD<sub>3</sub>OD indicated a kinetic isotope effect, slowing the methylation of the in situ generated aniline. To further comprehend the high selectivity observed with [3]<sup>+</sup>, three selected complexes were compared in the nitrobenzene reduction and aniline methylation steps. Using isopropyl alcohol as the H<sub>2</sub> source in the reduction of nitrobenzene, all three complexes performed equally in this first step, fully converting nitrobenzene to aniline without detecting nitro-reduction side products



after 18 h. However, in the *N*-methylation of aniline with methanol, [3]<sup>+</sup> outperformed D1 and N<sub>2</sub>, with the formation of *N*-methylaniline being quantitative. These observations underscore the critical role of dioxime ligands in the *N*-methylation step, potentially cooperating with the metal center.

## 7.6 Experimental

### 7.6.1 General experimental details

Compounds [RuI<sub>2</sub>(η<sup>6</sup>-p-cymene)]<sub>2</sub> (D2) [16] and [RuCl(η<sup>6</sup>-p-cymene)(κ<sup>2</sup>-N-{HCN(4-C<sub>6</sub>H<sub>4</sub>CH<sub>3</sub>)}<sub>2</sub>)]CF<sub>3</sub>SO<sub>3</sub> (N1) [17] were prepared according to literature methods. New or optimized procedures for the previously-reported compounds [RuCl<sub>2</sub>(η<sup>6</sup>-p-cymene)]<sub>2</sub> (D1), [18] [RuCl<sub>2</sub>(η<sup>6</sup>-C<sub>6</sub>Me<sub>6</sub>)]<sub>2</sub> (D3) [19] [RuCl<sub>2</sub>(η<sup>6</sup>-1,3,5-C<sub>6</sub>H<sub>3</sub>Me<sub>3</sub>)]<sub>2</sub> (D4), 51 [Ru<sub>2</sub>Cl<sub>2</sub>(μ-Cl)(μ-H)(η<sup>6</sup>-p-cymene)<sub>2</sub>], (D5) [18] [RuCl{κ<sup>2</sup>-N-H<sub>2</sub>NCH<sub>2</sub>CH<sub>2</sub>NH<sub>2</sub>}(η<sup>6</sup>-p-cymene)]Cl, (N2) [20] and [RuCl{κ<sup>2</sup>-N-(1*S*,2*S*)-H<sub>2</sub>NC(Ph)C(Ph)NSO<sub>2</sub>(p-C<sub>6</sub>H<sub>4</sub>CH<sub>3</sub>)}(η<sup>6</sup>-p-cymene)], (N3). Where specified, the reactions were carried out under N<sub>2</sub> using standard Schlenk techniques. Anhydrous THF was obtained from SPS 5 solvent purifier (MBraun); MeOH was distilled over CaH<sub>2</sub> and stored over 3 Å MS. Otherwise, preparations and manipulations were carried out in air with common laboratory glassware. All the complexes were isolated as air-stable powders that were maintained under N<sub>2</sub> for long time storage as a precaution (particularly recommended for [2]NO<sub>3</sub>, [2]PF<sub>6</sub> and [6]NO<sub>3</sub>). Reaction

yields are referred to the isolated, powdered materials. Carbon, hydrogen and nitrogen analyses were performed on a Vario MICRO cube instrument (Elementar). Infrared spectra of solid samples (650–4000  $\text{cm}^{-1}$  range) were recorded on a Perkin Elmer Spectrum One FT-IR spectrometer equipped with a UATR sampling accessory. NMR spectra were recorded on a Bruker Avance II DRX400, JEOL YH JNM-ECZ400S or JNM-ECZ500R instruments equipped with broadband probes. Chemical shifts are referenced to the residual solvent peaks ( $^1\text{H}$ ,  $^{13}\text{C}$ ) or to external standard ( $^{14}\text{N}$  to  $\text{CH}_3\text{NO}_2$ ,  $^{35}\text{Cl}$  to 1 M NaCl in  $\text{D}_2\text{O}$ ). Spectra indicated as CH<sub>3</sub>OH/C<sub>6</sub>D<sub>6</sub> were recorded in CH<sub>3</sub>OH solutions using a sealed C<sub>6</sub>D<sub>6</sub> capillary for locking. NMR resonances were assigned with the assistance of  $^1\text{H}$ - $^{13}\text{C}$  gs-HSQC and/or gs-HMBC correlation experiments. UV-Vis spectra (190–900 nm) were recorded on an Ultraspec 2100 Pro spectrophotometer. IR and UV-Vis spectra were processed with Spectragryph. Conductivity measurements were carried using an XS COND 8 instrument (cell constant = 1.0  $\text{cm}^{-1}$ ) equipped with NT 55 temperature probe (measurements automatically adjusted to 25 °C).  $\text{KNO}_3$  [ $\Lambda_{\text{m}}$  (MeOH,  $2.7 \times 10^{-3}$  M): 93  $\text{S cm}^2 \text{mol}^{-1}$ ] and  $[\text{Bu}^4\text{N}]\text{Br}$  [ $\Lambda_{\text{m}}$  (MeOH,  $3.2 \times 10^{-3}$  M): 62  $\text{S cm}^2 \text{mol}^{-1}$ ] were used as a reference compounds.<sup>58</sup> Mass spectrometry measurements were performed on a quadrupole time-of-flight mass spectrometer instrument (Q-TOF) (Xevo G2 QToF; Waters) operated with MassLynx (version 4.1, Waters) software package. The spectra were scanned in the  $m/z$  range from 50 to 1200. ESI Z-spray conditions: flow rate 5  $\mu\text{L min}^{-1}$ ; electrospray capillary voltage: 3.0 kV; source temperature: 100 °C; gas:  $\text{N}_2$ ; gas temperature: 250 °C. The cone voltage was adjusted according to the MassLynx software to 20 and the extraction cone to 2. The argon buffer

gas in the T-wave was set at about 0.3 mL min<sup>-1</sup>. Gas chromatography-mass spectrometry measurements were performed by a ThermoFischer Trace 1300 series instrument equipped with a mass spectrometer ThermoFischer ISQ 4000 (230 V) detector, using a J&W HP-5 30 m × 0.32 mm × 0.25 μm film thickness fused silica column and chromatography grade helium as carrier gas.

### *7.6.2 Synthesis and characterization of dioxime and oxime-oximate complexes*

**Procedure A ([1-7]NO<sub>3</sub>).** An orange suspension of [RuCl<sub>2</sub>(η<sup>6</sup>-arene)]<sub>2</sub> (50–200 mg; arene = p-cymene, C<sub>6</sub>Me<sub>6</sub>, 1,3,5-C<sub>6</sub>H<sub>3</sub>Me<sub>3</sub>) and AgNO<sub>3</sub> (2.0 equivalents) in MeCN (ca. 5 mL) was stirred at room temperature for 1 h (3.5 h for arene = 1,3,5-C<sub>6</sub>H<sub>3</sub>Me<sub>3</sub>) under protection from the light. The resulting mixture (yellow/orange solution + colorless solid) was filtered over celite and treated with the selected dioxime (2.0 equivalents). The solution was stirred at room temperature (reflux temperature for arene = 1,3,5-C<sub>6</sub>H<sub>3</sub>Me<sub>3</sub>) for 3 h and the conversion was checked by <sup>1</sup>H NMR (CD<sub>3</sub>OD). Following an appropriate filtration step over celite, volatiles were removed under vacuum. The resulting solid was triturated in Et<sub>2</sub>O (Et<sub>2</sub>O/MeCN 6 : 1 v/v for [4]NO<sub>3</sub> and [6]NO<sub>3</sub>) and the suspension was filtered. The solid was washed with Et<sub>2</sub>O, hexane and dried under vacuum (40 °C). Note: the presence of even a slight excess of AgNO<sub>3</sub> leads to formation of by-products, among which free p-cymene; it is important to use stoichiometric amounts.

**Procedure B ([2,3]NO<sub>3</sub>).** An orange suspension of [RuX<sub>2</sub>(η<sup>6</sup>-p-cymene)]<sub>2</sub> (54–160 mg, X = Cl, I) and AgNO<sub>3</sub> (2.0 equivalents) in MeOH (5–8 mL) was stirred at room temperature for 1.5 h under protection from the light. The suspension (X = Cl: yellow-orange solution + colorless solid; X = I: red-brown solution + pale yellow solid) was filtered over celite and the filtrate was treated with nioxime (2.0 equivalents). The mixture was stirred at room temperature for 1.5 h affording a clear red (X = I) or orange (X = Cl) solution. Conversion was checked by <sup>1</sup>H NMR (CD<sub>3</sub>OD) then volatiles were removed under vacuum. The residue was dissolved in CH<sub>2</sub>Cl<sub>2</sub> (X = I: a few drops of MeOH were added to assist solubilization) and filtered over celite. The filtrate was taken to dryness under vacuum and the resulting foamy solid was triturated in Et<sub>2</sub>O/hexane 1 : 1 v/v. The suspension was filtered; the solid was washed with Et<sub>2</sub>O/hexane 1 : 1 v/v, hexane and dried under vacuum (40 °C). Alternative preparations involving the use of MeCN in both reaction steps (as in procedure A) or MeCN in the first step and MeOH in the second step led to the isolation of a more brownish solid containing [2,3]NO<sub>3</sub> and minor amounts of non-arene nioxime complexes. Coherently, the presence of free p-cymene was assessed in the final reaction mixture.

**Procedure C ([2,6]PF<sub>6</sub>).** A suspension of [RuCl<sub>2</sub>(η<sup>6</sup>-arene)]<sub>2</sub> (33–70 mg; arene = p-cymene, C<sub>6</sub>Me<sub>6</sub>) and the selected dioxime (2.0 equivalents) in EtOH (6 mL) was stirred at room temperature for 1 h, then treated with KPF<sub>6</sub> (ca. 2.2 equivalents). After 2 h, the suspension (yellow-orange solution + colorless solid) was filtered over celite and the filtrate was taken to dryness under vacuum. The residue was dissolved in CH<sub>2</sub>Cl<sub>2</sub> and filtered over celite. Volatiles were removed from the filtrate solution and

the resulting solid was triturated in Et<sub>2</sub>O. The suspension was filtered, the solid was washed with Et<sub>2</sub>O, hexane and dried under vacuum (40 °C).

**Procedure D (2–4–H).** A suspension of [RuX<sub>2</sub>(η<sup>6</sup>-arene)]<sub>2</sub> (55–70 mg; X = Cl, I; arene = *p*-cymene, C<sub>6</sub>Me<sub>6</sub>) and the selected dioxime (2.0 equivalents) in MeOH (4 mL) was stirred at room temperature for 1.5 h, then treated with NaHCO<sub>3</sub> (2.0 equivalents) and stirred for 2 h. A yellow (X = Cl) or yellow-brown (X = I) solution formed within few minutes. For 2–H and 4–H: volatiles were removed under vacuum and the residue was suspended in CH<sub>2</sub>Cl<sub>2</sub>. For 3–H: the final mixture was diluted with MeOH. The suspension was filtered over celite and the filtrate was taken to dryness under vacuum. The resulting solid was triturated in Et<sub>2</sub>O and filtered. The solid was washed with Et<sub>2</sub>O, hexane and dried under vacuum (40 °C).

*[RuCl(κ<sup>2</sup> N-{CH<sub>3</sub>CNOH}<sub>2</sub>)(η<sup>6</sup>-*p*-cymene)]NO<sub>3</sub>, [1]NO<sub>3</sub> (Chart 1).* Prepared from [RuCl<sub>2</sub>(η<sup>6</sup>-*p*-cymene)]<sub>2</sub> (54 mg, 0.088 mmol, 1 eq.), AgNO<sub>3</sub> (30 mg, 0.18 mmol) and dimethylglyoxime (20 mg, 0.18 mmol), according to procedure A. Final reaction mixture: yellow-orange solution; filtered over celite. Orange solid, yield: 62 mg, 77%. Soluble in MeOH, MeCN, insoluble in Et<sub>2</sub>O, toluene. Anal. calcd. for C<sub>14</sub>H<sub>22</sub>ClN<sub>3</sub>O<sub>5</sub>Ru: C, 37.46; H, 4.94; N, 9.36; found: C, 36.3; H, 4.47; N, 8.91. IR (solid state):  $\tilde{\nu}/\text{cm}^{-1}$  = 3300–3100m-br (OH), 3071-3057w-br, 2971w, 2925w, 2730-2701w, 1464m-sh, 1435m-sh, 1389m, 1364m, 1323 m, 1254s-br (NO<sub>3</sub>), 1193s, 1162w-sh, 1118w, 1064s (NO), 1035m, 1006s, 875w, 824w, 804w, 720w, 674w. <sup>1</sup>H NMR (CD<sub>3</sub>OD):  $\delta/\text{ppm}$  = 6.06 (d, 3 J<sub>HH</sub> = 6.4 Hz, 2H, C<sub>4</sub> H), 5.69 (d, 3 J<sub>HH</sub> = 6.4 Hz, 2H, C<sub>3</sub> H), 2.71 (hept, 3 J<sub>HH</sub> = 7.0 Hz, 1H, C<sub>6</sub> H), 2.32 (s, 6H, C<sub>9</sub> H), 2.28 (s, 3H, C<sub>1</sub> H), 1.18 (d, 3 J<sub>HH</sub> = 6.9 Hz, 6H, C<sub>7</sub>

H).  $^{13}\text{C}\{^1\text{H}\}$  NMR ( $\text{CD}_3\text{OD}$ ):  $\delta/\text{ppm} = 161.0$  (C8),  $109.9$  (C5),  $107.0$  (C2),  $88.9$  (C4),  $85.7$  (C3),  $32.6$  (C6),  $22.4$  (C7),  $19.3$  (C1),  $13.6$  (C9).  $^{14}\text{N}$  NMR ( $\text{CD}_3\text{OD}$ ):  $\delta(\text{ppm}) = -3.7$  ( $\Delta\nu_{1/2} = 21$  Hz,  $\text{NO}_3^-$ ).

$[\text{RuCl}(\kappa^2\text{-}N\text{-}\{\text{CH}_2\text{CH}_2\text{CNOH}\}_2)(\eta^6\text{-}p\text{-cymene})]X$ ,  $[2]X$  ( $X = \text{NO}_3, \text{PF}_6$ ; Chart 2).

$[2]\text{PF}_6$ . Prepared from  $[\text{RuCl}_2(\eta^6\text{-}p\text{-cymene})]_2$  (70 mg, 0.114 mmol), nioxime (33 mg, 0.23 mmol) and  $\text{KPF}_6$  (45 mg, 0.24 mmol), according to procedure C. Ochre yellow-orange solid, yield: 104 mg, 82%. Alternatively prepared according to procedure A, using  $\text{NH}_4\text{PF}_6$  (89 mg, 0.545 mmol) in place of  $\text{AgNO}_3$ ,  $[\text{RuCl}_2(\eta^6\text{-}p\text{-cymene})]_2$  (165 mg, 0.269 mmol) and nioxime (78 mg, 0.549 mmol). Yield: 256 mg, 85%. Stored under  $\text{N}_2$  (partially decomposed to a dark brown solid after several months when stored in air). Soluble in MeCN, acetone, water, less soluble in  $\text{CH}_2\text{Cl}_2$ , poorly soluble in  $\text{CHCl}_3$ , insoluble in  $\text{Et}_2\text{O}$ , toluene. Anal. calcd. For  $\text{C}_{16}\text{H}_{24}\text{-ClF}_6\text{N}_2\text{O}_2\text{PRu}$ : C, 34.45, H, 4.34, N, 5.02; found: C, 33.92, H, 4.16, N, 5.01. IR (solid state):  $\tilde{\nu}/\text{cm}^{-1} = 3640\text{-}3600\text{w}$  (OH),  $3563\text{w}$  (OH),  $3433\text{w-br}$  (OH),  $2436\text{w}$ ,  $3100\text{m-br}$ ,  $2097\text{m}$ ,  $2949\text{w}$ ,  $2878\text{w}$ ,  $1546\text{w}$ ,  $1508\text{w}$ ,  $1470\text{m}$ ,  $1461\text{m}$ ,  $1456\text{m}$ ,  $1432\text{m}$ ,  $1425\text{m}$ ,  $1387\text{m-sh}$ ,  $1396\text{s}$ ,  $1309\text{s}$ ,  $1258\text{w}$ ,  $1242\text{w}$ ,  $1189$  m,  $1167\text{w}$ ,  $1116\text{w}$ ,  $1094\text{w}$ ,  $1039\text{s}$  (NO),  $1009\text{w}$ ,  $972\text{m}$ ,  $923\text{w}$ ,  $908\text{w}$ ,  $838\text{vs}$  ( $\text{PF}_6$ ),  $817\text{vs-sh}$ ,  $786$  s,  $739\text{m}$ ,  $729$  s,  $680\text{w}$ .  $^1\text{H}$  NMR (acetone- $d_6$ ):  $\delta/\text{ppm} = 6.38$  (d, 3 JHH = 6.0 Hz, C4 H),  $5.91$  (d, 3 JHH = 6.0 Hz, C3 H),  $3.00\text{-}2.79$  (m, 5H, C6 H+C9 H),  $2.27$  (s, 3H, C1 H),  $1.77\text{-}1.60$  (m, 4H, C10H),  $1.21$  (d, 3 JHH = 6.9 Hz, 6H, C7 H); N(OH) signals were not detected (rapid H/D exchange with residual water).  $^1\text{H}$  NMR ( $\text{CD}_3\text{OD}$ ):  $\delta/\text{ppm} = 6.07$  (d, 3 JHH = 6.3 Hz, 2H, C4 H),  $5.69$  (d, 3 JHH = 6.3 Hz, 2H, C3 H),  $2.94\text{-}2.78$  (m, 4H, C9 H),  $2.72$  (hept, 3 JHH = 6.9 Hz, 1H, C6 H),  $2.28$  (s, 3H, C1 H),  $1.73\text{-}1.62$  (m, 4H, C10H),  $1.18$  (d, 3 JHH =

6.9 Hz, 6H, C7 H). No changes in the  $^1\text{H}$  NMR spectrum were observed after 14 h at room temperature.  $^{13}\text{C}\{^1\text{H}\}$  NMR ( $\text{CD}_3\text{-OD}$ ):  $\delta/\text{ppm} = 161.0$  (C8),  $110.0$  (C2),  $106.9$  (C5),  $88.7$  (C4),  $85.4$  (C3),  $32.7$  (C6),  $27.2$  (C9),  $22.4$  (C7),  $21.4$  (C10),  $19.3$  (C1).  $^{19}\text{F}$  NMR ( $\text{CD}_3\text{OD}$ ):  $\delta/\text{ppm} = -74.8$  (d,  $1\text{ JFP} = 708\text{ Hz}$ , PF6<sup>-</sup>).  $^{31}\text{P}$  NMR ( $\text{CD}_3\text{OD}$ ):  $\delta/\text{ppm} = -144.6$  (hept,  $1\text{ JFP} = 708\text{ Hz}$ , PF6<sup>-</sup>).

*[2]NO<sub>3</sub>*. Prepared from  $[\text{RuCl}_2(\eta^6\text{-p-cimene})]_2$  (54 mg, 0.088 mmol),  $\text{AgNO}_3$  (30 mg, 0.18 mmol) and nioxime (26 mg, 0.18 mmol), according to procedure B. Ochre yelloworange solid, yield: 67 mg, 67%. Stored under  $\text{N}_2$ . Soluble in acetone, MeOH,  $\text{CH}_2\text{Cl}_2$ ; insoluble in  $\text{Et}_2\text{O}$ , hexane. Anal. Calcd. For:  $\text{C}_{16}\text{H}_{24}\text{ClN}_3\text{O}_5\text{Ru}$ : C, 40.47; H, 5.09; N, 8.85. Found: C, 40.33; H, 5.13; N, 8.68. IR (solid state):  $\tilde{\nu}/\text{cm}^{-1} = 3060\text{w}$ ,  $2945\text{m}$ ,  $2873\text{m}$ ,  $2700\text{w-br}$ ,  $1472\text{m-sh}$ ,  $1447\text{m-sh}$ ,  $1434\text{m}$ ,  $1417\text{s}$ ,  $1388\text{s}$ ,  $1379\text{s}$ ,  $1363\text{m}$ ,  $1325\text{m}$ ,  $1299\text{m-sh}$ ,  $1262\text{s}$ ,  $1243\text{s}$  (NO<sub>3</sub>),  $1184\text{s}$ ,  $1163\text{s-sh}$ ,  $1086\text{w}$ ,  $1072\text{w}$ ,  $1038\text{m}$  (NO),  $1019\text{m-sh}$ ,  $971\text{ s}$ ,  $909\text{w}$ ,  $890\text{w}$ ,  $873\text{w}$ ,  $823\text{w}$ ,  $805\text{w}$ ,  $750\text{w}$ ,  $713\text{-}677\text{w}$ .  $^1\text{H}$  NMR ( $\text{CD}_3\text{OD}$  or acetone- $d_6$ ): identical to the PF6<sup>-</sup> salt. UV-vis (MeOH,  $2.1 \cdot 10^{-3}\text{ M}$ ):  $\lambda_{\text{max}}/\text{nm}$  ( $\epsilon/\text{M}^{-1} \cdot \text{cm}^{-1}$ ) =  $243\text{sh}$  ( $8 \times 10^3$ ),  $274\text{sh}$  ( $6.3 \times 10^3$ ),  $328$  ( $5.0 \times 10^3$ ),  $390\text{br}$  ( $1.9 \times 10^3$ ).  $\Lambda\text{m}$  (MeOH,  $2.1 \times 10^{-3}\text{ M}$ ):  $93\text{ S cm}^2\text{ mol}^{-1}$ .

*[RuI( $\kappa^2$  N-{CH<sub>2</sub>CH<sub>2</sub>CNOH})<sub>2</sub>]( $\eta^6$ -p-cymene)]NO<sub>3</sub>, [3]NO<sub>3</sub> (Chart 3)*. Prepared from  $[\text{RuI}_2(\eta^6\text{-p-cymene})]_2$  (160 mg, 0.164 mmol),  $\text{AgNO}_3$  (55.5 mg, 0.327 mmol) and nioxime (47 mg, 0.33 mmol), according to procedure B. Orange-brown solid, yield: 160 mg, 86%. Soluble in MeOH, MeCN, acetone, water, less soluble in  $\text{CH}_2\text{Cl}_2$ ,  $\text{H}_2\text{O}$ , insoluble in  $\text{Et}_2\text{O}$ . X-ray quality needle-like crystals of [3]NO<sub>3</sub> were obtained from an EtOH solution layered with a toluene/hexane mixture and settled aside at  $-20$

°C. Anal. calcd. for  $C_{16}H_{24}IN_3O_5Ru$ : C, 33.93; H, 4.27; N, 7.42. Found: C, 33.84; H, 4.35; N, 7.52. IR (solid state):  $\tilde{\nu}/\text{cm}^{-1}$  = 3200w-br (OH), 3079w, 2955w, 2931w, 2870w, 2740w-br, 1454m-sh, 1418m-sh, 1388s, 1368s, 1326m-sh, 1270s (NO<sub>3</sub>), 1243s, 1186s, 1164s-sh, 1135m-sh, 1113m, 1086m, 1043s (NO), 1019m-sh, 969s, 906w, 879w, 825w, 805w, 789w, 733w, 714w. <sup>1</sup>H NMR (CD<sub>3</sub>OD):  $\delta/\text{ppm}$  = 5.99 (d, 3 J<sub>HH</sub> = 6.2 Hz, 2H, C4 H), 5.65 (d, 3 J<sub>HH</sub> = 6.1 Hz, 2H, C3 H), 2.97–2.74 (m, 5H, C9 H+C6 H), 2.65 (s, 3H, C1 H), 1.73–1.56 (m, 4H, C10H), 1.20 (d, 3 J<sub>HH</sub> = 6.9 Hz, 6H, C7 H). <sup>13</sup>C{<sup>1</sup>H} NMR (CD<sub>3</sub>-OD):  $\delta/\text{ppm}$  = 159.8 (C8 ), 110.1 (C2 ), 108.2 (C5 ), 88.6 (C4 ), 86.0 (C3 ), 33.2 (C6 ), 27.3 (C9 ), 22.4 (C7 ), 21.8 (C1 ), 21.5 (C10).

*[RuCl( $\kappa^2$  N-{CH<sub>3</sub>CNOH})<sub>2</sub>]( $\eta^6$ -C<sub>6</sub>Me<sub>6</sub>)]NO<sub>3</sub>, [4]NO<sub>3</sub> (Chart 4).* Prepared from [RuCl<sub>2</sub>( $\eta^6$ -C<sub>6</sub>Me<sub>6</sub>)<sub>2</sub>] (60 mg, 0.090 mmol), AgNO<sub>3</sub> (30 mg, 0.18 mmol) and dimethylglyoxime (21 mg, 0.18 mmol), according to procedure A. Final reaction mixture: pale yellow solution and yellow solid; dried under vacuum, dissolved in MeOH and filtered over celite. Yellow solid, yield: 68 mg, 82%. Soluble in MeOH, water, poorly soluble in MeCN, insoluble in Et<sub>2</sub>O. X-ray quality crystals of [4]NO<sub>3</sub>·H<sub>2</sub>O were obtained from an EtOH solution spiked with a drop of 65% HNO<sub>3</sub>(aq), layered with Et<sub>2</sub>O and settled aside at –20 °C. Anal. calcd. for  $C_{16}H_{26}ClN_3O_5Ru$ : C, 40.30; H, 5.50; N, 8.81; found: C, 40.12; H, 5.68; N, 8.82. IR (solid state):  $\tilde{\nu}/\text{cm}^{-1}$  = 3022m-sh (OH), 2297m-sh, 2914m, 2656m-br, 1612w, 1534w, 1416s, 1386s, 1276s (NO<sub>3</sub>), 1192s, 1072s (NO), 1039m, 1016m, 998 s, 962 s, 833w, 826w, 719w, 668w. <sup>1</sup>H NMR (CD<sub>3</sub>OD):  $\delta/\text{ppm}$  = 2.30 (s, 6H, C4 H), 2.17 (s, 18H, C1 H). <sup>13</sup>C{<sup>1</sup>H} NMR (CD<sub>3</sub>OD):  $\delta/\text{ppm}$  = 162.3 (C3 ), 99.7 (C2 ), 15.8 (C1 ), 13.7 (C4 ). UV-vis (MeOH, 2.1 × 10<sup>-3</sup> M):  $\lambda_{\text{max}}/\text{nm}$  ( $\epsilon/\text{M}^{-1} \text{cm}^{-1}$ ) = 345 (4.0 × 10<sup>3</sup> ), 403 (2.9 × 10<sup>3</sup> ).  $\lambda_{\text{m}}$  (MeOH, 2.1 × 10<sup>-3</sup> M)



10–3 M): 102 S cm<sup>2</sup> mol<sup>-1</sup>.  $[RuCl(\kappa^2 N-\{CH_2CH_2CNOH\}_2)(\eta^6-C_6Me_6)]NO_3$ ,  $[5]NO_3$  (Chart 5). Prepared from  $[RuCl_2(\eta^6-C_6Me_6)]_2$  (99 mg, 0.148 mmol),  $AgNO_3$  (50 mg, 0.30 mmol) and nioxime (42 mg, 0.30 mmol), according to procedure A. Final reaction mixture: yellow-orange solution + solid; dried under vacuum, dissolved in MeOH and filtered over celite. Yellow-ochre solid, yield: 144 mg, 97%. Soluble in MeOH, less soluble in MeCN, poorly soluble in  $CH_2Cl_2$ , insoluble in  $Et_2O$ , hexane. Anal. calcd. for  $C_{18}H_{28}ClN_3O_5Ru$ : C, 42.99; H, 5.61; N, 8.35. Found: C, 43.06; H, 5.45; N, 8.29. IR (solid state):  $\tilde{\nu}/cm^{-1}$  = 3441w (OH), 3366w (OH), 2945m, 2875w, 2660m-br, 1452m-sh, 1435s-sh, 1393s, 1377s, 1350s-sh, 1315m, 1273s (NO<sub>3</sub>), 1256s-sh, 1238s-sh, 1184s, 1165m, 1141m, 1073m, 1031s (NO), 970m, 904m, 866w, 823w, 778w, 731w, 718w. <sup>1</sup>H (CD<sub>3</sub>OD):  $\delta/ppm$  = 2.98– 2.79 (m, 4H, C4 H), 2.19 (s, 18H, C1 H), 1.80– 1.58 (m, 4H, C5 H). <sup>13</sup>C{<sup>1</sup>H} (CH<sub>3</sub>OH/C<sub>6</sub>D<sub>6</sub>):  $\delta/ppm$  = 163.4 (C3 ), 99.6 (C2 ), 27.2 (C4 ), 21.2 (C5 ), 15.6 (C1 ). <sup>14</sup>N (CD<sub>3</sub>OD):  $\delta/ppm$  = -4.3 ( $\Delta\nu_{1/2}$  = 20 Hz).

$[RuCl(\kappa^2 N-\{PhCNOH\}_2)(\eta^6-C_6Me_6)]X$ ,  $[6]X$  ( $X = NO_3, PF_6$ ; Chart 6).  $[6]NO_3$ . Prepared from  $[RuCl_2(\eta^6-C_6Me_6)]_2$  (166 mg, 0.248 mmol),  $AgNO_3$  (85 mg, 0.50 mmol) and diphenyldioxime (125 mg, 0.518 mmol), according to procedure A. Final reaction mixture: pale yellow solution and orange solid; dried under vacuum, dissolved in MeOH and filtered over celite. Orangebrown solid, yield: 261 mg, 87%. Stored under N<sub>2</sub>. Soluble in MeOH, poorly soluble in MeCN, insoluble in  $Et_2O$ . Anal. calcd. for  $C_{26}H_{30}ClN_3O_5Ru$ : C, 51.96; H, 5.03; N, 6.99; found: C, 51.26; H, 4.88; N, 6.83. IR (solid state):  $\tilde{\nu}/cm^{-1}$  = 3463-3405w-br (OH), 3027w, 2878w-br, 2600w-br, 1433m, 1402s, 1393s, 1353s, 1272s (NO<sub>3</sub>), 1247s, 1220s, 1120w, 1089s (NO), 1072m, 1063m, 1038m, 1028m, 1016m, 1001m,

922w, 886m, 847w, 819w, 795w, 774w, 764 m, 724s, 694s. <sup>1</sup>H NMR (CD<sub>3</sub>OD): δ/ppm = 7.36–7.24 (m, 6H, C<sub>6</sub> H+C<sub>7</sub> H), 7.09–7.04 (m, 4H, C<sub>5</sub> H), 2.28 (s, 18H, C<sub>1</sub> H). <sup>13</sup>C{<sup>1</sup>H} NMR (CD<sub>3</sub>OD): δ/ppm = 163.6 (C<sub>3</sub>), 131.3 (C<sub>7</sub>), 130.7 (C<sub>6</sub>), 130.1 (C<sub>4</sub>), 129.3 (C<sub>5</sub>), 101.5 (C<sub>2</sub>), 16.0 (C<sub>1</sub>). <sup>14</sup>N NMR (CD<sub>3</sub>-OD): δ/ppm = -5.3 (Δν<sub>1/2</sub> = 19 Hz, NO<sub>3</sub>).

[6]PF<sub>6</sub>. Prepared from [RuCl<sub>2</sub>(η<sup>6</sup>-C<sub>6</sub>Me<sub>6</sub>)]<sub>2</sub> (101 mg, 0.151 mmol), diphenyldioxime (73 mg, 0.30 mmol) and KPF<sub>6</sub> (60 mg, 0.33 mmol), according to procedure C. Orange solid, yield: 176 mg, 85%. Unlike in the preparation of [2]PF<sub>6</sub>, no reaction occurs until the addition of KPF<sub>6</sub> (the insoluble [RuCl<sub>2</sub>(η<sup>6</sup>-C<sub>6</sub>Me<sub>6</sub>)]<sub>2</sub> did not react with nioxime). Soluble in MeOH, EtOH, CH<sub>2</sub>Cl<sub>2</sub>, poorly soluble in Et<sub>2</sub>O. Anal. calcd. For. C<sub>26</sub>H<sub>30</sub>ClN<sub>3</sub>O<sub>5</sub>Ru: C, 45.65; H, 4.42; N, 4.10. Found: C, 45.35; H, 4.54; N, 4.03. <sup>1</sup>H NMR (CD<sub>3</sub>OD): δ/ppm = identical to the NO<sub>3</sub> - salt. <sup>19</sup>F NMR (CD<sub>3</sub>OD): δ/ppm = -74.8 (d, J = 706 Hz). <sup>19</sup>F NMR (CD<sub>3</sub>OD): δ/ppm = -74.8 (d, 1 JFP = 706 Hz, PF<sub>6</sub> -). <sup>31</sup>P NMR (CD<sub>3</sub>OD): δ/ppm = -144.6 (hept, 1 JFP = 706 Hz, PF<sub>6</sub> -).

[RuCl(κ<sup>2</sup>-N-{CH<sub>2</sub>CH<sub>2</sub>CNOH})<sub>2</sub>](η<sup>6</sup>-1,3,5-C<sub>6</sub>H<sub>3</sub>Me<sub>3</sub>)]NO<sub>3</sub>, [7] NO<sub>3</sub> (Chart 7). Prepared from [RuCl<sub>2</sub>(η<sup>6</sup>-1,3,5-C<sub>6</sub>H<sub>3</sub>Me<sub>3</sub>)]<sub>2</sub> (53 mg, 0.090 mmol), AgNO<sub>3</sub> (32 mg, 0.19 mmol) and nioxime (27 mg, 0.19 mmol), according to procedure A. Final reaction mixture: brown solution; dried under vacuum, dissolved in acetone and filtered over celite. Brown solid, yield: 71 mg, 86%. Soluble in MeOH, acetone; poorly soluble in CH<sub>2</sub>Cl<sub>2</sub>, insoluble in Et<sub>2</sub>O, hexane. Anal. calcd. for C<sub>15</sub>H<sub>22</sub>ClN<sub>3</sub>O<sub>5</sub>Ru: C, 39.09; H, 4.81; N, 9.12. Found: C, 38.95; H, 4.90; N, 9.06. IR (solid state):  $\tilde{\nu}$ /cm<sup>-1</sup> = 3420w-br (OH), 3078w, 3041w, 2945 m, 2870 m, 2701w-br, 1881w, 1646w, 1531w, 1452m-sh, 1417s-sh, 1378s, 1323-sh, 1299s-sh, 1272s,

1252s (NO<sub>3</sub>), 1186s, 1166m-sh, 1072w, 1033s (NO), 1012w-sh, 989w, 970m, 905w, 887w, 824w, 785w, 732w, 714w. <sup>1</sup>H NMR (CD<sub>3</sub>OD): δ/ppm = 5.38 (s, 3H, C3 H), 2.82 (app. t, 3 J<sub>HH</sub> = 6.5 Hz, 4H, C5 H), 2.32 (s, 9H, C1 H), 1.79–1.70, 1.68–1.60 (m, 4H, C6 H). <sup>13</sup>C{<sup>1</sup>H} NMR (CD<sub>3</sub>OD): δ/ppm = 160.6 (C4 ), 111.6 (C2 ), 81.3 (C3 ), 27.1 (C5 ), 21.6 (C6 ), 19.5 (C1 ). <sup>14</sup>N NMR (CD<sub>3</sub>OD): δ/ppm = -3.9 (Δν<sub>1/2</sub> = 33 Hz).

[RuCl(κ<sup>2</sup> N-{ONC(CH<sub>2</sub>)<sub>4</sub>CNOH})(η<sup>6</sup> -p-cymene)], 2-*H* (Chart 8). Prepared from [RuCl<sub>2</sub>(η<sup>6</sup> -p-cymene)]<sub>2</sub> (70 mg, 0.114 mmol), nioxime (33 mg, 0.23 mmol) and NaHCO<sub>3</sub> (19 mg, 0.23 mmol), according to procedure D. Yellow-orange solid, yield: 86 mg, 91%. Soluble in MeOH, CH<sub>2</sub>Cl<sub>2</sub>, less soluble in acetone, MeCN, scarcely soluble in Et<sub>2</sub>O. Anal. calcd. for C<sub>16</sub>H<sub>23</sub>ClN<sub>2</sub>O<sub>2</sub>Ru: C, 46.66; H, 5.63; N, 6.80. Found: C, 45.27; H, 5.35; N, 6.49. IR (solid state):  $\tilde{\nu}/\text{cm}^{-1}$  = 3064w, 2959w, 2928w, 2864w, 1595w, 1500w-sh, 1467 m, 1449 m, 1427 m, 1385 m, 1300w, 1303 m, 1253w, 1228w, 1162s, 1101s (NO), 1029s (N-O), 999 s-sh, 898 s, 864m-sh, 798s, 747w. <sup>1</sup>H NMR (CD<sub>3</sub>-OD): δ/ppm = 5.75 (d, 3 J<sub>HH</sub> = 6.3 Hz, 2H, C4 H), 5.38 (d, 3 J<sub>HH</sub> = 6.2 Hz, 2H, C3 H), 2.72 (hept, 3 J<sub>HH</sub> = 6.9 Hz, 1H, C6 H), 2.66–2.59 (m, 4H, C9 H), 2.20 (s, 3H, C1 H), 1.61–1.53 (m, 4H, C10H), 1.15 (d, 3 J<sub>HH</sub> = 6.9 Hz, 6H, C7 H). <sup>13</sup>C{<sup>1</sup>H} NMR (CD<sub>3</sub>OD): δ/ ppm = 165.8 (C8 ); 106.5 (C5 ), 103.0 (C2 ), 89.3 (C4 ), 85.9 (C3 ), 32.5 (C6 ), 26.5 (C9 ); 22.50, 22.48 (C7 + C10); 19.2 (C1 ). UV-vis (MeOH, 2.4 × 10<sup>-3</sup> M): λ<sub>max</sub>/nm (ε/M<sup>-1</sup> cm<sup>-1</sup>) = 240 (104 ), 292 (104 ), 328sh (5.8 × 10<sup>3</sup> ), 390br (1.6 × 10<sup>3</sup> ). λ<sub>m</sub> (MeOH, 2.4 × 10<sup>-3</sup> M): 11 S cm<sup>2</sup> mol<sup>-1</sup> .

[RuI(κ<sup>2</sup> N-{ONC(CH<sub>2</sub>)<sub>4</sub>CNOH})(η<sup>6</sup> -p-cymene)], 3-*H* (Chart 9). Prepared from [RuI<sub>2</sub>(η<sup>6</sup> -p-cymene)]<sub>2</sub> (53 mg, 0.054 mmol), nioxime (16 mg, 0.11 mmol) and NaHCO<sub>3</sub> (10 mg, 0.12 mmol), according to procedure D.

Orange solid, yield: 45 mg, 80%. The insolubility of 3-H in CH<sub>2</sub>Cl<sub>2</sub> and acetone prevented its purification from traces of sodium salts, as revealed by conductivity and CHN analyses. Therefore, an alternative strategy was adopted. A suspension of [RuI<sub>2</sub>(η<sup>6</sup>-pcymene)]<sub>2</sub> (160 mg, 0.164 mmol) and nioxime (47 mg, 0.33 mmol) in MeOH (10 mL) was stirred at room temperature for 1.5 h. The resulting red-brown solution was treated with Ag<sub>2</sub>O (38 mg, 0.17 mmol) and stirred at room temperature for 2.5 h under protection from the light. The amber orange suspension was diluted with MeOH and filtered over celite. The orange filtrate was taken to dryness under vacuum and the residue was triturated in acetone/Et<sub>2</sub>O 1 : 1 v/v. The suspension was filtered and the resulting orange solid was washed with Et<sub>2</sub>O, hexane and dried under vacuum (40 °C). Yield: 129 mg, 78%. Fairly soluble in MeOH, less soluble in EtOH, DMSO, insoluble in CH<sub>2</sub>Cl<sub>2</sub>, acetone, diethyl ether, hexane. Anal. calcd. for C<sub>16</sub>H<sub>23</sub>I<sub>2</sub>N<sub>2</sub>O<sub>2</sub>Ru: C, 38.18; H, 4.61; N, 5.57. Found: C, 37.12; H, 4.56; N, 5.38. IR (solid state):  $\tilde{\nu}/\text{cm}^{-1}$  = 3080w, 3039w, 2961 m, 2940 m, 2862 m, 2800–2400m-br, 1498w, 1461m-sh, 1438s, 1423s-sh, 1388m, 1380m, 1369s, 1359s, 1298s, 1280m-sh, 1247w, 1232w, 1176s, 1159s-sh, 1109s (N=O), 1088s-sh, 1075m-sh, 1063 m, 1035s (N-O), 1019s, 1003s-sh, 988s-sh, 969s, 943m-sh, 927m-sh, 902s, 896s, 883m-sh, 858s, 795s, 756m, 744ss, 690w, 665 m. <sup>1</sup>H NMR (CD<sub>3</sub>OD):  $\delta/\text{ppm}$  = 5.67 (d, 3 J<sub>HH</sub> = 6.3 Hz, 2H, C4 H), 5.38 (d, 3 J<sub>HH</sub> = 6.2 Hz, 2H, C3 H), 2.87 (hept, 3 J<sub>HH</sub> = 6.9 Hz, 1H6 H), 2.71–2.56 (m, 4H, C9 H), 2.48, 1.63–1.51(m, 4H, C10H), 1.17 (d, 3 J<sub>HH</sub> = 6.9 Hz, 6H, C7 H). <sup>13</sup>C{<sup>1</sup>H} NMR (CD<sub>3</sub>OD):  $\delta/\text{ppm}$  = 105.6 (C5 ), 104.4 (C2 ), 88.9 (C4 ), 86.5 (C3 ), 32.9 (C6 ), 26.6 (C9 ), 22.5 (C7 + C10), 21.4 (C1 ). The resonance of C8 was not detected due to limited solubility. UV-

vis (MeOH,  $2.0 \times 10^{-3}$  M):  $\lambda_{\text{max}}/\text{nm}$  ( $\epsilon/M-1 \text{ cm}^{-1}$ ) = 290 ( $7.3 \times 10^3$ ), 418 ( $8.4 \times 10^2$ ).  $\Lambda_{\text{m}}$  (MeOH,  $2.0 \times 10^{-3}$  M):  $10 \text{ S cm}^2 \text{ mol}^{-1}$ .

*[RuCl( $\kappa^2$  N-{ONC(CH<sub>3</sub>)C(CH<sub>3</sub>)NOH})( $\eta^6$ -C<sub>6</sub>Me<sub>6</sub>)]*, 4-H (Chart 10). Prepared from [RuCl<sub>2</sub>( $\eta^6$ -C<sub>6</sub>Me<sub>6</sub>)]<sub>2</sub> (55 mg, 0.082 mmol), dimethylglyoxime (20 mg, 0.17 mmol) and NaHCO<sub>3</sub> (14 mg, 0.17 mmol), according to procedure D. Yellow solid, yield: 60 mg, 88%. Soluble in CH<sub>2</sub>Cl<sub>2</sub>, MeOH, poorly soluble in Et<sub>2</sub>O, insoluble in hexane. X-ray quality crystals of 4-H·1.5H<sub>2</sub>O were obtained from a solution of [4]NO<sub>3</sub> in EtOH, layered with Et<sub>2</sub>O and stored at -20 °C. Anal. calcd. for C<sub>16</sub>H<sub>25</sub>ClN<sub>2</sub>O<sub>2</sub>Ru: C, 46.43; H, 6.09; N, 6.77. Found: C, 44.05; H, 6.01; N, 6.65. IR (solid state):  $\tilde{\nu}/\text{cm}^{-1}$  = 3019w, 2998w, 2979w, 2914w, 1613w-sh, 1556w, 1440s, 1380s, 1363m-sh, 1213m-sh, 1186s, 1109s (N=O), 1069 m, 1041s (N-O), 1010s-sh, 993s-sh, 955s, 920m-sh, 832w-sh, 735m, 720m, 703m. <sup>1</sup>H NMR (CD<sub>3</sub>-OD):  $\delta/\text{ppm}$  = 2.12 (s, 18H, C1 H); 2.10 (s, 6H, C4 H). No changes were observed in the <sup>1</sup>H NMR spectrum after a few days at room temperature. <sup>13</sup>C{<sup>1</sup>H} NMR (CD<sub>3</sub>OD):  $\delta/\text{ppm}$  = 164.7 (C3), 98.7 (C2), 15.5 (C1), 12.8 (C4). UV-vis (MeOH,  $1.9 \times 10^{-3}$  M):  $\lambda_{\text{max}}/\text{nm}$  ( $\epsilon/M-1 \text{ cm}^{-1}$ ) = 238 ( $1 \times 10^4$ ), 294 ( $6.2 \times 10^3$ ), 328sh ( $4.1 \times 10^3$ ), 387br ( $1.4 \times 10^3$ ).  $\Lambda_{\text{m}}$  (MeOH,  $1.9 \times 10^{-3}$  M):  $11 \text{ S cm}^2 \text{ mol}^{-1}$ .

### 7.6.3 X-ray crystallography

Crystal data and collection details for [3]NO<sub>3</sub>, [4]NO<sub>3</sub>·H<sub>2</sub>O and 4-H·1.5H<sub>2</sub>O are reported in Table 5. Data were recorded on a Bruker APEX II diffractometer equipped with a PHOTON2 detector using Mo-K $\alpha$

radiation. The structures were solved by direct methods and refined by full-matrix least-squares based on all data using F2. 59 Hydrogen atoms were fixed at calculated positions and refined using a riding model, except O-bonded hydrogens that have been located in the difference Fourier map and refined isotropically.

#### 7.6.4 Reactivity studies in MeOH

General procedures are described below. With Brønsted bases. A solution of the dioxime compound (ca. 20 mg) in MeOH (2 mL) was treated with the selected base (up to 2.0 equivalents) and stirred at room temperature for 3–8 h. Addition of t BuOK was performed from a 1 M THF solution in anhydrous MeOH under N<sub>2</sub>. Volatiles were removed under vacuum and the yellow/brown residue was analyzed by <sup>1</sup>H NMR (CD<sub>3</sub>OD). The NMR tube was kept at room temperature overnight (14–18 h) and a new <sup>1</sup>H NMR spectrum was recorded. 2) With silver nitrate. A solution of dioxime compound (ca. 15 mg) in MeOH (2 mL) was treated with AgNO<sub>3</sub> (1.0 equivalent) and stirred at room temperature for 1 h under protection from the light. A light grey/yellow solid (silver halide) was separated by filtration over celite. The filtrate solution was taken to dryness under vacuum and the brown residue was analyzed by <sup>1</sup>H NMR (CD<sub>3</sub>OD). The NMR tube was kept at room temperature overnight (ca. 14 h) and the <sup>1</sup>H NMR spectrum was recorded. 3) Under catalytically relevant conditions. In a 10-mL test tube under N<sub>2</sub>, a solution of [3]NO<sub>3</sub> or [5]NO<sub>3</sub> (ca. 15 mg) in anhydrous MeOH (2 mL) was treated with PhNO<sub>2</sub> and t - BuOK (20 eq. each). The dark brown solution was stirred at room

temperature for 1 h then at reflux for 20 h and finally analyzed by  $^1\text{H}$  NMR and  $^1\text{H}$ - $^{13}\text{C}$  HMBC ( $\text{CD}_3\text{OD}$ ). An analogous experiment was carried out using  $\text{PhNH}_2$  instead of  $\text{PhNO}_2$ . In both cases, the selective formation of [3-2H] – or [5-2H] – was observed at room temperature. Progressive release of the  $\eta^6$ -arene ligand was observed over time (p-cymene: ca. 50% after 6 h and almost quantitative after 20 h;  $\text{C}_6\text{Me}_6$ : 80% after 20h).

### 7.6.5 Catalytic activity

The catalytic N-methylation reactions were carried out under a  $\text{N}_2$  atmosphere in a pressure tube equipped with a Teflon high vacuum stopcock. Inside a glove box, an oven dried reactor was charged with the nitrocompound (0.5 mmol), the base (t BuOK 0.5 mmol), and the catalyst (0.02 mmol, 4 mol%), dissolved in dry methanol (1 mL). After sealing, the reactor was purged three times with nitrogen and then pressurized with 1 atm of nitrogen. The resulting mixture was stirred at room temperature until complete dissolution of the catalyst and then placed in a thermostated oil bath at  $130\text{ }^\circ\text{C}$ . After 18 h, it was left to cool to RT and the conversion and selectivity were determined by gas chromatography (GCFID). The N-methylanilines were isolated by the following procedure. After the completion of the reaction, the reaction mixture was cooled to room temperature and filtrated through a pad of celite. After evaporating the solvent through rotary evaporator, the residue was eluted through a silica gel column using hexane/diethyl ether (typically 9 : 1 v/v) as eluent. The fraction containing the product was treated with 4 M HCl in dioxane. After the removal of volatiles under vacuum, the pure N-

methylaniline hydrochloride salt was dissolved in 0.5 mL of D<sub>2</sub>O or CDCl<sub>3</sub> and analyzed by <sup>1</sup>H and <sup>13</sup>C NMR.

## 7.7 Conclusions

Beginning with commercially available dioxime ligands, we successfully synthesized seven novel piano-stool ruthenium(II) complexes featuring distinct  $\eta^6$ -arene and halide ligands. These complexes were isolated as nitrate or hexafluorophosphate salts with high yields ranging from 77% to 97%. Through mono-deprotonation of the coordinated dioxime, we prepared three zwitterionic oxime–oximato complexes. The elucidation of crystal structures for both cationic and neutral complexes represents a rare instance of X-ray studies on ruthenium dioxime complexes. In optimized conditions (MeOH, <sup>t</sup>BuOK, 130 °C, 18 h), the dioxime complexes exhibited excellent conversion (91–99%) and selectivity (80–96%) in the one-pot transfer hydrogenation and *N*-methylation of nitrobenzene at a low catalyst loading (4 mol%). Comparative analysis of the catalytic performance with other ruthenium(II) arene complexes, including the well-known Noyori–Ikariya catalyst, underscored the pivotal role played by the dioxime ligand in the hydrogen borrowing step (*N*-methylation of aniline). The most effective compound, [RuI(nioxime)(*p*-cymene)]NO<sub>3</sub>, denoted as [3]NO<sub>3</sub>, also demonstrated efficacy in the tandem reduction/*N*-monomethylation of various aromatic nitrocompounds. Time-profile analysis and deuterium labeling experiments of the model system enabled the detection of aniline as the



sole reaction intermediate, reaffirming the role of methanol as both an H<sub>2</sub> donor and alkylating agent. Additional experiments with [3]NO<sub>3</sub> indicated the homogeneous nature of the catalytic system and the plausible activation step of the pre-catalyst through the thermal dissociation of the *p*-cymene ligand. Overall, the ruthenium(II) arene dioxime complexes described herein prove to be effective catalysts for the tandem reduction/*N*-methylation of nitroarenes, suggesting the potential application of this readily available and customizable class of compounds for other hydrogen borrowing processes. Furthermore, our findings propose to the broader inorganic chemistry community the consideration of dioximes as ligands for catalyst development, an aspect that has been overlooked until now.

## References

1. Lawrence S. A., **2004**, *Cambridge University Press*, Cambridge, U.K.
2. Chen Y., **2019**, *Chem. – Eur. J.*, 25, 3405–3439.
3. Wang X., Zhao K., Wang H., Shi F., **2021**, *Catal. Sci. Technol.*, 11, 7239–7254.
4. Latham D. E., Dambatta M. B., Morrill L. C., **2021**, *ACS Cent. Sci.*, 7, 570–585.
5. Del Zotto A., Baratta W., Sandri M., Verardo G., Rigo P., **2004**, *Eur. J. Inorg. Chem.*, 524–529.
6. Broomfield L. M., Wu Y., Martin E., Shafir A., **2015**, *Adv. Synth. Catal.*, 357, 3538–3548.
7. Meng C., Liu P., Thanh Tung N., Han X., Li F., **2020**, *J. Org. Chem.*, 85, 5815–5824.
8. Wang D., Astruc D., **2015**, *Chem. Rev.*, 115, 6621–6686.
9. Paul B., Shee S., Chakrabarti K., Kundu S., **2017**, *ChemSusChem*, 10, 2370–2374.
10. Podyacheva E., Afanasyev O. I., Vasilyev D. V., Chusov D., **2022**, *ACS Catal.*, 12, 7142–7198.
11. Dolui D., Khandelwal S., Majumder P., Dutta A., **2020**, *Chem. Commun.*, 56, 8166.
12. Taqui Khan M. M., Ramachandraiah G., Mehta S. H., **1989**, *J. Mol. Catal.*, 50, 123–129.

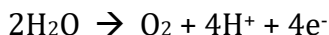
13. Kumar Awasthi M., Tyagi D., Patra S., Kumar Rai R., Mobin S. M., Kumar Singh S., **2018**, *Chem. – Asian J.*, 13, 1424–1431.
14. Mizerska T. G. U., Moszner M., O'Brien M., Perry R., Stanczyk W. A., **2004**, *Appl. Catal., A*, 259, 49–55.
15. Jensen S. B., Rodger S. J., Spicer M. D., **1998**, *J. Organomet. Chem.*, 556, 151–158.
16. Biancalana L., Zanda E., Hadiji M., Zacchini S., Pratesi A., Pampaloni G., Dyson P. J., Marchetti F., **2021**, *Dalton Trans.*, 50, 15760–15777.
17. Zanda E., Busto N., Biancalana L., Zacchini S., Biver T., Garcia B., Marchetti F., **2021**, *Chem.-Biol. Interact.*, 344, 109522.
18. Biancalana L., Pampaloni G., Zacchini S., Marchetti F., **2018**, *J. Organomet. Chem.*, 869, 201–211.
19. Bennett M. A., Huang T. N., Matheson T. W., Smith A. K., **1982**, *Inorg. Synth.*, 21, 72–78.
20. Huber W., Bröhler P., Wätjen W., Frank W., Spingler B., Kunz P. C., **2012**, *J. Organomet. Chem.*, 717, 187–194.

## 8. Synthesis of new Iron complexes for water oxidation catalysis

This work was carried out during a research period abroad at the ICIQ in Tarragona (Spain), in Professor Antoni Llobet's research group, under his direct supervision.

### 8.1 Introduction

Currently, the world's energy supply is largely based on fossil fuels, which manifests itself in serious global problems, such as the greenhouse effect, pollution and energy crises. The development of sustainable energy systems is urgently needed. The efficient use of sunlight to generate solar fuels attracts much attention today [1]. Hydrogen is among the most prospective chemical energy carriers that can be generated in a pure form from the splitting of water. The oxygen evolution reaction (Equation 3), is arguably the most challenging process of overall water splitting.



Equation 3. Oxygen evolution reaction (OER)

The removal of four protons and four electrons from two water molecules, which undergo the formation of O-O bonds to produce O<sub>2</sub> as a final step, is a challenging process from both a kinetic and thermodynamic point of view [2]. It has been shown for several Ru or Ir-

based water oxidation catalysts (WOCs) that efficiency can be combined with robustness by molecular design [3]. On the other hand, it is clear that low-cost, robust and effective WOCs should rather rely on abundant elements. Fascinating new results on molecular catalysts based on first-row transition metal indicate that research can be fruitful to advance the field in this direction [4]. However, while the high abundance and low cost of these metals are attractive properties, the insufficient stability of their complexes remains a serious challenge. A prominent representative of these metals is iron which is involved in numerous biochemical and artificial catalytic oxidation processes in which the active species  $\text{Fe}^{\text{IV/V}}=\text{O}$  have been shown to be responsible for reactivity [5]. This fact is encouraging with respect to the potential application of Fe in single-site molecular WOCs, since the high oxidation state  $\text{M}=\text{O}$  intermediate required for nucleophilic water attack (WNA) should be available from  $\text{Fe}^{\text{II}}-\text{OH}_2$  or  $\text{Fe}^{\text{III}}-\text{OH}/\text{OH}_2$  complexes. Some shared features of the most active systems allow for the naming of additional WOC candidates, namely easy access to high oxidation states, robust auxiliary ligands, and cis coordination of two water molecules. Furthermore, complex decomposition in working conditions can lead to another species or up to iron oxides [6]. In order to develop advanced systems involving Fe-based WOCs in electrocatalysis that can take advantage of these molecular units, the synthesis of 2D macrocyclic structures based on mono- and bi-nuclear complexes of iron is a promising strategy for the stabilization of these new catalysts.

The real increase in activity and efficiency of the complexes used in WOC occurred with the development of the Ru complexes based on the  $\text{H}_2\text{bda}$  ligand ([2,2'-bipyridine]-6,6-dicarboxylic acid) providing compounds of

[Ru<sup>II</sup>(bda)]. Another recent Ru(bda) inspired WOC that operates via a monomolecular mechanism for the O-O bond form was developed by Llobet *et al* [7] and is currently the ruthenium complex with best TOF synthesized for WOC (Figure 38). The purpose of this work is to design new catalysts for WOC shifting the focus to another transition metal, iron. Iron is much more abundant than ruthenium, less expensive and also has greater environmental compatibility. The disadvantages of using iron for catalysis are the lack of stability of its organometallic complexes and the redox stability. The control over the electronic and geometric structure of the complexes through the design of ligands would determine their general characteristics and in particular the catalytic performance against water oxidation. It is for this reason that binuclear iron catalysts have been synthesized, in order to arrive at the synthesis of 2D macrocyclic structures capable of significantly increasing the stability and activity of these iron catalysts.

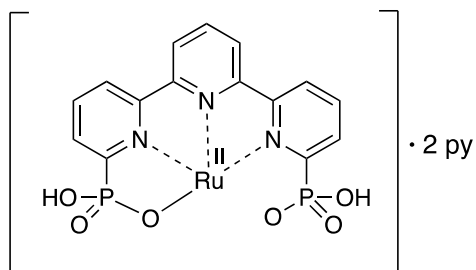


Figure 38. [Ru<sup>II</sup>(HztPa-κ-N<sup>3</sup>O)(py)<sub>2</sub>]: ruthenium complex synthesized by Llobet and coworkers

## 8.2 Synthesis of the ligand

The aim of this work is to synthesize a binuclear iron complex, using a cluttered ligand with a strong N-donor power, capable of stabilizing the metal. For this reason, it was decided to synthesize the ligand in Figure 39.

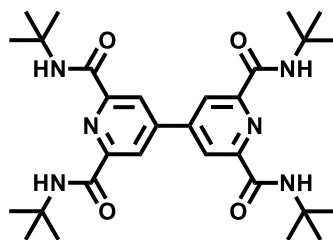


Figure 39. Proposed ligand for the binuclear complex

In the first synthetic route conceived (Figure 40), the synthesis of the ligand included five synthetic steps:

1. Miyaura borylation;
2. Suzuki coupling;
3. oxidation;
4. formation of acyl chloride;
5. amide formation.

During the work, as explained in detail below, the steps have been optimized to four.

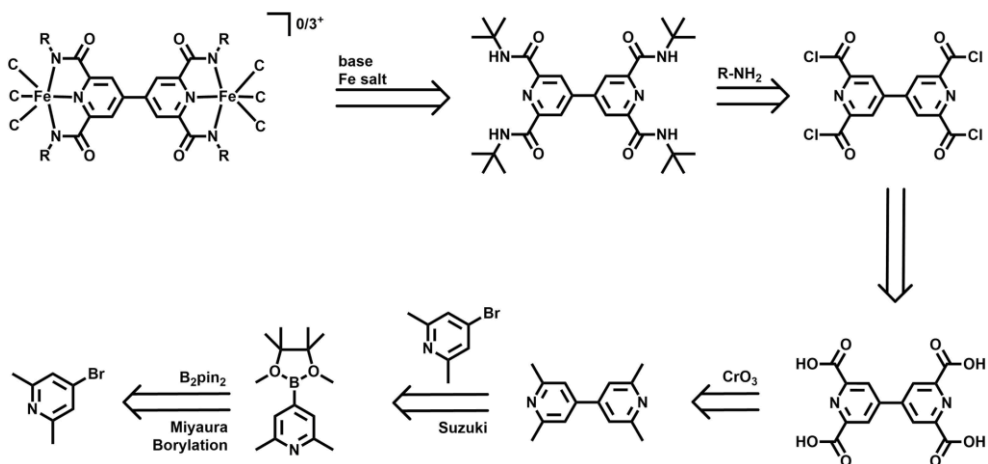


Figure 40. First retrosynthetic route conceived

### 8.3 One-pot Miyaura-Suzuki coupling

The first step of the synthesis was the Miyaura borylation, followed by a Suzuki coupling (Figure 41). We tried to optimize the borylation but the yield was not very high (54.17%) and furthermore the product was not very stable making a scale up very difficult. For this reason, it was decided to proceed with a one-pot Miyaura-Suzuki reaction. The reaction was optimized, without having to increase the amount of palladium catalyst, leading to higher yields (68.03%). A scale up was also possible and a step in the synthetic way was eliminated, thus optimizing time and costs. It was also possible, with this procedure, to avoid isolating the intermediate, corresponding to the borylation product, eliminating the problem of stability and not very easy purification. Below the characterization of the pure product.



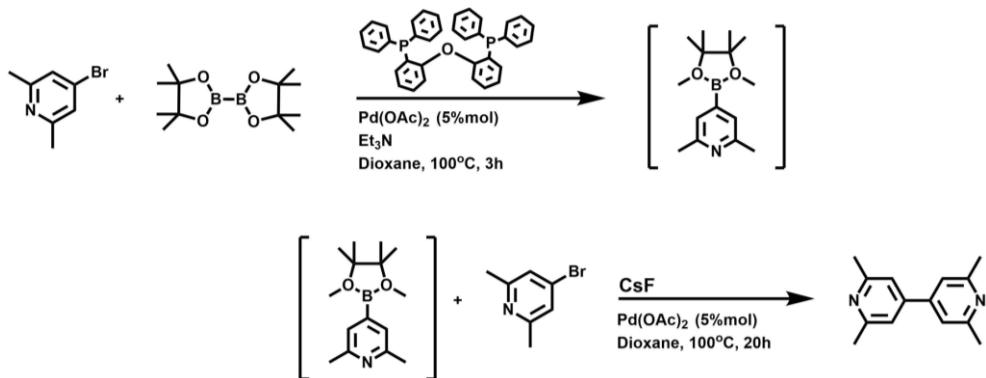


Figure 41. *One-pot Miyaura-Suzuki coupling conditions*

#### 8.4 Synthesis of tetracarboxylic acid

To obtain the tetra carboxylic acid (Figure 42), it was decided to use  $\text{CrO}_3$  as oxidizing agent, which is reported in literature as the most used for this type of reaction. In reality, the reaction showed a good yield the first time it was carried out (87.89%) but it proved to be non-reproducible, probably due to the poor solubility of the reagent, which became more evident with the scale up. It was therefore decided to take another route, using  $\text{K}_2\text{Cr}_2\text{O}_7$  as oxidizing agent. With this different reagent the yield remained high (89.36%) and the procedure proved to be perfectly reproducible. Below the characterization of the pure product.

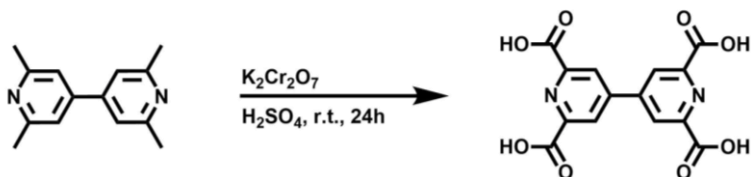


Figure 42. *Synthesis of tetracarboxylic acid conditions*

## 8.5 Synthesis of tetra acyl chloride

Once the acid was obtained, the corresponding acyl chloride (Figure 43) was synthesized, basically using  $\text{SOCl}_2$  as a source of chlorides to replace the hydroxyl groups of the acid. Since these products are particularly sensitive to moisture, the characterization was done via ATR-IR. In the spectrum it is possible to see the disappearance of the -OH band around  $3152\text{ cm}^{-1}$  and a slight shift of the carbonyl peak from  $1738\text{ cm}^{-1}$  to  $1730\text{ cm}^{-1}$ , confirming the formation of acyl chloride.

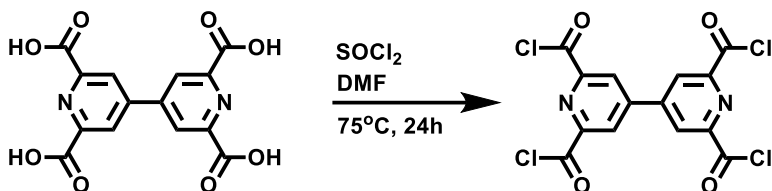


Figure 43. Synthesis of tetra acyl chloride conditions

## 8.6 Synthesis of amide ligand

In order to try to further optimize the synthetic route, a one-pot reaction was initially tested that led directly from the acid to the amide. Unfortunately, the reaction gave a mixture of products that were very difficult to separate from each other, so it was decided to synthesize the amide starting from acyl chloride and the amine (Figure 44). The reaction immediately led to the desired product but with a not very good yield (26.27%). The reaction conditions were then further optimized to obtain a pure product with a yield of 59.84%. Below the characterization of the pure product.

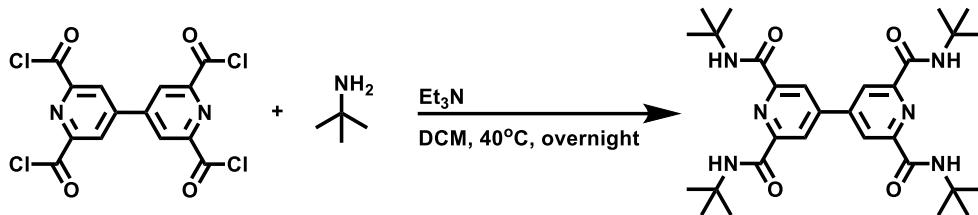


Figure 44. *Synthesis of amide ligand conditions*

### 8.7 Synthesis of the catalysts

In order to obtain the complex, the first iron salt that was used was the  $\text{Fe}(\text{OTf})_3$  (Figure 45).

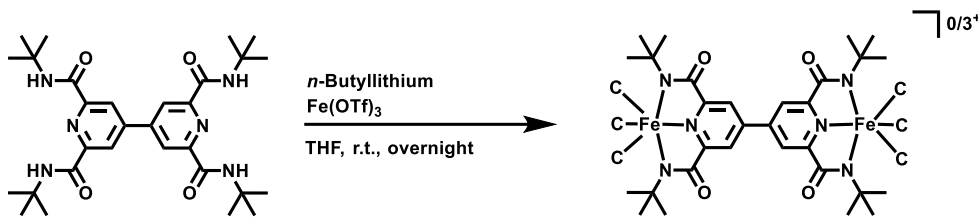


Figure 45. *Synthesis of catalyst conditions*

At the end of the reaction the product appeared as a brown solid. However, it was not possible to characterize it as it was not soluble in any solvent. The only solvent in which partial solubility was observed was water, but a few seconds after solubilization a precipitate was formed, suggesting that the complex was soluble but not stable in water. To increase the solubility of the complex, a ligand exchange reaction with pyridine was performed. The product obtained, again a brown solid, proved to be partially soluble in acetonitrile and propylene carbonate, but to analyze it through cyclic voltammetry (CV) it was necessary to use

the drop casting technique and carry out the tests in DCM. The CV is unclear and difficult to analyze as shown in the Figure 46.

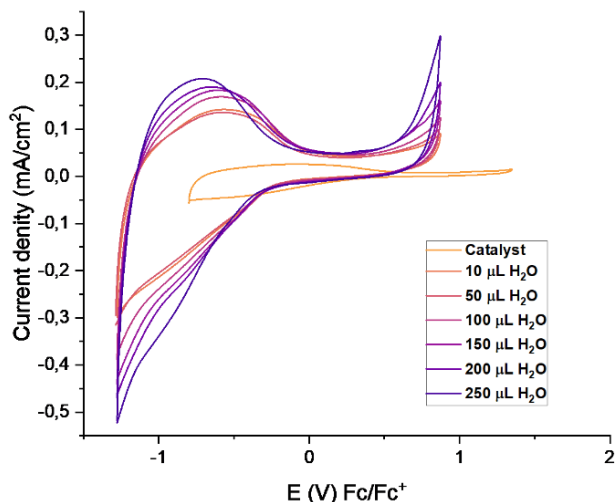


Figure 46. CV conditions: WE: Fe<sub>2</sub>Py@GCd, GCd (0.71 cm<sup>2</sup>) RE: Ag<sub>wire</sub>/Fc/Fc<sup>+</sup>, CE: Pt,  $\nu = 100$  mV/s, 0.1 M TBAPF<sub>6</sub> in DCM, addition of phosphate buffer (pH=11); drop casting procedure: [Fe] = 0.5 mM in MeCN 3 X 20  $\mu$ L

It is evident that there is some type of process and probably an active species that shows activity as the amount of water increases, but it is difficult to define exactly the process that is taking place. For this reason, it was decided to change the iron precursor and switch to FeCl<sub>3</sub>. Also in this case the first experiment was done without the addition of pyridine. A more orange solid was obtained than the synthesis with the other iron precursor, but also this time insoluble. Then the same ligand exchange reaction was done with pyridine. This time the product was a sticky

brown solid perfectly soluble in acetonitrile and it has been possible to characterize it.

### *8.8 Characterization of the complex*

In order to characterize the complex and to understand the possible catalytic activity, CV experiments were performed, as explained in detail below. First of all was performed a CV to determine the possible activity and the stability of the complex (Figure 47). From the voltammogram it is possible to see a first wave corresponding to a reversible oxidation process, which involves a single electron. There are also two other treatments, one with higher currents which could correspond to the active species and another barely visible which could be a semi-irreversible process. It is also possible to state that after ten cycles the catalyst is sufficiently stable. Given the promising results of the first experiment, we moved on to preliminary catalytic tests.

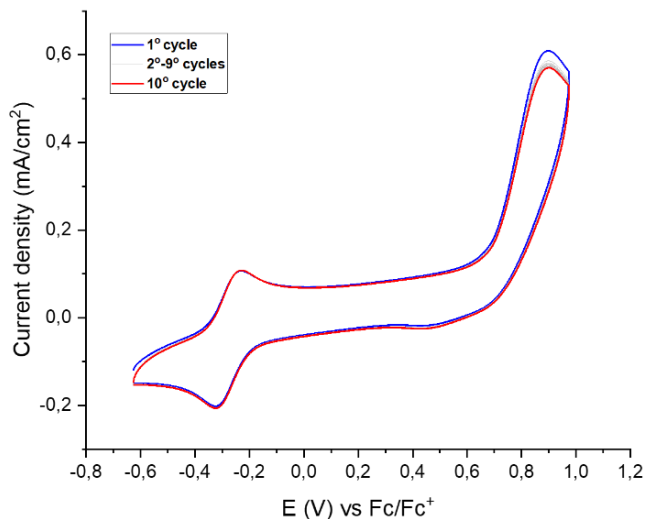


Figure 47. CV conditions: WE: GCd (0.71 cm<sup>2</sup>) RE: Ag<sub>wire</sub>/Fc/Fc<sup>+</sup>, CE: Pt,  $\nu = 100$  mV/s, 0.1 M TBAPF<sub>6</sub> in MeCN, [Fe] = 1 mM (estimated concentration)

### 8.9 Preliminary catalytic tests

To understand if there was actually activity, some water was added (phosphate buffer pH = 11). What has been observed is the increase in the current density of the curve which should represent the active intermediate, in proportion to the increase in the amount of water added. This could indicate that it is actually the super oxidized active species (Fe<sup>IV</sup> /  $\nu = 0$ ) and that therefore the complex is catalytically active. Furthermore, two other phenomena were observed: the progressive decrease of the current density of the first curve and the growth of the curve which should represent the semi-reversible process. Both suggest that there is a change in the structure of the catalyst that could be

attributed to an exchange in the inner sphere of coordination in which the H<sub>2</sub>O molecules replace the chlorides (Figure 48).

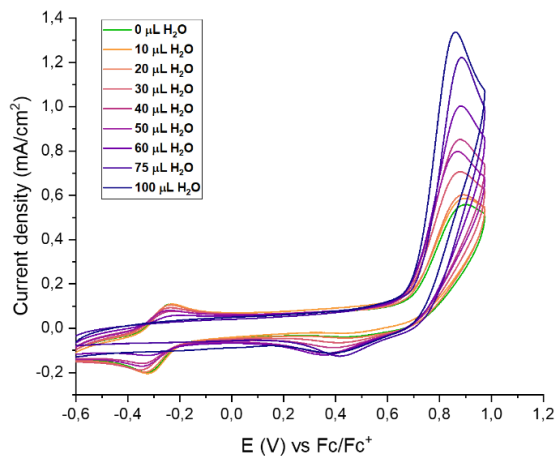


Figure 48. CV conditions: WE: GCd (0.71 cm<sup>2</sup>) RE: Ag<sub>wire</sub>/Fc/Fc<sup>+</sup>, CE: Pt,  $v = 100$  mV/s, 0.1 M TBAPF<sub>6</sub> in MeCN, [Fe] = 1 mM (estimated concentration), addition of phosphate buffer (pH=11)

To further evaluate the stability of the catalyst, five cycles were repeated for the experiment with the maximum addition of H<sub>2</sub>O (100 μL). As can be seen in Figure 49 also in this case, despite the high amount of H<sub>2</sub>O, the catalyst has proved to be quite stable.

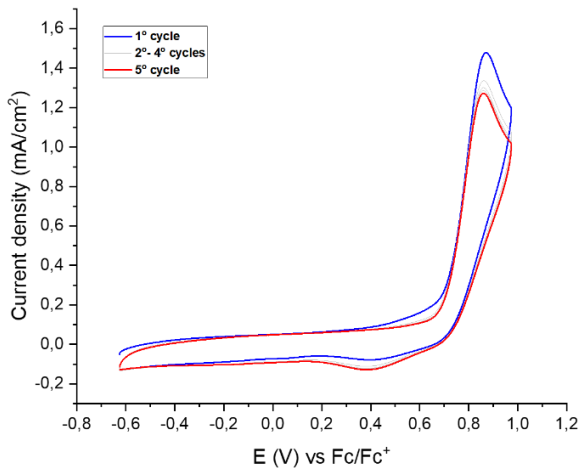


Figure 49. CV conditions: WE: GCd (0.71 cm<sup>2</sup>) RE: Ag<sub>wire</sub>/Fc/Fc<sup>+</sup>, CE: Pt,  $\nu = 100$  mV/s, 0.1 M TBAPF<sub>6</sub> in MeCN, [Fe] = 1 mM (estimated concentration), addition of phosphate buffer (pH=11)

To be sure that the observed activity was not due to FeO<sub>x</sub> nanoparticles, a Rinse test was performed. The test consists in polishing the working electrode with the solvent used, in this case acetonitrile, and repeating the experiment in a fresh electrolyte solution in which 100  $\mu$ L of H<sub>2</sub>O has been added, in order to reproduce the experimental conditions. As is evident in Figure 50 the CV made with the polish electrode is flat compared to the previous one. It is therefore possible to state that the activity is due to the catalyst and not to the FeO<sub>x</sub> nanoparticles.



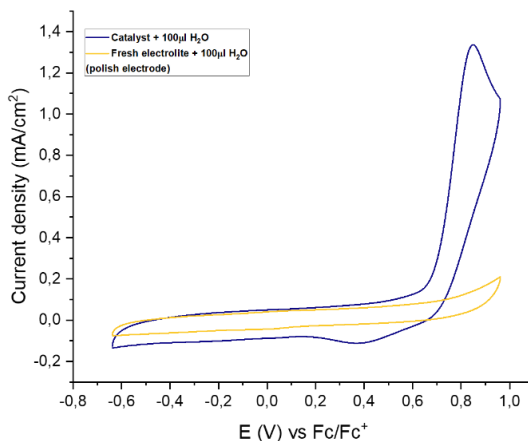


Figure 50. CV conditions: WE: GCd (0.71 cm<sup>2</sup>) RE: Ag<sub>wire</sub>/Fc/Fc<sup>+</sup>, CE: Pt,  $v = 100$  mV/s, 0.1 M TBAPF<sub>6</sub> in MeCN, [Fe] = 1 mM (estimated concentration), addition of phosphate buffer (pH=11)

## 8.10 Experimental

### 8.10.1 Synthesis of the ligand: synthetic route

At the beginning of this project it was decided to synthesize two different ligands, both with a bipyridine base, but one with imine substituents and one with amide substituents. During the optimization it was decided to focus the attention only on the ligand with amide substituents, as will be explained in detail below.

### 8.10.2 One-pot Miyaura-Suzuki coupling

For the first step, in a semi-oven dried apparatus were added 5.4 mmol of 4-bromo-2,6-dimethylpyridine, 0.54 mmol of DPEphos and 0.26

mmol of Pd(OAc)<sub>2</sub>, in 5.5 mL of 1,4-Dioxane, under Ar atmosphere. Then were added to the mixture a solution of 16.4 mmol of Et<sub>3</sub>N in 5.5 mL of 1,4-Dioxane and 1 M solution of Bis(pinacolato)diboron in THF (10.8 mmol in 11 mL of THF). The reaction mixture was heated at 100°C for 3h, under Ar. Then the reaction was cooled at R.T. For the second step 43.2 mmol of CsF in 30 mL of 1,4-Dioxane were added at the reaction mixture. After 45 minutes 5.4 mmol of 4-bromo-2,6-dimethylpyridine and 0.26 mmol of Pd(OAc)<sub>2</sub> in 20 mL of 1,4-Dioxane were added and the reaction was heated at 100°C for 20h, under Ar. The reaction was cooled at R.T. and the mixture was filtered on a celite pad. Brine was added and the aqueous phase was extracted with DCM and, after drying on MgSO<sub>4</sub>, the solvent was removed under reduced pressure. The product was purified by column chromatography (DCM/EtOAc 1:4) obtaining a pure solid (7.35 mmol, yield=68.03%).

### *8.10.3 Synthesis of tetracarboxylic acid*

1.88 mmol of 2,2',6,6'-tetramethyl-4,4'-bipyridine were added in 22 mL of H<sub>2</sub>SO<sub>4</sub> and they were mixed under stirring. Then 22.56 mmol of K<sub>2</sub>Cr<sub>2</sub>O<sub>7</sub> were added slowly at 0°C. The reaction was stirred at R.T. for 24h and then was quenched with cold water in an ice bath. The precipitate was formed and purified with sever washes with water in centrifuge (first one 10 min 4400 RPM, other ones 5 min 4400 RPM). The product was obtained as a white solid (1.68 mmol, yield=89.36%).

### *8.10.4 Synthesis of tetra acyl chloride*

In a semi-oven dried apparatus were added 1.5 mmol of tetracarboxylic acid and 10 mL of  $\text{SOCl}_2$ , under Ar. Then were added 10 drops of DMF and the reaction mixture was refluxed at  $75^\circ\text{C}$ , under Ar, for 24h. The solution was cooled at R.T. and the excess of  $\text{SOCl}_2$  was removed with vacuum distillation. The product was obtained as a light pink solid (1.5 mmol, yield 100%).

#### *8.10.5 Synthesis of amide ligand*

In a semi-oven dried apparatus were added 1.5 mmol of tetra acyl chloride in 2 mL of DCM was added dropwise in a solution containing 7.5 mmol of *tert*-Butylamine and 7.5 mmol of  $\text{Et}_3\text{N}$  in 8 mL of DCM. The reaction mixture was refluxed at  $40^\circ\text{C}$ , under Ar, for 48h. The reaction was cooled at R.T. and the product was washed with water and brine. The organic phase was dried under  $\text{MgSO}_4$ , then the solvent was removed and the product was recrystallized twice: the first time in Toluene to remove the impurities and the second time in Hexane. The product was obtained as a powder (0.89 mmol, yield=59.84%).

#### *8.10.6 Synthesis of the catalysts*

For the synthesis of the complexes it was decided to use two different salts of Fe(III) as precursors: the  $\text{Fe}(\text{OTf})_3$  and the  $\text{FeCl}_3$ .

**Synthesis of the complex with  $\text{Fe}(\text{OTf})_3$ .** In a semi-oven dried apparatus were added 0.09 mmol of ligand in 8 mL of dry THF under Ar

atmosphere and cooled to 0 °C. 0.38 mmol of *n*-BuLi were added slowly and the reaction mixture was stirred for 30 min (the color immediately changes from colorless to dark blue/purple). 0.18 mmol of Fe(OTf)<sub>3</sub> were added to the reaction mixture, the solution was warmed up to R.T. and stirred (the color change from to dark blue to brown after few minutes). 1.8 mmol of Pyridine were added and the reaction mixture was stirred overnight (the solution became reddish). The reaction was stopped, the solvent was removed and the product was reprecipitate in Toluene. The product was obtained as a pale brown powder (33 mg).

**Synthesis of the complex with FeCl<sub>3</sub>.** In a semi-oven dried apparatus were added 0.09 mmol of ligand in 8 mL of dry THF under Ar atmosphere and cooled to 0 °C. 0.38 mmol of *n*-BuLi were added slowly and the reaction mixture was stirred for 30 min (the color immediately change from colorless to dark blue/purple). 0.18 mmol of FeCl<sub>3</sub> were added to the reaction mixture, the solution was warmed up to R.T. and stirred (the color immediately changes from to dark blue to orange). 1.8 mmol of Pyridine were added and the reaction mixture and after 15 minutes a precipitate was formed. The reaction was stopped after 2h and the precipitate was removed with the centrifuge. The solvent was concentrated and the product was reprecipitate in Toluene. The product was obtained as a pale brown/orange sticky solid (79.6 mg).

#### 8.10.7 Electrochemical studies

All the electrochemical studies were performed using a glassy carbon electrode (GC) with a surface area of 0.071 cm<sup>2</sup> as working electrode, a

platinum disk as counter electrode and a silver wire electrode as reference electrode. The chosen electrolyte was the tetrabutylammonium hexafluorophosphate (TBAPF<sub>6</sub>) 0.1 M. The estimated concentration of the iron was 1 mM. In order to perform some preliminary catalytic test, different amount of phosphate buffer at pH 11 were added.

### *8.11 Conclusions and future work*

In conclusion, during my semester abroad stage at ICIQ, we have optimized a synthetic route for the synthesis of a new ligand. The ligand looks promising for the formation of binuclear iron complexes, in order to increase the stability of this metal in WOC. The complex synthesized using the FeCl<sub>3</sub>, based on preliminary studies, looks promising both in terms of stability and possible catalytic activity. The solubility problems encountered at the beginning have also been largely solved. Obviously a more in-depth characterization is needed to better understand the structure of the catalyst. Other catalytic tests will also be needed, first of all a bulk electrolysis to determine the TOF and the use of a Clark probe in order to confirm that the product of the catalysis is oxygen and its concentration. The aim of this work was from the first moment to increase the stability of the iron complexes in order to be able to apply them more easily to the WOC. For this reason, the future work will be concentrated on the synthesis of 2D macrostructures in which the building block will be the iron binuclear complex. At this point we will move on to triangular structures through the reaction with bridging ligands. Once the triangular structure has been obtained, the project will

end with the formation of 2D structures which should lead to a stable and robust iron catalyst for the WOC. It is easy to understand how important this type of research is by looking at the literature. In fact, there are very few references to these 2D structures used for the WOC, and only using ruthenium. It is for this reason that the results obtained give good hope that this innovative type of catalysts will be achieved in a fairly short time, introducing not a little novelty in the world of WOC with iron.

## References

1. Balzani V., Credi A., Venturi M., **2008**, *ChemSusChem*, , 1, 26-58.
2. Blakemore J. D., Crabtree R. H., Brudvig G. W., **2015**, *Chem. Rev.*, 23, 12974–13005.
3. Wu L., Eberhart M., Nayak A., Brennaman M. K., Shan B., Meyer T. J., **2018**, *J. Am. Chem. Soc.*, 44, 15062–15069.
4. Gil-Sepulcre M., Llobet A., **2022**, *Nat. Catal.*, 5, 79-82.
5. De Oliveira F. T., Chanda A., Banerjee D., Shan X., Mondal S., Que JR L., Bominaare E. L., Münck C., Collins T. J., **2007**, *Science*, 315, 835-838.
6. Berardi S., Drouet S., Francàs L., Gimbert-Suriñach C., Guttentag M., Richmond C., Stolla T., Llobet A., **2014**, *Chem. Soc. Rev.*, 43, 7501-7519
7. Vereshchuk N., Matheu R., Benet-Buchholz J., Pipelier M., Lebreton J., Dubreuil D., Tessier A., Gimbert-Suriñach C., Ertem M. Z., Llobet A., **2020**, *J. Am. Chem. Soc.*, 142, 5068–5077

## 9. General conclusions

As highlighted in the preceding chapters, the research conducted in this doctoral thesis encompassed various projects. The overarching goal was to thoroughly investigate metal oxide nanoparticles, optimizing their synthesis, coating, and both catalytic and biomedical applications. Throughout the study period, the characterization of the systems under examination was fundamental, conducted comprehensively through the combination of numerous diverse and complementary techniques. Specifically, the focus was on mixed iron oxide magnetic nanoparticles.

Regarding the synthesis of magnetic nanoparticles, three main methods were studied and optimized: solvothermal synthesis, hydrothermal synthesis, and synthesis of nanoparticles in DES (Deep Eutectic Solvents). Through the study and optimization of solvothermal and hydrothermal methods, we were able to synthesize cores of magnetite, maghemite, Ni-ferrite, Co-ferrite, and NiCo-ferrite. By investigating these synthesis methodologies and characterizing the obtained nanoparticles, we achieved reproducible syntheses, and importantly, we were able to modify the magnetic properties and morphology of the nanoparticles during the synthesis phase. In particular, superparamagnetic ferrite nanoparticles were obtained, along with nanoparticles exhibiting different hysteresis loops, depending on the presence of Ni, Co, or both. Additionally, the nanoparticles also exhibit diverse sizes and morphologies. Regarding synthesis in DES, we aimed to correlate the properties of five different DES with the properties of the obtained nanoparticles.



Specifically, it was envisaged to employ the optimized conditions for hydrothermal synthesis in DES.

Through this work, we succeeded in demonstrating that indeed the nature of the DES influenced both the magnetic properties and the morphology of the nanoparticles.

All the magnetic nanoparticles obtained were used as cores for subsequent applications.

After synthesis, the focus shifted to optimizing the coating. Silica was chosen as coating due to its inertness in the reaction environment and ease of functionalization for subsequent applications. Based on the subsequent functionalization, both amorphous silica and mesoporous silica (MCM-41) were synthesized. In both cases, we were able to achieve homogeneous coatings that completely covered the core without exposing the iron and did not excessively obscure the magnetization of the respective cores.

Regarding amorphous silica, the cores coated with it were used for the heterogenization of molybdenum and vanadium organometallic complexes. With this work, we demonstrated that the catalysts were active and selective in the selective oxidation reaction of double bonds, both in organic solvent and in water. Furthermore, we showed that, for molybdenum complexes, the catalysts are recyclable and reusable up to five times without significantly losing activity.

Initially, amorphous silica was also used to coat the cores containing mixed oxides of Ni and Co.

In this case, the catalytically active component was not an organometallic complex but rather nanoparticles of Pd and Ru. For this reason, it was essential to have a coating with the maximum possible surface area. Mesoporous silica was therefore chosen, which provided better results both in terms of surface area and metal loading. These catalysts were then tested in the Suzuki coupling reaction via magnetic induction. The preliminary results obtained in this work demonstrated that catalysis via magnetic induction leads to faster kinetics and higher conversion at the same time and temperature compared to conventional catalysis.

Finally, we decided to utilize the magnetic nanoparticles synthesized via the hydrothermal method for a biomedical application. In this work, the magnetic nanoparticles formed the basis of Metal Phenolic Networks (MPNs) containing cross-linked tannic acid in two different modes and  $Gd^{3+}$  ions. This resulted in the synthesis of a contrast agent for imaging, which proves to be a promising starting point for dual-mode contrast agents, currently of particular interest in the scientific community for their versatility.

In the last part of my thesis, having in mind the perspective of future heterogenization, two homogeneous catalysis projects were conducted. The first involved optimizing the one-pot reduction/N-methylation reaction of nitroarenes. Methanol was chosen as the methylating agent, also serving as the solvent. The catalysts were Ru half-sandwich complexes containing oxime ligands. It was demonstrated that the oxime ligand had a significant effect on the selectivity of the desired alkylation product.

The second project was carried out during a period abroad at the ICIQ in Tarragona in Professor Antoni Llobet's research group. A new catalyst for water oxidation catalysis was synthesized. The synthesized complex was a dinuclear iron complex with a non-innocent redox-active pyridine-based ligand. Preliminary studies showed that the complex is active in the water oxidation reaction and remains stable even after the addition of significant amounts of water.